



저작자표시-비영리-변경금지 2.0 대한민국

이용자는 아래의 조건을 따르는 경우에 한하여 자유롭게

- 이 저작물을 복제, 배포, 전송, 전시, 공연 및 방송할 수 있습니다.

다음과 같은 조건을 따라야 합니다:



저작자표시. 귀하는 원저작자를 표시하여야 합니다.



비영리. 귀하는 이 저작물을 영리 목적으로 이용할 수 없습니다.



변경금지. 귀하는 이 저작물을 개작, 변형 또는 가공할 수 없습니다.

- 귀하는, 이 저작물의 재이용이나 배포의 경우, 이 저작물에 적용된 이용허락조건을 명확하게 나타내어야 합니다.
- 저작권자로부터 별도의 허가를 받으면 이러한 조건들은 적용되지 않습니다.

저작권법에 따른 이용자의 권리는 위의 내용에 의하여 영향을 받지 않습니다.

이것은 [이용허락규약\(Legal Code\)](#)을 이해하기 쉽게 요약한 것입니다.

[Disclaimer](#)

공학박사학위논문

**A study on the rheological and electrical
properties of poly(lactic acid)/graphene
nanoplatelet composites by application of
electric field**

전기장 인가에 따른 폴리락틱산/그래핀
나노플레이트 복합체의 유변학적 및
전기적 특성에 관한 연구

2018년 2월

서울대학교 대학원

화학생물공학부

권 오 민

Abstract

A study on the rheological and electrical properties of poly(lactic acid)/graphene nanoplatelet composites by application of electric field

Kwon, Oh Min

School of Chemical and Biological Engineering

The Graduate School

Seoul National University

The goal of this thesis is to examine effect of electric field-induced graphene nanoplatelet (GNP) networks on rheological and electrical properties of poly(lactic acid) (PLA)/GNP composites and correlating between the composite properties and the GNP networks depending on concentration of GNPs or application intensity/time of the electric field.

For melt-compounded PLA composites containing GNPs at various, low volume fractions $\phi_{\text{GNP}} \leq 0.34$ vol%, this thesis focused on correlation between the composite properties and a large-scale structure of GNPs formed by a fixed, strong AC electric field (with the frequency and intensity of 60 Hz and 1.75 kV/mm, respectively). Optical microscopy, transmission electron microscopy, and 2D wide-angle X-ray diffraction measurements revealed that almost randomly oriented, thin stacks of GNPs in the as-fabricated composites were aligned by the electric field in the field direction and further organized into a column of stacks. This

columnar structure bridged two parallel plate electrodes when ϕ_{GNP} was above a threshold value, $\phi_{\text{GNP}}^* \cong 0.17$ vol%. Corresponding to this structural change, the liquid-like rheological response of the as-fabricated composites became the solid-like response, $G' \sim \omega^0$ at low ω (for the composites having $\phi_{\text{GNP}} \geq \phi_{\text{GNP}}^*$), after application of the electric field. In contrast, the loss modulus G'' was insensitive to the electric field and remained almost proportional to ω at low ω , suggesting that the columnar structure formed by the field was an elastic structure bridging the parallel plates. This bridge also served as an electrically conductive path between the plates so that an insulator-conductor transition occurred when the composites with $\phi_{\text{GNP}} \geq \phi_{\text{GNP}}^*$ were subjected to the electric field. Quantitative analysis of the equilibrium modulus and conductivity of the composites suggested that the field-induced columnar structure was not a rigid single slab but included the junctions being much softer and less conductive compared to the body of GNP. Moreover, analysis of the ϕ_{GNP} dependence of the equilibrium modulus and static electrical conductance after the transition ($\phi_{\text{GNP}} \geq 0.17$ vol%) suggested that an elastically inert secondary structure was formed by the GNP stacks remaining out the columnar structure (primary structure). This secondary structure appeared to be in *soft* contact with the primary structure to provide an extra conducting path.

Meanwhile, for a melt-mixed composite of PLA with GNPs having a fixed, low volume fraction $\phi_{\text{GNP}} = 0.34$ vol%, this thesis also examined growths of mechanical and electrical properties under an AC electric field of various intensities E for various times t_E , focusing on field-

induced GNP structures governing those properties. A fraction of randomly oriented GNPs was aligned by the field and then connected into columns, as suggested from optical microscopy. This structural evolution led to qualitatively similar growths of low-frequency storage modulus and static electrical conductivity. The key quantity for understanding this growth was a time t_E^* for occurrence of short circuit that detected formation of GNP columns conductively bridging the electrodes. The growths of both modulus and conductivity for various E were summarized as functions of a reduced variable, t_E/t_E^* , confirming the growths commonly reflected the evolution of the GNP columns. However, the modulus grew fast and leveled off by $t_E/t_E^* \sim 1$, whereas the conductivity kept growing gradually even at $t_E/t_E^* > 1$. This difference was discussed in relation to the matrix chains and residual GNPs out the column.

This thesis, which focused on the interrelation between the composites properties and the field-induced GNP structure, highlights the importance of controlling the microstructure of GNPs particularly for their orientation in order to realize the excellent intrinsic properties of GNPs still in the composites.

Keywords: electric field, graphene nanoplatelets, poly(lactic acid), biodegradable composites, polymer rheology, dielectric property

Student Number: 2014-30248

Contents

Abstract.....	i
List of Figures.....	vi
List of Table.....	xi
Chapter 1. Introduction	- 1 -
1.1. General introduction	- 2 -
1.2. Overview of thesis	- 7 -
Chapter 2. Background	- 9 -
2.1. Graphene nanoplatelet	- 10 -
2.2. Control of microstructure: Dispersion	- 12 -
2.3. Control of microstructure: Orientation	- 15 -
2.4. Objectives of thesis.....	- 21 -
Chapter 3. Experimental methods	- 22 -
3.1. Sample preparation	- 23 -
3.2. Application of electric field to composites.....	- 25 -
3.3. Visualization and X-ray scattering	- 27 -
3.4. Rheological measurement.....	- 29 -
3.5. Electrical measurement.....	- 31 -
Chapter 4. Results and discussion.....	- 33 -
4.1. Concentration-dependent changes by electric field.....	- 34 -
4.1.1. Electric field-induced structural changes	- 34 -
4.1.2. Rheological properties.....	- 45 -
4.1.3. Electrical properties.....	- 52 -

4.1.4.	Correlation between structure and properties.....	- 61 -
4.2.	Time/intensity-dependent changes by electric field	- 70 -
4.2.1.	Structure evolution under an electric field and evaluation of percolation time t_E^*	- 70 -
4.2.2.	Rheological properties.....	- 75 -
4.2.3.	Electrical properties.....	- 81 -
4.2.4.	Similarity and difference of the elasticity and conductance growths.....	- 87 -
4.2.5.	Further examination of time scale of structure formation	- 92 -
Chapter 5.	Summary	- 113 -
국문 초록	- 117 -
References		- 121 -

List of Figures

- Fig. 2.1.1** (a) Schematic illustration of GNP [55] (b) SEM image of GNP [56].....11
- Fig. 2.2.1** TEM micrographs of thermoplastic polyurethane (TPU) with (a) melt-blended 5 wt % (2.7 vol %) graphite, (b, c) melt-blended, (d) solvent-mixed, (e, f) in situ polymerized ~ 3 wt % (1.6 vol %) thermally reduced graphene oxide (TRG), (g) solvent-mixed 3 wt % (1.6 vol %) phenyl-isocyanate treated graphene oxide (Ph-iGO), (h) Acetylphenly-isocyanate treated graphene oxide (AcPh-iGO), and (i) in situ polymerized 2.8 wt % (1.5 vol %) GO. [51].....13
- Fig. 2.2.2** (a) Young's moduli E of graphene/TPU composites normalized by matrix modulus E_0 . (b) dc surface resistance of graphene/TPU composites. (c) N_2 permeability, P_{nitrogen} , of TPU composites normalized by permeability P_0 of unfilled TPU. All the abbreviations and symbols are noted in the caption of Fig. 2.2.1. [51].....14
- Fig. 2.3.1** (a) Digital photo of magnetized GNP/epoxy composites after being doped with Fe_3O_4 [30] (b) SEM micrographs of highly ordered Fe_3O_4 /GNPs in epoxy [30] (c) helium permeability measurements of GNP/epoxy composites and Fe_3O_4 /GNP-based epoxy composites after application of the magnetic field [30] (d) thermal conductivity of neat epoxy, epoxy/GNP composites (1 vol% of GNPs), and Fe_3O_4 /GNP-based epoxy composites (1 vol% of GNPs) in parallel and perpendicular magnetic alignment direction [28].....17
- Fig. 2.3.2** (a) Sample geometries depending on sample preparation methods and definition for 3 orthogonal directions (b) dc surface resistance of graphite and functionalized graphene sheets (FGS)/poly(carbonate) (PC) composites. D: denoted by circles. ~ 1 mm thick disks annealed for 48 h at 240 °C. F:

triangles. ~150 mm thick films from compression molding at 260 °C. B: rectangles. 10 cm × 3.25 mm × 12.8 mm injection molded bars. The inset compares dc surface resistance values measured on the polished and unpolished surface of graphite B samples. [36].....18

Fig. 2.3.4 Optical micrographs of GNPs in the liquid epoxy resin (0.054 vol%) during application of the AC electric field (25 V/mm). The positive and negative electrodes are denoted by “+” and “-”. [20].....19

Fig. 2.3.5 (a) Electrical conductivity (b) thermal conductivity (c) fracture energy G_{IC} of GNP/epoxy composites depending on the orientation states of GNPs at various GNP volume fractions. (The direction of the measurement of the properties with respect to the oriented direction of the GNPs is indicated.) [20].....20

Fig. 4.1.1 Optical micrographs (OM) of GNP composite with very low $\phi_{GNP} = 0.028$ vol% (a) before and (b) after application of the electric field (2.5 kV/mm, $f = 60$ Hz) for 75 min at 190 °C. The OM observation was also carried out for a composite with high $\phi_{GNP} = 0.17$ vol% (c) before and (d) after application of the electric field (1.75 kV/mm, $f = 60$ Hz) for 14 min at 190 °C. The direction of the applied electric field (EF) is indicated in parts b and d.....36

Fig. 4.1.2 2D wide-angle X-ray diffraction (2D WAXD) profiles of GNP composite with $\phi_{GNP} = 0.28$ vol% (a) before (denoted as “No EF”) and (b) after (denoted as “EF”) application of the electric field (1.75 kV/mm, $f = 60$ Hz). The most outer ring (denoted as “ $2\theta = 26.4^\circ$ ”) indicates diffraction from the 002 plane of graphene sheets being oriented parallel to the incident X-ray beam, namely in the direction normal to the sample surface. The electric field, when applied, was in parallel to the incident beam direction. The circular-average 1D WAXD profiles

obtained from the 2D profiles are shown in part c, together with the 1D profile of pure GNP powder (shown as a reference).....41

- Fig. 4.1.3** Low and high magnification TEM images of GNP composite with $\phi_{\text{GNP}} = 0.28$ vol% before (a and b) and after (c and d) application of the electric field (1.75 kV/mm, $f = 60$ Hz). The direction of the applied electric field (EF), *expected* from the WAXD data, is indicated in parts c and d.....43
- Fig. 4.1.4** Angular frequency (ω) dependence of storage modulus G' of GNP composites at 190 °C (a) before and (b) after application of the electric field (1.75 kV/mm, $f = 60$ Hz).....48
- Fig. 4.1.5** Angular frequency (ω) dependence of loss modulus G'' of GNP composites at 190 °C (a) before and (b) after application of the electric field (1.75 kV/mm, $f = 60$ Hz).....49
- Fig. 4.1.6** ϕ_{GNP} dependence of $G'(\omega = 0.1)$ of GNP composites at 190 °C before and after application of electric field (1.75 kV/mm, $f = 60$ Hz). Lines were drawn to guide the eye.....51
- Fig. 4.1.7** Angular frequency (ω) dependence of dynamic dielectric constant ϵ' (filled symbols) and dielectric loss ϵ'' (unfilled symbols) of GNP composites at 190 °C (a) before and (b) after application of the electric field (1.75 kV/mm, $f = 60$ Hz).....53
- Fig. 4.1.8** Angular frequency (ω) dependence of the imaginary part of dielectric modulus M'' of GNP composites at 190 °C (a) before and (b) after application of the electric field (1.75 kV/mm, $f = 60$ Hz).....57
- Fig. 4.1.9** ϕ_{GNP} dependence of phenomenological relaxation time, τ_{dc} before and after application of the electric field (1.75 kV/mm, $f = 60$ Hz). Lines were drawn to guide the eye.....58
- Fig. 4.1.10** ϕ_{GNP} dependence of σ_{dc} of GNP composites at 190 °C before and after application of the electric field (1.75 kV/mm, $f = 60$ Hz). Lines were drawn to guide the eye.....60
- Fig. 4.1.11** Schematics of a chained-stack structure (a) as a rigid single

- slab and (b) with junctions.....62
- Fig. 4.1.12** (a) Schematic illustration of chained-stacks (primary structure) and left-over stacks (secondary structure) in the composite. (b) TEM image of GNP composite with $\phi_{\text{GNP}} = 0.28$ vol% after application of the electric field ($E = 1.75$ kV/mm, $f = 60$ Hz).....69
- Fig. 4.2.1** Optical micrographs of GNP composite with $\phi_{\text{GNP}} = 0.028$ vol% subjected to the electric field ($E = 2.5$ kV/mm, $f = 60$ Hz) at 190 °C for times t_E as indicated. Circles and ellipse highlight characteristic structures of GNP stacks for respective t_E . The direction of the applied electric field (EF) is indicated in the image for $t_E = 19$ s. For the highlighted stack in the circles, the initial orientation angle (at $t_E = 0$) defined with respect to this field direction was $\theta_0 \cong 68^\circ$, and the angle at $t_E = 19$ s was $\theta' \cong 18^\circ$71
- Fig. 4.2.2** Angular frequency (ω) dependence of storage and loss moduli, G' (top panel) and G'' (bottom panel), of GNP composite with $\phi_{\text{GNP}} = 0.34$ vol% at 190 °C measured after application of the strong electric field ($E = 1.75$ kV/mm, $f = 60$ Hz) for the time t_E as indicated. Neat PLA data are also shown as a reference.....77
- Fig. 4.2.3** Evolution of low- ω modulus increment $\Delta G'(\omega = 0.1)$ of composite with $\phi_{\text{GNP}} = 0.34$ vol% at 190 °C on application of the strong AC electric field of the intensity E as indicated. $\Delta G'(\omega = 0.1)$ is plotted against the electric field application time t_E (top panel) and a reduced time t_E/t_E^* (bottom panel). Lines were drawn to guide the eye.....79
- Fig. 4.2.4** Angular frequency (ω) dependence of dynamic dielectric constant and dielectric loss, ϵ' (top panel) and ϵ'' (bottom panel), of GNP composite with $\phi_{\text{GNP}} = 0.34$ vol% at 190 °C measured after application of the strong electric field ($E = 1.75$ kV/mm, $f = 60$ Hz) for the time t_E as indicated. Neat PLA data are also

	shown as a reference.....	83
Fig. 4.2.5	Evolution of increment of dc conductivity $\Delta\sigma_{dc}$ of composite with $\phi_{GNP} = 0.34$ vol% at 190 °C on application of the strong AC electric field of the intensity E as indicated. $\Delta\sigma_{dc}$ is plotted against the electric field application time t_E (top panel) and a reduced time t_E/t_E^* (bottom panel). Lines were drawn to guide the eye.....	85
Fig. 4.2.6	Schematic illustration of GNP motion under a strong electric field. The direction of the applied AC electric field is indicated as EF (both-sided arrow).....	89
Fig. 4.2.7	Changes of the time t_E^* for formation of GNP columns under strong electric field with the field strength E observed for the composites with $\phi_{GNP} = 0.17, 0.28$ and 0.34 vol% at 190 °C. t_E^* is double-logarithmically plotted against E . Solid lines show results of power-law fitting. Dotted lines indicate a reference slope of -2 representing a relationship $t_E^* \propto E^{-2}$ expected for the simplest case.....	94
Fig. 4.2.8	Schematic illustration of alignment of GNP stacks for (a) rotational and (b) translational motion under electric field. The lines of electric flux representing the interaction between the induced dipoles of neighboring GNP stacks are schematically shown in (c).....	97
Fig. 4.2.9	Schematic illustration of possible sequential motions of GNPs serving for the rate-determining step: Connection of (a) 4 GNP stacks and (b) 3 GNP stacks.....	104

List of Table

Table 4.2.1 The average time t_E^* required for formation of GNP columns conductively connecting two electrodes in concentrated GNP/PLA composites subjected to the strong AC electric field at 190 °C.....	74
--	----

1. Introduction

1.1. General introduction

Graphene nanoplatelets (GNPs), multilayer carbon sheets with each layer having a hexagonal lattice structure, exhibit a high mechanical rigidity, high thermal and electrical conductivities, and low gas permeability due to their primary sheet structure. Extensive studies have been made for polymeric composites containing GNPs as a nano-sized filler because of those excellent properties as well as a large surface area of GNPs [1-8]. However, GNPs often form agglomerates in the composite due to their strong van der Waals attraction and lack of affinity with the polymer matrix, thereby diminishing their performance reflecting the primary structure. Therefore, it is a critical challenge to control the dispersion and orientation of GNPs to realize their performance in the composites. Dispersion of carbon-based fillers (including GNPs) has been successfully enhanced with several methods that involve *in-situ* polymerization [7], chemical modification [8], solution-mixing [9], and master-batch [10].

Attempts have been made also for controlling the orientation of those fillers. Several approaches, that include the use of the electric field [11-27], magnetic field [28-33], shear flow field [34-36], and multilayer co-extrusion [37], have been made to orient the fillers in the composites. In particular, the electric field orients carbon nanofibers [11, 12], carbon nanotubes [13-17], and carbon black [18, 19] in the field direction to improve the mechanical, electrical, and thermal properties of the

composites. This electric field-induced orientation has been examined also for composites containing GNPs [20-27]. Wu et al. reported that the orientation of GNPs in an epoxy resin could increase the electrical conductivity by 7-8 orders of magnitude, the fracture-toughness by 900%, and the thermal conductivity by 90% [20]. For composites of unsaturated polyester and GNPs, Chen et al. found that application of the electric field significantly improved the transmittance of visible light (due to reduction of light absorption and scattering) [23-25]. The increases in the electrical/thermal conductivity and the mechanical toughness on application of the strong electric field can be related to enhancement of the *connectivity* of the oriented GNPs that possibly resulted from an interaction of the field-induced dipoles (as explained later in more detail). This behavior makes a contrast to the decrease of electrical conductivity on shear-orientation [36], which would be related to shear-induced disruption of the connectivity between GNPs (in the absence of the induced dipole interaction).

Despite those studies for manipulating the properties of GNP composites, no attempt has been made to control rheological properties of GNP composites subjected to an electric field on the basis of rigid understanding of the *correlation* between the structure and properties. For related materials, clay dispersions in thermoplastic resins, Ahn's group previously attempted to characterize the effect(s) of an alternating current (AC) electric field on the rheological properties of dispersions

[38-42]. The structural change of the clays, enhanced exfoliation due to the interaction between the permanently polarized charges of the clay (giving *permanent* dipoles) and the electric field, was well correlated with the rheological properties.

On the basis of this result, in this thesis, it was attempted to correlate the structural change(s) of GNPs in poly(lactic acid) due to the strong AC electric field and the rheological and electrical properties, considering a fact that GNPs exhibit *induced* dipoles (not permanent dipoles similar to those of the clay). Optical microscopy, transmission electron microscopy, and 2D wide-angle X-ray diffraction measurements confirmed that thin stacks of GNPs were oriented but not exfoliated by the AC electric field (because of those induced dipoles immediately following the AC electric field) and further organized into an extended chain (or column) of stacks that bridged the electrodes unless GNPs were very dilute. The mechanical modulus and electrical conductivity were found to increase significantly on formation of this bridging structure. Despite this significant increase, quantitative analysis revealed that the modulus and conductivity of this chained-stack structure were still much lower than those of the body of GNP (each graphene nanoplate). This fact suggests that the chained-stack structure was not a rigid single slab but contained the junctions being much softer and less conductive compared to the body of GNP. Furthermore, residual GNP stacks out the chained-stack structure appeared to form a secondary structure being

elastically inert but still offering an extra conducting path to the chained-stacked structure, as suggested from the analysis of the equilibrium modulus and static electrical conductivity.

Considering the importance of this structure-property correlation in the GNP/PLA composites noted just above, it was also attempted to study *growth* of the electrical conductivity and low-frequency modulus with an application time t_E of the strong electric field in relation to the time-evolution of the GNP column under the field. The modulus and conductivity exhibited qualitatively similar growth with t_E . A key quantity for understanding this growth behavior was a time t_E^* for formation of electrically percolated GNP columns connecting the two electrodes: This t_E^* was measured as a time for occurrence of electrical short circuit under the strong electric field, and was in accord, in its magnitude, to a rough theoretical estimate of the time for translational motion of the GNP stack driven by an interaction between induced dipoles of the GNP stacks. The growths of the modulus and conductivity observed for various E were successfully summarized as functions of a single reduced variable, t_E/t_E^* , confirming that the growths commonly resulted from the evolution of GNP columns electrically connecting the two electrodes. However, quantitatively, the growth of the modulus was fast and leveled off by the reduced time $t_E/t_E^* \cong 1$, whereas the growth of conductivity was slower and continued up to $t_E/t_E^* \gg 1$. This difference was discussed in relation to the matrix PLA chains (that would have

mechanically connected neighboring GNP stacks thereby enlarging the modulus but not the conductivity) and also to the remaining GNP stacks out the column (these stacks could have *softly* connected neighboring columns at long times to continuously increase σ_{dc} without too much affecting the modulus). Details of these results are presented in this thesis.

1.2. Overview of thesis

This thesis comprises of introduction, background, experimental methods, results and discussion, and summary chapters.

Chapter 2 explains about the background of the thesis which is divided into three parts. Chapters 2.1 briefly describes basic characteristic features of graphene nanoplatelet (GNP), a key material used in this thesis. Chapters 2.2 and 2.3 highlight the importance of controlling microstructure of GNPs in polymer via controlling dispersion (Chapter 2.2) and orientation (Chapter 2.3) states of GNPs. Various techniques to control the dispersion and orientation of GNPs in order to improve multifunctional properties of polymers are introduced therein.

Chapter 3 describes experimental methods that are categorized into five parts. Chapter 3.1 involves material information of PLA and GNPs and composite preparation methods. A method to apply electric field to composites is described in Chapter 3.2. Furthermore, structural changes of GNPs under the field application were investigated via visualization techniques including optical microscopy and TEM as well as X-ray scattering. The experimental procedures for each technique to characterize those structural changes are explained in Chapter 3.3. In linear regimes (either in linear viscoelastic or linear dielectric response regimes), rheological and electrical properties of PLA/GNP composites were measured before and after application of the electric field by

varying the GNP concentration or application intensity/time of the field, and their experimental procedures are presented in Chapters 3.4 and 3.5.

In Chapter 4, results of structure and property changes of PLA/GNP composites under the field application are presented and the correlation between the two is discussed. Chapter 4.1 involves concentration-dependent changes in the structure and properties by the field application while a strong but fixed field intensity was applied up to occurrence of electrical short circuit. Meanwhile, Chapter 4.2 focuses on field application time/intensity-dependent changes in the structure and properties, thus various field intensities and time were applied to a composite having a fixed, low volume fraction of GNPs. In both parts, the structures and the properties are well correlated.

Finally, Chapter 5 summarizes the results of the correlation between the field-induced GNP structure and the composite properties.

2. Background

2.1. Graphene nanoplatelet

Graphene is a two-dimensional (2-D) carbon sheet comprised of sp^2 carbon atoms arranged into a hexagonal lattice structure. Graphene nanoplatelet (GNP) is made of individual single graphene sheets stacked together on top of one another by van der Waals forces (cf. Fig. 2.1.1). Particularly, graphene (including GNP) is a promising nano-sized filler, offering combined advantages of both carbon nanotube (CNT) and layered silicate. Its outstanding electrical and thermal properties makes itself being superior to layered silicate. In addition, these 2-D carbon sheets can provide exceptional gas barrier properties over one-dimensional CNT. Overall, graphene has a high in-plane stiffness (~ 1 TPa [43-45]), a high thermal conductivity ($\sim 400 \text{ W m}^{-1} \text{ K}^{-1}$ [46]) and a high electrical conductivity ($\sim 10^8 \text{ S m}^{-1}$ [47, 48]). These properties in addition to very large surface area and gas barrier properties greatly encourage the use of graphene (in either pristine sheet form or layered form) as reinforcement to enhance multifunctional properties of polymers including electrical, thermal, mechanical, and gas barrier properties. [2, 4, 6, 36, 45, 49-54].

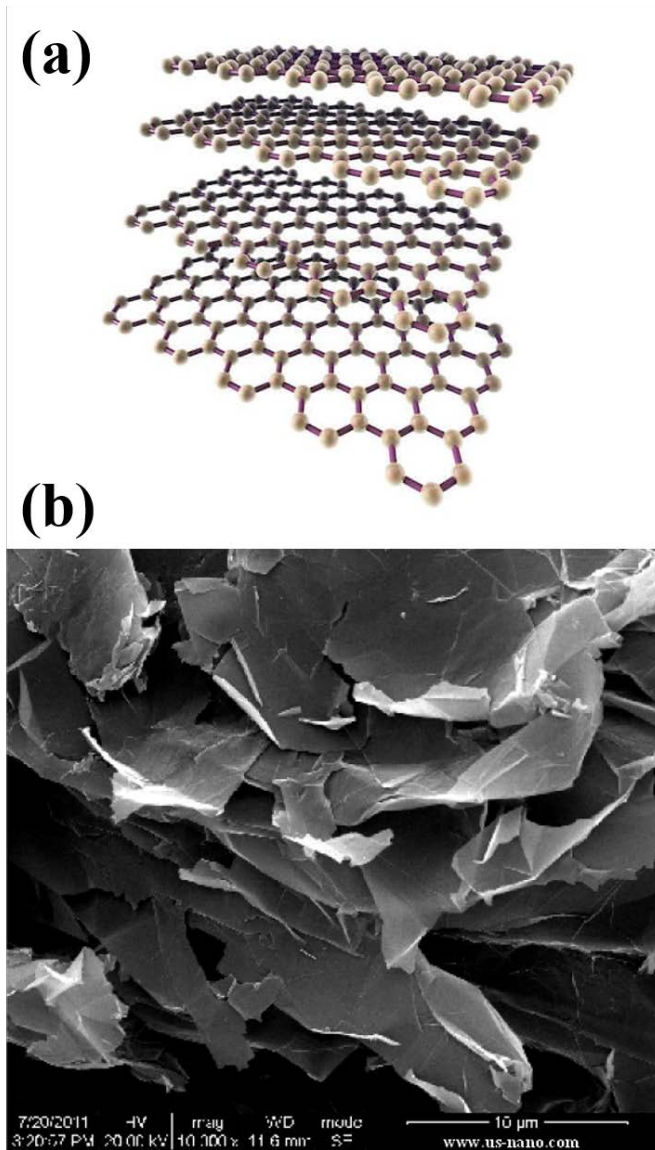


Fig. 2.1.1 (a) Schematic representation of GNP [55] (b) SEM image of GNP [56]

2.2. Control of microstructure: Dispersion

Despite those exceptional intrinsic properties of GNP, its incorporation into polymers as reinforcement have not been easily attained since GNPs often agglomerate with each other due to their strong van der Waals attraction, thus their intrinsic/outstanding properties are not reflected in the composites properties. Therefore, it is highly desired to control the microstructure by controlling dispersion and orientation of GNPs thereby effectively transferring their excellent properties to the composites.

Numerous methods have been implemented in order to control the dispersion state of GNPs to achieve better multifunctional properties of polymers. Kim et al. [51] utilized various dispersing techniques, (e.g., melt-mixing, solvent casting, in-situ polymerization, and chemical modification) to improve solid-state properties of graphite-derivatives composite including mechanical, electrical, and gas-barrier properties. Depending on the dispersing techniques, different dispersion states of the graphite-derivatives such as graphite, graphene oxide (GO), thermally reduced graphene oxide (TRG), and isocyanate treated graphene oxide (i-GO) were achieved as illustrated in Fig. 2.2.1. These different dispersion states had different effects on the mechanical, electrical, and gas barrier properties as noted in Fig. 2.2.2. The thinner the graphene sheets are, the better the composite properties become.

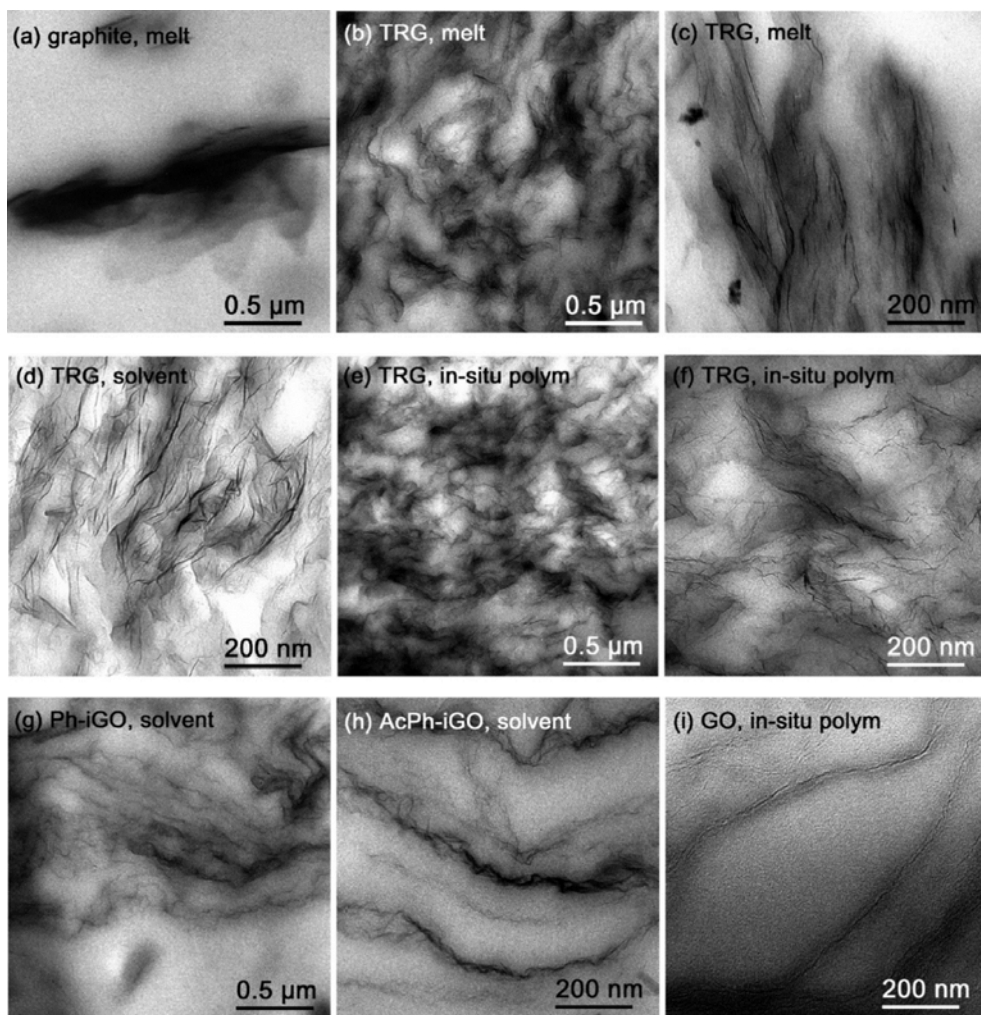


Fig. 2.2.1 TEM micrographs of thermoplastic polyurethane (TPU) with (a) melt-blended 5 wt % (2.7 vol %) graphite, (b, c) melt-blended, (d) solvent-mixed, (e, f) in-situ polymerized ~ 3 wt % (1.6 vol %) thermally reduced graphene oxide (TRG), (g) solvent-mixed 3 wt % (1.6 vol %) phenyl-isocyanate treated graphene oxide (Ph-iGO), (h) acetylphenyl-isocyanate treated graphene oxide (AcPh-iGO), and (i) in-situ polymerized 2.8 wt % (1.5 vol %) GO. [51]

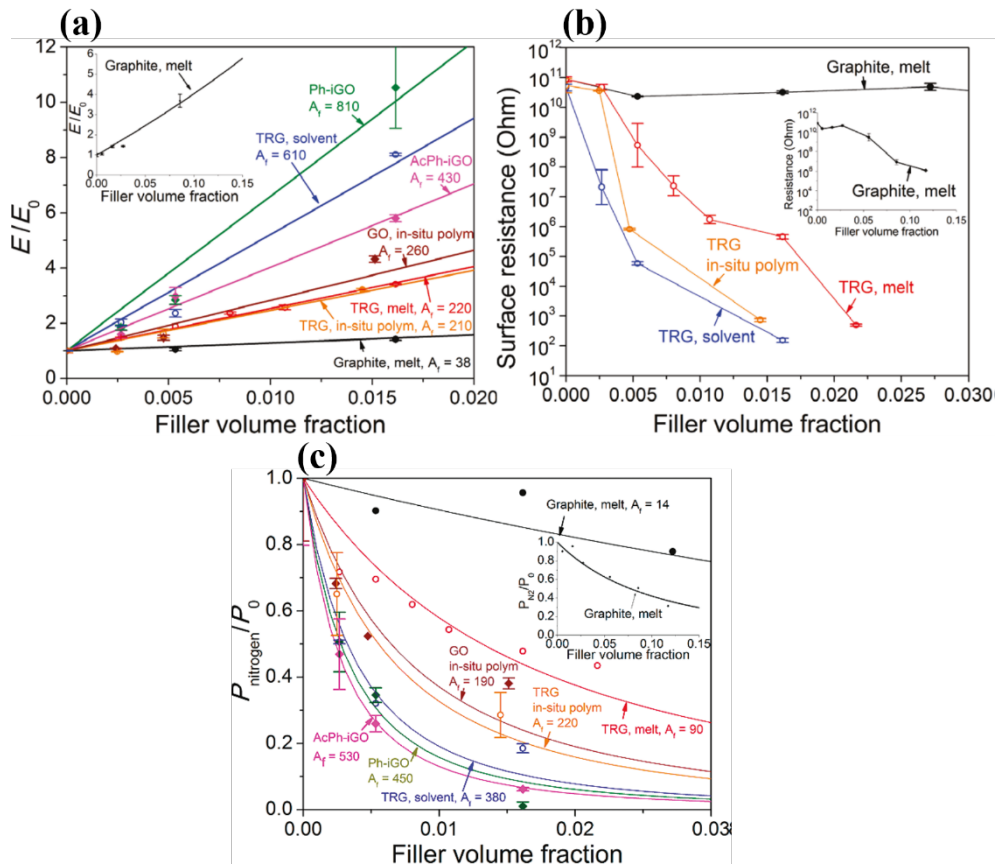


Fig. 2.2.2 (a) Young's moduli E of graphene/TPU composites normalized by matrix modulus E_0 . (b) dc surface resistance of graphene/TPU composites. (c) N_2 permeability, P_{nitrogen} , of TPU composites normalized by permeability P_0 of unfilled TPU. All the abbreviations and symbols are noted in the caption of Fig. 2.2.1. [51]

2.3. Control of microstructure: Orientation

Controlling orientation of GNPs is another viable option to control microstructure of GNPs in polymer.

One of the effective approaches to align GNPs is to use magnetic field. With Fe_3O_4 magnetic nanoparticles attached on the surface of GNPs, Jiao et al. [30] succeeded to improve gas barrier properties by aligning $\text{Fe}_3\text{O}_4/\text{GNP}$ into a highly ordered/aligned structure in epoxy using a low magnetic field (cf. Figs. 2.3.1a-c). Similarly, Yan et al. [28] also reported nearly 500% increase in thermal conductivity of $\text{Fe}_3\text{O}_4/\text{GNP}$ -based epoxy composites after application of the magnetic field when comparing with that of just GNP/epoxy composite (cf. Fig. 2.3.1d).

Another effective way to manipulate orientation of GNPs is to utilize shear flow field. Kim et al. [36] tried to apply strong shear flow field to graphite or functionalized graphene sheets (FGS) via compression and injection moldings, as illustrated in Fig. 2.3.2. These as-fabricated/highly aligned samples were then annealed for sufficiently long time to turn the shear-aligned sheets into isotropic state. From the measurement of electrical conductivity, the higher electrical percolation threshold was noted for the as-fabricated/highly aligned samples than the annealed ones having isotropic state of the sheets (cf. Fig. 2.3.3), possibly resulted from the shear flow-induced disruption of connectivity between the sheets.

Another highly efficient approach to align GNPs is to apply electric

field. Wu et al. [20] tried to manipulate orientation of GNPs in epoxy resin by applying an AC electric field. After 20 min application of the field, connected/columnar structures of GNPs were formed as revealed in Fig. 2.3.3. This formation of the columnar structure by the field enhanced electrical/thermal conductivity and fractural toughness of the GNP/epoxy composites than those fabricated without application of the field as noted in Fig. 2.3.4. Unlike shear flow field examined above, electric field promotes the connectivity between GNPs because of the interaction between induced dipoles (as already explained in Chapter 1.1) thereby increasing electrical conductivity after application of the electric field. This is possibly resulted from the GNP columnar structure formed by the field acting as an electrical path for charge carriers to travel.

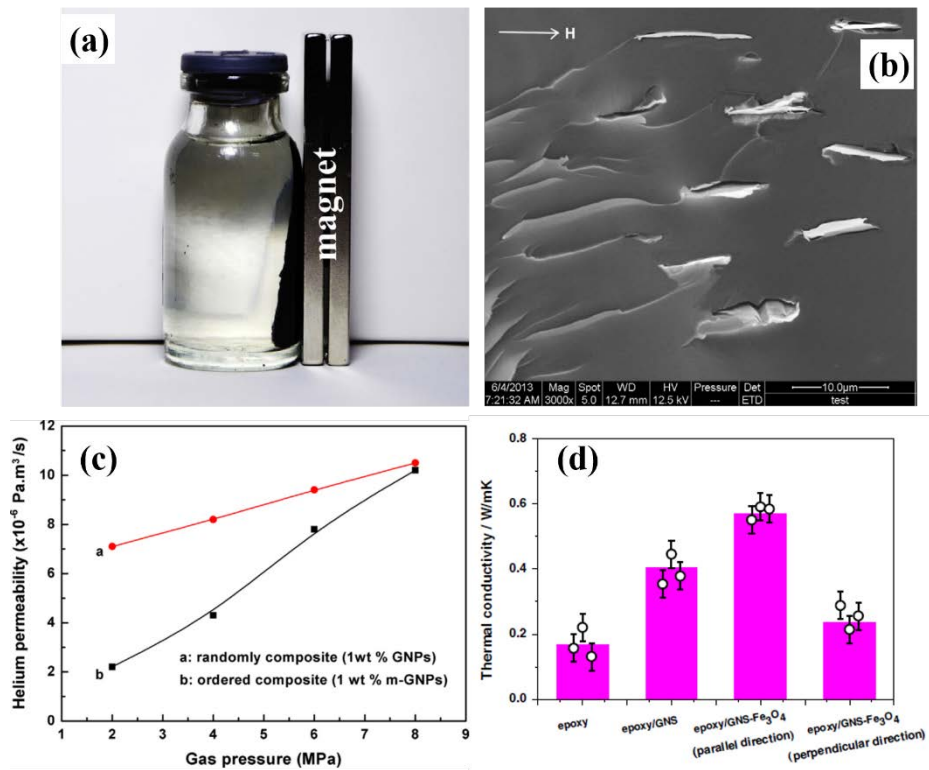


Fig. 2.3.1 (a) Digital photo of magnetized GNP/epoxy composites after being doped with Fe_3O_4 [30] (b) SEM micrographs of highly ordered Fe_3O_4 /GNPs in epoxy [30] (c) helium permeability measurements of GNP/epoxy composites and Fe_3O_4 /GNP-based epoxy composites after application of the magnetic field [30] (d) thermal conductivity of neat epoxy, epoxy/GNP composites (1 vol% of GNPs), and Fe_3O_4 /GNP-based epoxy composites (1 vol% of GNPs) in parallel and perpendicular magnetic alignment direction. [28]

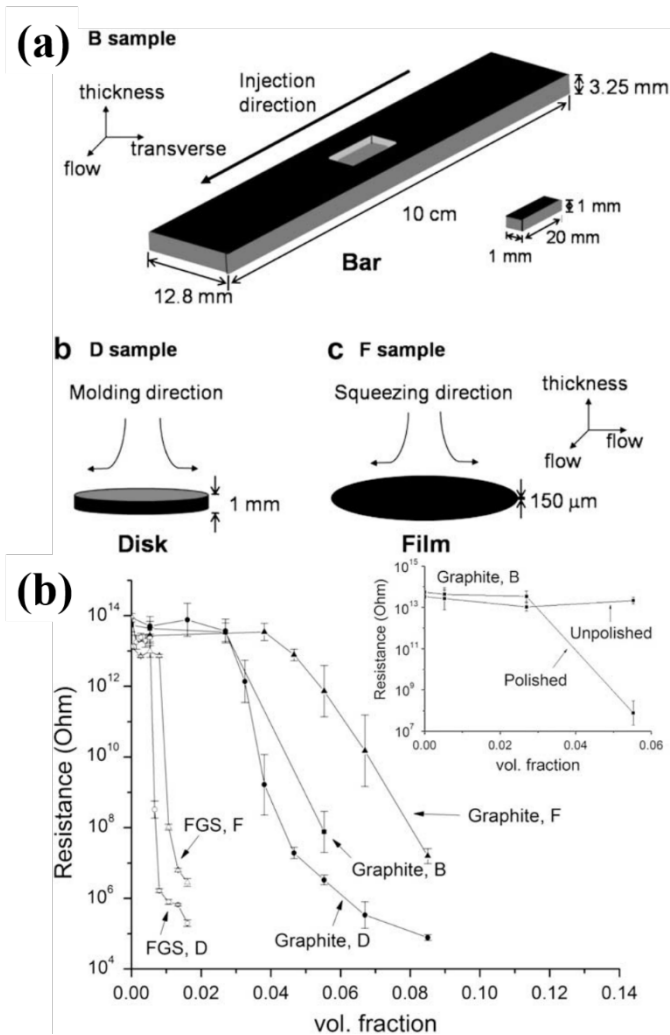


Fig. 2.3.2 (a) Sample geometries depending on sample preparation methods and definition for 3 orthogonal directions (b) dc surface resistance of graphite and functionalized graphene sheets (FGS)/poly(carbonate) (PC) composites. D: denoted by circles. ~1 mm thick disks annealed for 48 h at 240 °C. F: triangles. ~150 mm thick films from compression molding at 260 °C. B: rectangles. 10 cm × 3.25 mm × 12.8 mm injection molded bars. The inset compares dc surface resistance values measured on the polished and unpolished surface of graphite B samples. [36]

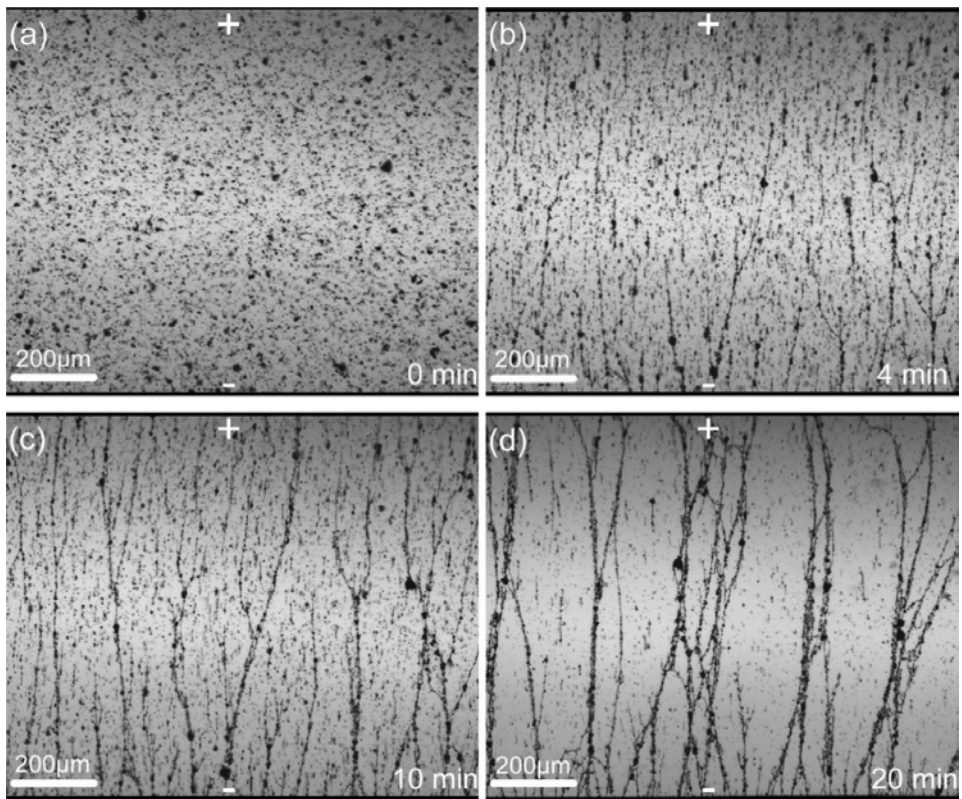


Fig. 2.3.3 Optical micrographs of GNPs in the liquid epoxy resin (0.054 vol%) during application of the AC electric field (25 V/mm). The positive and negative electrodes are denoted by “+” and “-”. [20]

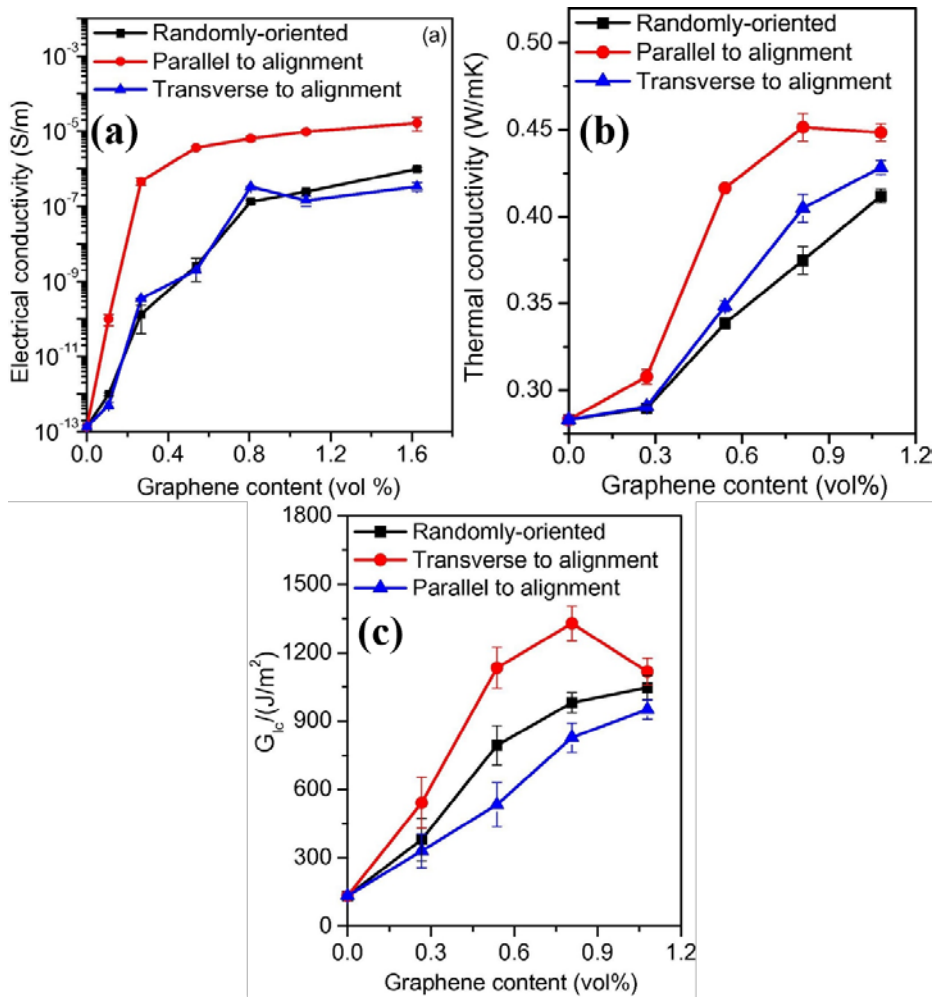


Fig. 2.3.4 (a) Electrical conductivity (b) thermal conductivity (c) fracture energy G_{IC} of GNP/epoxy composites depending on the orientation states of GNPs at various GNP volume fractions. (The direction of the measurement of the properties with respect to the oriented direction of the GNPs is indicated.) [20]

2.4. Objectives of thesis

This thesis aims to study the effect of AC electric field-induced GNP networks on the rheological and electrical properties of PLA/GNP composites on the basis of the correlation between the higher order structures of GNPs formed by the field and the composite properties. These objectives were accomplished based on the results of the rheological/electrical measurements of PLA/GNP composites under the applied field by varying the GNP concentration (Chapter 4.1) or application time/intensity of the electric field (Chapter 4.2). This thesis provides valuable insight about dynamics of GNPs under the field application that is a fundamental study of GNP-based composites.

3. Experimental methods

3.1. Sample preparation

3.1.1. Raw materials

Poly(lactic acid), PLA (grade 4032D, $M_w = 181$ kg/mol, $M_w/M_n = 2.01$) was provided by Natureworks (USA). Graphene nanoplatelets, GNPs (grade N008-100-P-40), were purchased from Angstrom Materials, Inc. (USA) and used as received. According to the manufacturer's designation, the average length and width of the platelets were ≤ 10 μm and the thickness was in the range of 50-100 nm. The carbon content of the corresponding GNP was ≥ 97 wt% with the oxygen content being ≤ 1 wt%, as indicated by the manufacturer's technical data sheet.

3.1.2. Composites preparation

The composite components, GNPs and PLA samples, were dried in a vacuum oven overnight at 80 °C, and then melt-mixed for 6 min at 210 °C with an intensive mixer (Rheocomp mixer 600, MKE, Korea) operated at a screw speed of 100 rpm. The composites thus prepared were compressed into disks with the thickness of 0.45 mm and diameter of 25 mm using a hot press (CH4386, Carver, USA) at 210 °C for 6 min. Those disks matched, in size, with the parallel plates utilized in the rheological and electrical measurements.

The GNP weight fraction in the composite, W_{GNP} , was set at 0 (neat PLA), 0.05, 0.1, 0.3, 0.5, and 0.6 wt%. The corresponding GNP volume fraction was $\phi_{\text{GNP}} = 0, 0.028, 0.06, 0.17, 0.28,$ and 0.34 vol%. (Assuming

the volume additivity, ϕ_{GNP} was calculated from W_{GNP} and the PLA weight fraction W_{PLA} as $\phi_{\text{GNP}} = (W_{\text{GNP}}/\rho_{\text{GNP}})/\{(W_{\text{GNP}}/\rho_{\text{GNP}}) + (W_{\text{PLA}}/\rho_{\text{PLA}})\}$, with $\rho_{\text{GNP}} \approx 2.20 \text{ g/cm}^3$ and $\rho_{\text{PLA}} \approx 1.24 \text{ g/cm}^3$ being the densities of GNP and PLA specified by the manufacturers.) At these low volume fractions, as-fabricated composites contained no conductive (electrically percolated) network of GNPs thereby exhibiting no electrical short circuit.

3.2. Application of electric field to composites

A parallel plate fixture of a conventional rheometer (RMS-800, Rheometrics, USA) was redesigned to allow a sample between the plates to be subjected to an alternating current (AC) electric field of high intensity. Detailed information about the setup of the rheometer including the parallel plate electrodes (made of stainless steel) has been given in Ref. [42]. The AC electric field was generated with a function generator (Tektronix AFG 310) and a high voltage amplifier (Trek 677B), and the voltage drop across the entire circuit was detected by a digital oscilloscope (Tektronix TDS210).

For the part of the analysis in Chapter 4.2, to the composites with $\phi_{\text{GNP}} = 0.17, 0.28, \text{ and } 0.34 \text{ vol\%}$ at $190 \text{ }^\circ\text{C}$, the AC electric field of the intensity $E = 1.10, 1.25, 1.50, 1.62, 1.75, \text{ and } 1.90 \text{ kV/mm}$ and a fixed frequency $f = 60 \text{ Hz}$ was applied for different times, t_E . For each of these composites, electrical short circuit occurred on application of the field for a certain time, t_E^* . This t_E^* , evaluated as an average obtained for at least three different specimens, specifies the time for formation of electrically percolated GNP columns connecting the two electrodes. (Significant current leakage occurred for $E > 1.90 \text{ kV/mm}$, which limited the experiment to determine t_E^* and measure rheological and electrical properties after application of the electric field only for $E \leq 1.90 \text{ kV/mm}$.)

Separately from the experiments in the rheometer explained above, the electric field was applied to the composites also on an optical

microscope (OM) stage for direct observation of the structure therein. The composite samples were sandwiched between thin polyimide films with a spacer, and a pair of parallel electrodes separated at a gap of 0.45 mm (same gap as in the rheometer) was embedded in the sample to apply the electric field. The sample thickness (spacer thickness) was chosen according to the optical transmittance of the sample. The OM images (for the transmitted light) detected the spatial distribution of GNPs superposed along the sample thickness direction.

In the experiments either in the rheometer or on the OM stage, the AC electric field at a fixed frequency of 60 Hz was applied to the GNP composite samples at 190 °C. In Chapter 4.1, the AC electric field intensity was set at 1.75 kV/mm, except for the composite with the lowest $\phi_{\text{GNP}} = 0.028$ vol% (that was only subjected to the OM observation). The short circuit occurred when concentrated GNPs were oriented under the electric field to form a conductive path bridging the electrodes. The time needed for occurrence of the short circuit decreased with increasing ϕ_{GNP} . In Chapter 4.2, the AC electric field was applied with varying field intensity E , 1.10-1.90 kV/mm for different application time t_E , 0-10 min. The rheological and electrical properties of the samples were measured at 190 °C immediately after the strong electric field was switched off on occurrence of the short circuit (Chapter 4.1) or different time interval t_E (Chapter 4.2), whereas the OM observation was carried out without switching off the field.

3.3. Visualization and X-ray scattering

For visualization of GNP columnar structure in the composites, μm -sized images were taken using an optical microscope (BX51, Olympus, Japan) under the electric field. High resolution optical images were successfully obtained for the composites having $\phi_{\text{GNP}} \leq 0.17$ vol%, with adequate choices of the sample thickness for OM observation that decreased from 0.45 mm (for the smallest ϕ_{GNP} examined, 0.028 vol%) to 0.2 mm (for $\phi_{\text{GNP}} = 0.17$ vol%). For the composite with larger ϕ_{GNP} (e.g., 0.28 vol%), the GNPs covered the whole optical view field (even for the smallest attainable sample thickness of 0.2 mm) to give just black OM images owing to their low light transmittance. Thus, the OM observation could be made only for $\phi_{\text{GNP}} \leq 0.17$ vol%.

In particular, for the dilute composite with $\phi_{\text{GNP}} = 0.028$ vol%, rotational motion of single GNP stack (highlighted as a circle in Fig. 4.2.1) was examined with the above OM observation during application of the electric field of the intensity $E = 2.5$ kV/mm ($f = 60$ Hz). (For larger ϕ_{GNP} , the images of stacks overlapped heavily and the rotation of single stack was not clearly resolved.) The change in the angle of the single stack in the dilute composite with respect to the electric field was used as the input parameter to theoretically estimate, in Chapter 4.2.5, the rotational time of the stack under the applied field, t_r .

For a composite containing $\phi_{\text{GNP}} = 0.28$ vol%, Transmission Electron Microscopy (TEM) was used to take nm-sized images. JEM 2100F

(JEOL, Japan) was operated at an accelerating voltage of 200 kV to obtain this TEM image. For this composite, the alignment of GNPs was also examined with 2D wide-angle X-ray diffraction (2D WAXD) covering the scattering angle 2θ ranging from 5° to 35° . The 2D WAXD measurement (operated in a transmission mode) was conducted with the D/MAX-2500 (RIGAKU, Cu-K α radiation with the wavelength $\lambda = 0.154$ nm) operated at an acceleration voltage of 50 kV with an exposure time of 8 h. For pure GNP powder, the diffraction peak at $2\theta = 26.4^\circ$ (due to the 002 plane of the graphene sheet) was confirmed by the 1D WAXD measurement conducted with the Bruker D8 advance covering the scattering angle 2θ ranging from 5° to 35° .

3.4. Rheological measurement

In Chapter 4.1, for the GNP composites with $\phi_{\text{GNP}} \geq 0.06$ vol% (*i.e.*, $\phi_{\text{GNP}} = 0.06, 0.17, 0.28,$ and 0.34 vol%) as well as neat PLA (matrix utilized for the composites), rheological measurements were conducted with a strain-controlled rheometer (RMS-800, Rheometrics, USA) at 190 °C immediately after *in-situ* application of the strong AC electric field ($f = 60$ Hz) having a fixed intensity of 1.75 kV/mm at the same temperature. A dynamic strain sweep test was made at a fixed angular frequency of $\omega = 1$ rad/s in order to find the linear viscoelastic regime. Within this linear viscoelastic regime, a dynamic frequency sweep test was carried out at $\omega = 0.1 - 100$ rad/s to obtain the complex modulus, $G^*(\omega) = G'(\omega) + jG''(\omega)$ with $j = \sqrt{-1}$. In this study, those $G^*(\omega)$ data are presented as plots of the storage and loss moduli, $G'(\omega)$ and $G''(\omega)$, against ω .

In Chapter 4.2, for the representative GNP composite with a fixed concentration of $\phi_{\text{GNP}} = 0.34$ vol%, rheological measurements were conducted at 190 °C immediately after *in-situ* application of the strong AC electric field ($f = 60$ Hz) having various intensities, $E = 1.10, 1.25, 1.50, 1.75,$ and 1.90 kV/mm, for different interval of time, $t_E = 0-8$ min, at the same temperature. Dynamic frequency sweep tests were carried out at angular frequencies $\omega = 0.1 - 100$ rad/s in the linear viscoelastic regime (strain amplitude $\gamma_0 = 0.19$) to obtain the storage and loss moduli, $G'(\omega)$ and $G''(\omega)$. Each test was carried out for a freshly loaded

composite sample having experienced the strong electric field of given E and t_E .

A dynamic time sweep test for the neat PLA sample was conducted at 190 °C for 30 min at 1 rad/s and no detectable change in the modulus was found. This result ensured lack of detectable degradation of PLA (in the neat and composite samples) within the interval of time (~ 30 min) of all experimental procedures for obtaining the data reported in this thesis. (The procedures included melting/annealing of the sample, application of the strong electric field, and dynamic frequency sweep or the dielectric measurement explained in Chapter 3.5.).

It should be also noted that the $G^*(\omega)$ data of the composites were reproduced in the second run of frequency sweep immediately following the first run conducted just after the strong electric field was switched off. This fact indicates that the electric field-oriented structure did not change within the time scale of the experiments carried out in this study because the GNP stacks were large (having a size of a few μm) and the PLA matrix was quite viscous (with the viscosity ~ 1000 Pa·s at 190 °C): The Brownian motion of the stacks in the composites should be very slow in the absence of the strong electric field.

3.5. Electrical measurement

In Chapter 4.1, for the GNP composites with $\phi_{\text{GNP}} \geq 0.06$ vol% (*i.e.*, $\phi_{\text{GNP}} = 0.06, 0.17, 0.28,$ and 0.34 vol%) as well as neat PLA (matrix utilized for the composites) before and after application of the strong electric field, the complex dielectric permittivity, $\varepsilon^*(\omega) = \varepsilon'(\omega) + j\varepsilon''(\omega)$ with $j = \sqrt{-1}$ were measured at 190°C with an SI 1260 impedance/gain-phase analyzer and a 1296 dielectric interface (Solartron, Cambridge, U.K.). The measurements were made for freshly loaded samples at angular frequencies $\omega = 10^1$ - 10^7 rad/s, utilizing the parallel plates in the rheometer as the electrodes. In the measurement, the amplitude of the oscillatory electric field was kept small (2.5 V/mm) so as to ensure the linearity of the dielectric response of the samples. In this study, the electrical behaviors of the GNP composites are presented as plots of the dynamic dielectric constant $\varepsilon'(\omega)$ and dielectric loss $\varepsilon''(\omega)$ against ω .

In Chapter 4.2, for the representative composite ($\phi_{\text{GNP}} = 0.34$ vol%), the dynamic dielectric constant and dielectric loss, $\varepsilon'(\omega)$ and $\varepsilon''(\omega)$ at angular frequencies $\omega = 10^2$ - 10^7 rad/s, were also measured at 190°C immediately after *in-situ* application of the strong electric field of various E (1.10, 1.25, 1.50, 1.75, and 1.90 kV/mm at $f = 60$ Hz) for different times, $t_E = 0$ -10 min, at the same temperature. Each measurement was conducted for a freshly loaded composite sample having experienced the

strong electric field of given E and t_E .

For all systems at low ω , $\varepsilon''(\omega)$ was inversely proportional to ω and direct current (dc) conductance was observed. The dc conductivity σ_{dc} was evaluated from the $\varepsilon''(\omega)$ data at such low ω as $\sigma_{dc} = \varepsilon_0[\omega\varepsilon''(\omega)]_{\omega \rightarrow 0}$, where ε_0 is the absolute permittivity of vacuum ($\varepsilon_0 = 8.854 \times 10^{-12}$ F/m). For discussion of a phenomenological relaxation time τ_{dc} related to this dc conductance, the $\varepsilon^*(\omega)$ data were also converted into the complex dielectric modulus $M^*(\omega)$ defined by

$$M^*(\omega) = M'(\omega) + jM''(\omega) = \frac{1}{\varepsilon^*(\omega)} \quad (j = \sqrt{-1}) \quad (3.5.1)$$

The time τ_{dc} was evaluated from the peak frequency of the imaginary part of this modulus, $M''(\omega)$.

4. Results and discussion

4.1. Concentration-dependent changes by electric field

For the melt-compounded PLA composites containing GNPs at various, low volume fractions $\phi_{\text{GNP}} \leq 0.34$ vol%, this chapter focused on correlation between the composite properties and a large-scale structure of GNPs formed by a fixed, strong AC electric field (with the frequency and intensity of 60 Hz and 1.75 kV/mm, respectively). Details of the results are presented in this chapter.

4.1.1. Electric field-induced structural changes

Figs. 4.1.1a and 4.1.1b present optical micrographs of a GNP composite with $\phi_{\text{GNP}} = 0.028$ vol% before and after application of the strong AC electric field (2.5 kV/mm, $f = 60$ Hz) for 75 min at 190 °C. No further structural change was observed on application of the electric field for a longer time. Furthermore, no electrical short circuit was detected and thus no direct conductive path of GNPs connecting the two electrodes was formed in the dilute composite examined ($\phi_{\text{GNP}} = 0.028$ vol%).

Before application of the electric field (Fig. 4.1.1a), GNPs appear to be organized in thin stacks but form no large agglomerates, and those stacks are well dispersed randomly in the PLA matrix of the composite. This good dispersion was achieved during the mechanical mixing on preparation of the composites. In contrast, after application of the field (Fig. 4.1.1b), the thin stacks of GNPs are aligned in the direction of the

electric field and further organized into a chain (or column) of stacks oriented in that direction, without exhibiting significant exfoliation. This structural change occurred quite possibly due to the anisotropy in the electric field-induced dipole of each graphene sheet: The polarization of the electron cloud of this sheet, occurring instantaneously and thus oscillating synchronously with the electric field, is much larger in the direction parallel along the sheet than in the normal direction, so that the interaction of the induced dipole with the electric field tends to orient the stack of GNPs in the field direction. Because of this synchronous feature of the polarization, the induced dipole is always in the direction of the electric field thereby allowing the GNP stacks, having a meso-scale size and being embedded in a viscous PLA medium, to slowly but steadily rotate/orient in the field direction. The interaction between the induced dipoles of neighboring stacks would have further organized the stacks into a chain-like (or columnar) structure oriented in the field direction.

This behavior makes a strong contrast with the enhanced exfoliation of the clays due to the AC field without significant orientation [38-42]: The clays have permanent charge polarization (*permanent* dipoles) and the interaction of those dipoles with the *high-frequency* AC electric field does not allow large clay sheets having a low mobility to rotate and orient in a way synchronized with the field. Thus, the orientation of GNPs without significant exfoliation is a characteristic feature of GNPs having just induced dipoles.

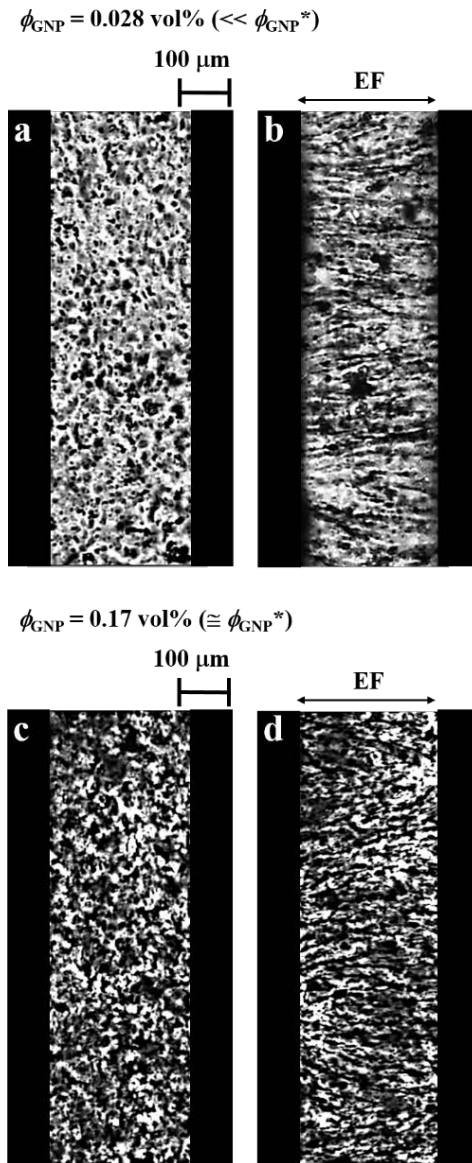


Fig. 4.1.1 Optical micrographs (OM) of GNP composite with a very dilute $\phi_{\text{GNP}} = 0.028 \text{ vol}\%$ (a) before and (b) after application of the electric field (2.5 kV/mm, $f = 60 \text{ Hz}$) for 75 min at 190 °C. The OM observation was also carried out for a composite with a concentrated $\phi_{\text{GNP}} = 0.17 \text{ vol}\%$ (c) before and (d) after application of the electric field (1.75 kV/mm, $f = 60 \text{ Hz}$) for 14 min at 190 °C. The direction of the applied electric field (EF) is indicated in b and d.

The optical micrographic (OM) observation was attempted also for concentrated composites having $\phi_{\text{GNP}} \gg 0.028$ vol%. It turned out $\phi_{\text{GNP}} = 0.17$ vol% was the highest GNP content giving clear OM images with the attainable sample thickness of 0.2 mm, and the composites with larger ϕ_{GNP} gave just black OM images, as explained earlier in Chapter 3.3. Figs. 4.1.1c and 4.1.1d present the OM images for this highest ϕ_{GNP} obtained before and after application of the electric field (1.75 kV/mm, $f = 60$ Hz) for a time $t_E = 14$ min at 190 °C. (The short circuit happened on application of the electric field for 14 min.) As noted in Figs. 4.1.1c and 4.1.1d, clear OM images were obtained for $\phi_{\text{GNP}} = 0.17$ vol% because the sample thickness was chosen to be the smallest attainable value of 0.2 mm (which was considerably smaller than the thickness 0.45 mm utilized for the dilute composite examined in Figs. 4.1.1a and 4.1.1b.)

Comparing the images shown in Figs. 4.1.1a and 4.1.1c, it is noted that the concentrated GNP stacks ($\phi_{\text{GNP}} = 0.17$ vol%) before application of the electric field were almost randomly oriented, as similar to the dispersion state of dilute GNP stacks ($\phi_{\text{GNP}} = 0.028$ vol%). After application of the field for the time $t_E = 14$ min, those concentrated GNP stacks were largely oriented in the field direction, again as similar to the behavior of dilute GNP stacks. However, it is also important to note a difference: The concentrated GNP stacks exhibited the short circuit and thus they should have conductively bridged the electrodes (though not clearly resolved in Fig. 4.1.1d) at the field application time of $t_E = 14$ min,

whereas the dilute GNP stacks remained without the short circuit even for much longer t_E (= 75 min). The bridge due to the concentrated GNP stacks becomes a key in the later discussion of the viscoelastic and electrical properties.

In order to further verify the electric field-induced orientation of concentrated GNP stacks, 2D WAXD observation (in a transmission mode) was conducted for the composite with $\phi_{\text{GNP}} = 0.28$ vol% (larger than that examined in Figs. 4.1.1c and 4.1.1d). The results are shown in Fig. 4.1.2. The incident X-ray beam was introduced in the direction normal to the composite sample surface, that is, in the direction of the electric field when applied to the composite. In the 2D WAXD profiles of the composite before and after application of the electric field for 6 min (Figs. 4.1.2a and 4.1.2b), the most outer ring (denoted as “ $2\theta = 26.4^\circ$ ”) indicates diffraction from the 002 plane of graphene sheets being oriented parallel to the incident X-ray beam. The profiles are circularly symmetric either before or after application of the electric field, indicating that the electric field did not significantly affect the orientation of the GNP stacks *within* a plane normal to the electric field (within a plane parallel to the surface sample).

However, the electric field *did induce* the orientation of GNP stacks in the field direction, as noted in Fig. 4.1.2c where the circular-average 1D WAXD profiles before and after application of the electric field (obtained from the 2D profiles) are plotted against the scattering angle

2θ . These 1D profiles of the composites (black and red curves) are normalized at the broad peak at $2\theta \sim 17^\circ$ (due to the PLA matrix) for convenience of direct comparison of the diffraction peak from the graphene sheet emerging at $2\theta = 26.4^\circ$. This graphene peak is similarly sharp for the composite before and after application of the electric field (solid curves) as well as for the pure GNP powder (dashed curve) shown here as a reference. However, the peak intensity of the composite becomes significantly larger after application of the electric field (solid red curve), indicating that the concentrated GNP stacks in the composite was largely oriented in the field direction (parallel to the X-ray beam).

More quantitatively, the magnitude of the electric field-induced orientation of the GNPs shall be estimated from a ratio of the scattering peak area (intensity) A at $2\theta = 26.4^\circ$. Utilizing the dotted black curve in Fig. 4.1.2c as a baseline, the ratio, $A(\text{EF})/A(\text{no EF})$ was evaluated as approximately 5. If the GNP stacks had an ideal, random orientation before application of the electric field, one third of those stacks should have been oriented in the direction of the X-ray beam, and two thirds, in the other two directions. Full electric field-induced orientation from this random orientation would give $A(\text{EF})/A(\text{no EF}) = 3$, but the observed $A(\text{EF})/A(\text{no EF})$ ratio ($\cong 5$) is larger than this ratio for the ideal case. This fact suggests that the GNP stacks before application of the electric field were rather preferentially oriented in a direction parallel to the sample surface (in the direction normal to the electric field) because of the

mechanical compression during the sample preparation, and that those stacks were mostly oriented by the electric field. (As a rough estimate, it is noted that $A(\text{EF})/A(\text{no EF}) = 5$ if four fifth (instead of two thirds) of the GNP stacks were oriented parallel to the sample surface before application of the electric field and all stacks were oriented along the field when it was applied). This electric field-induced orientation is uniaxial and would result in no anisotropy in a plane normal to the electric field, which is consistent with the circular symmetry seen for the 2D WAXD profile after application of the electric field (Fig. 4.1.2b).

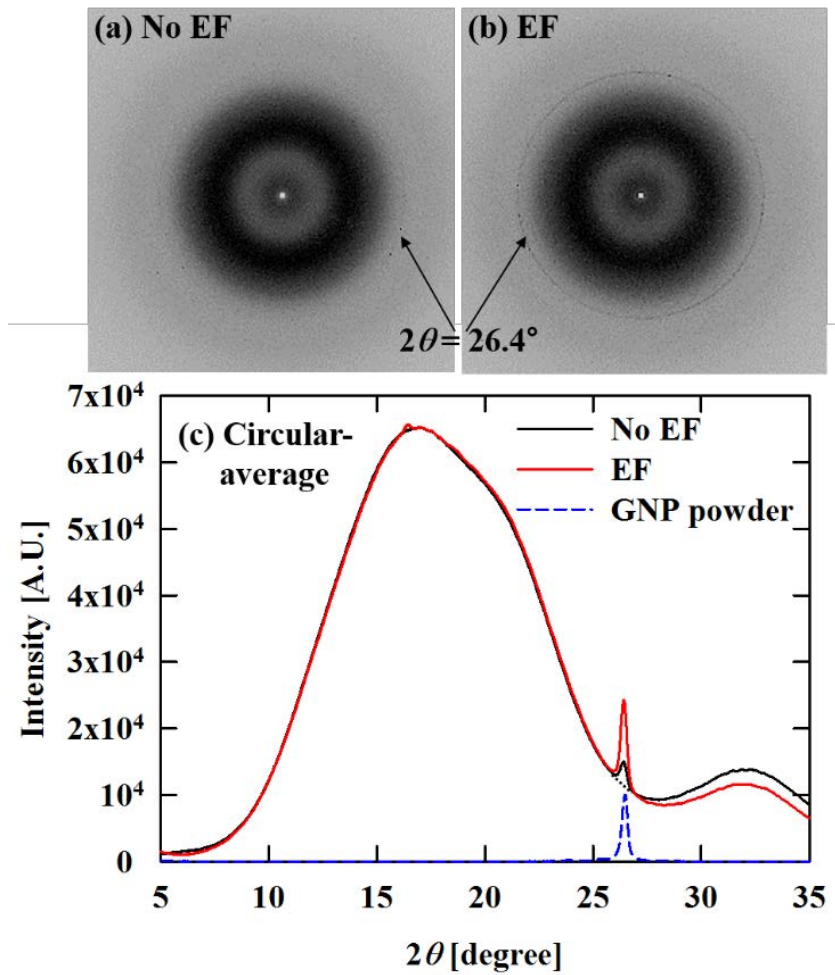


Fig. 4.1.2 2D wide-angle X-ray diffraction (2D WAXD) profiles of GNP composite with $\phi_{\text{GNP}} = 0.28$ vol% (a) before (denoted as “No EF”) and (b) after (denoted as “EF”) application of the electric field (1.75 kV/mm, $f = 60$ Hz). The most outer ring (denoted as “ $2\theta = 26.4^\circ$ ”) indicates diffraction from the 002 plane of graphene sheets being oriented parallel to the incident X-ray beam, namely in the direction normal to the sample surface. The electric field, when applied, was in parallel to the incident beam direction. The circular-average 1D WAXD profiles obtained from the 2D profiles are shown in part c, together with the 1D profile of pure GNP powder (shown as a reference).

The results shown in Figs. 4.1.1 and 4.1.2 demonstrate that the GNP stacks were largely oriented in the electric field direction irrespective of their content ϕ_{GNP} . The local structure corresponding to this orientation can be examined with TEM. For the composite with $\phi_{\text{GNP}} = 0.28$ vol% (examined in Fig. 4.1.2), the results of TEM observation are presented in Fig. 4.1.3. It was not easy to specify the direction of the electric field within the TEM image (partly because the TEM specimens sliced from the composite had irregular shapes). However, comparison of TEM images before and after application of the electric field suggests that the local orientation of the GNP stacks detected in the length scale of TEM images is more or less random (roughly the same number of stacks are oriented in different directions) before application of the field, whereas the local orientation is rather coherent (a large fraction of the stacks are oriented in the same direction) after application of the field. The electric field in the latter case is expected to be in the direction of the orientation of the majority of the stacks, as judged from the WAXD data shown in Fig. 4.1.2. The arrows in Figs. 4.1.3c and 4.1.3d (denoted as “EF”) indicate this expected direction.

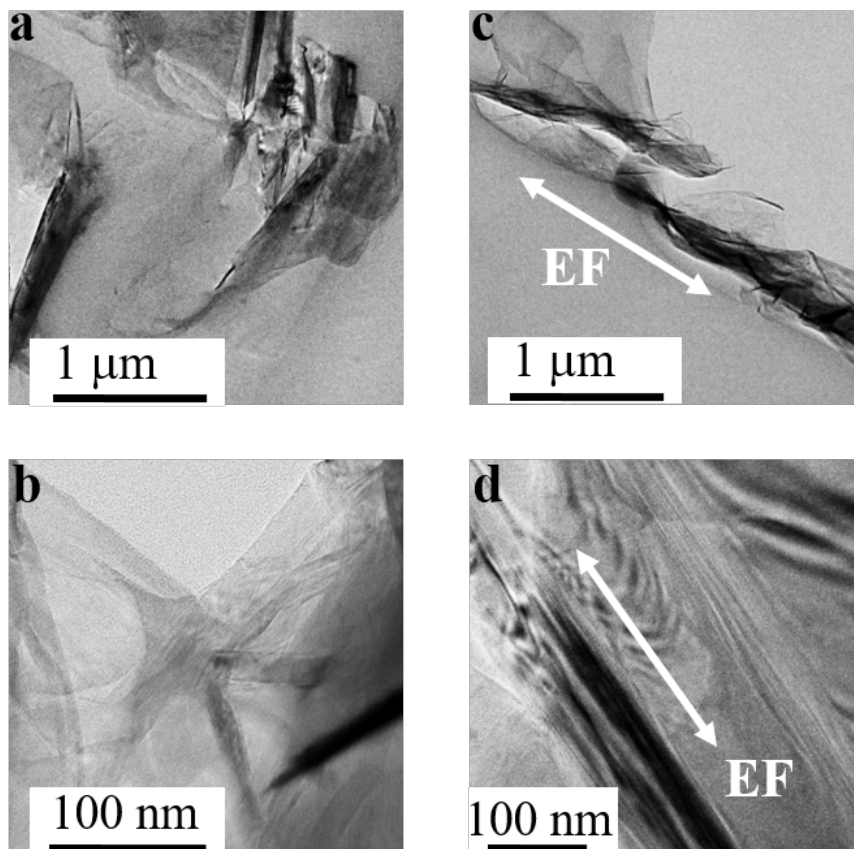


Fig. 4.1.3 Low and high magnification TEM images of GNP composite with $\phi_{\text{GNP}} = 0.28$ vol% before (a and b) and after (c and d) application of the electric field (1.75 kV/mm, $f = 60$ Hz). The direction of the applied electric field (EF), *expected* from the WAXD data, is indicated in c and d.

In summary, the structural data presented in Figs. 4.1.1-4.1.3 strongly suggest that the GNP stacks under the electric field were mostly oriented, irrespective of ϕ_{GNP} , in the field direction to form chained (or columnar) structure in that direction. For large ϕ_{GNP} (≥ 0.17 vol%), this chained-stack structure conductively bridged two electrodes, as evidenced from the short circuit occurring on application of the electric field for a sufficiently long time (14 min and 6 min for $\phi_{\text{GNP}} = 0.17$ and 0.28 vol%, respectively, as explained for Figs. 4.1.1 and 4.1.2). This chained-stack structure bridging the electrodes is the key structure in the discussion of rheological and electrical properties of the composites presented below.

4.1.2. Rheological properties

Figs. 4.1.4 and 4.1.5, respectively, show the data of storage and loss moduli, $G'(\omega)$ and $G''(\omega)$, measured at 190 °C for the GNP composites having $\phi_{\text{GNP}} = 0.06\text{-}0.34$ vol%. For comparison, the data are shown also for the neat PLA matrix. The PLA matrix has almost completely relaxed in the experimental window at 190 °C, as noted from the power-law dependence of its moduli on the angular frequency ω , $G'(\omega) \sim \omega^2$ and $G''(\omega) \sim \omega$. The loss modulus $G''(\omega)$ is proportional to ω at all ω below 10 rad/s, whereas the storage modulus $G'(\omega)$ is (approximately) proportional to ω^2 only at $\omega = 1\text{-}10$ rad/s and weakens its ω dependence at lower $\omega < 1$ rad/s. This weakening indicates that the PLA matrix has not fully relaxed even at the lowest ω examined (0.1 rad/s), because of its broad molecular weight distribution $M_w/M_n = 2.01$: A high- M tail component having a small fraction in this distribution does not seem to have relaxed even at $\omega = 0.1$ rad/s to weaken the ω dependence of $G'(\omega)$ but hardly contribute to $G''(\omega)$. Nevertheless, the neat PLA matrix essentially behave as a viscous fluid, as judged from the $G''(\omega)/G'(\omega)$ ratio (>1 at all ω).

Now, a focus is given on the behavior of the GNP composites. Before application of the strong AC electric field (Figs. 4.1.4a and 4.1.5a), $G'(\omega)$ and $G''(\omega)$ of the composites are very close to those of the neat PLA matrix. Thus, those composites behave essentially as viscous fluids indistinguishable from the neat matrix, quite possibly because GNP

stacks having $\phi_{\text{GNP}} \leq 0.34$ vol% were rather dilute and their almost random orientation in the PLA matrix provided the composites with no significant slow relaxation mechanism.

Application of the electric field hardly affected $G'(\omega)$ and $G''(\omega)$ of the composite with $\phi_{\text{GNP}} = 0.06$ vol%, suggesting that the chained-stack structure of the GNPs was formed by the field (as noted in Fig. 4.1.1) but did not fully extend from one plate (electrode) to the other. Such “non-bridging” structure, evidenced from lack of the electrical short circuit explained in the previous chapter, resulted in no intensive slow relaxation mechanism (because it is dilute), thereby allowing the composites to still behave as a fluid exhibiting the $G^*(\omega)$ data close to the data of the neat PLA matrix. In contrast, for $\phi_{\text{GNP}} \geq 0.17$ vol%, application of the electric field drastically increases $G'(\omega)$ at low ω thereby allowing the composites to exhibit the solid-like response, $G'(\omega) \sim \omega^0$ at low ω , as noted in Fig. 4.1.4b. For this case, the stacks of GNPs appear to be sufficiently concentrated thereby allowing the chained-stack structure to elastically bridge the two plates (which is in harmony with the electrical short circuit noted for the concentrated composite). For the composites with $\phi_{\text{GNP}} \geq 0.17$ vol%, the equilibrium modulus G_e characterizing the elastic GNP bridge therein is estimated as the $G'(\omega)$ value at the lowest ω ($= 0.1$ rad/s) examined. This G_e is analyzed later in Chapter 4.1.4.1.

In relation to the GNP bridge formation discussed above, it is also

important to note that application of the electric field hardly affected $G''(\omega)$ even for $\phi_{\text{GNP}} \geq 0.17$ vol% (cf. Fig. 4.1.5b). This fact confirms the elastic feature (no viscoelastic loss) of the chained-stack structure of the GNP bridge formed at those ϕ_{GNP} .

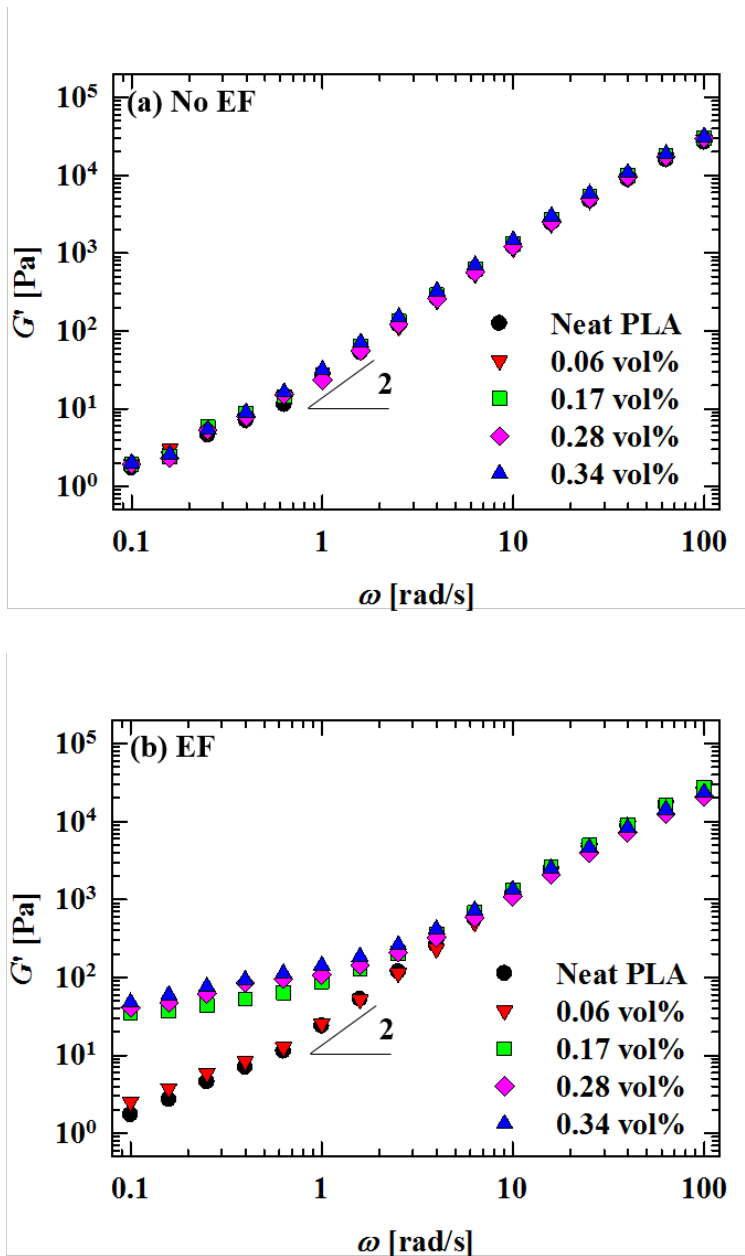


Fig. 4.1.4 Angular frequency (ω) dependence of storage modulus G' of GNP composites at 190 °C (a) before and (b) after application of the electric field (1.75 kV/mm, $f = 60$ Hz).

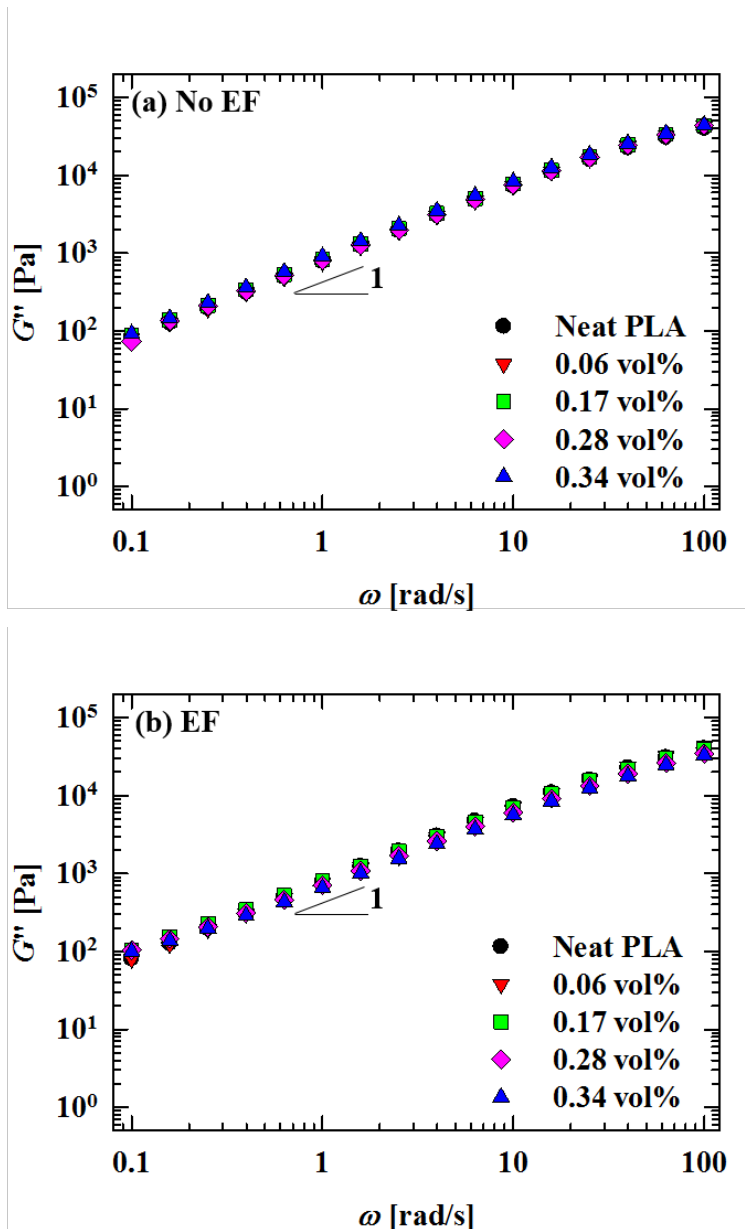


Fig. 4.1.5 Angular frequency (ω) dependence of loss modulus G'' of GNP composites at 190 °C (a) before and (b) after application of the electric field (1.75 kV/mm, $f = 60$ Hz).

The storage modulus of the composites at the lowest ω examined, $G'(\omega = 0.1)$ evaluated from the data in Fig. 4.1.4, is summarized in Fig. 4.1.6 as a function of ϕ_{GNP} . Before application of the electric field, $G'(\omega = 0.1)$ increases with ϕ_{GNP} only slightly because no intensive slow relaxation is activated by dilute and randomly oriented stacks of GNPs, as already explained for Fig. 4.1.4. In contrast, after application of the field, a drastic increase of $G'(\omega = 0.1)$ by a factor of 16 is noted on an increase of ϕ_{GNP} from 0.06 vol% to 0.17 vol %. This increase, corresponding to the liquid-to-solid transition explained for Fig. 4.1.4, reflects formation of the chained-stack structure elastically bridging the parallel plates in the rheometer. $G'(\omega = 0.1)$ after this transition, utilized as the equilibrium modulus G_e of the GNP bridge, increases just moderately with ϕ_{GNP} (≥ 0.17 vol%), as already noted in Fig. 4.1.4. This behavior of G_e is later discussed in Chapter 4.1.4 through comparison with the electrical conductivity.

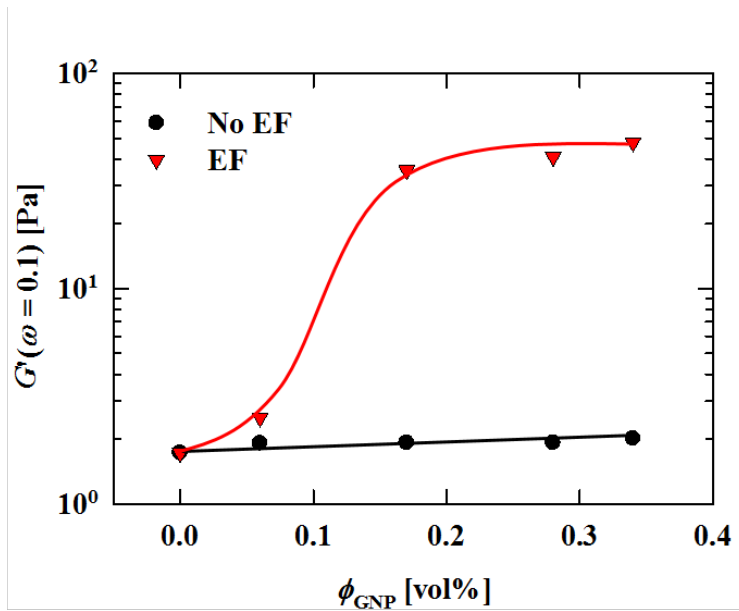


Fig. 4.1.6 ϕ_{GNP} dependence of $G'(\omega = 0.1)$ of GNP composites at 190 °C before and after application of electric field (1.75 kV/mm, $f = 60$ Hz). Lines were drawn to guide the eye.

4.1.3. Electrical properties

Fig. 4.1.7 shows the data of dynamic dielectric constant and dielectric loss, $\varepsilon'(\omega)$ and $\varepsilon''(\omega)$, measured at 190 °C for the GNP composites having $\phi_{\text{GNP}} \leq 0.34$ vol%. The dielectric measurement was conducted in the rheometer (utilizing the parallel plate electrodes) for freshly loaded composite samples that were subjected to the strong AC electric field in the same way as in the viscoelastic measurements explained for Figs. 4.1.4 and 4.1.5.

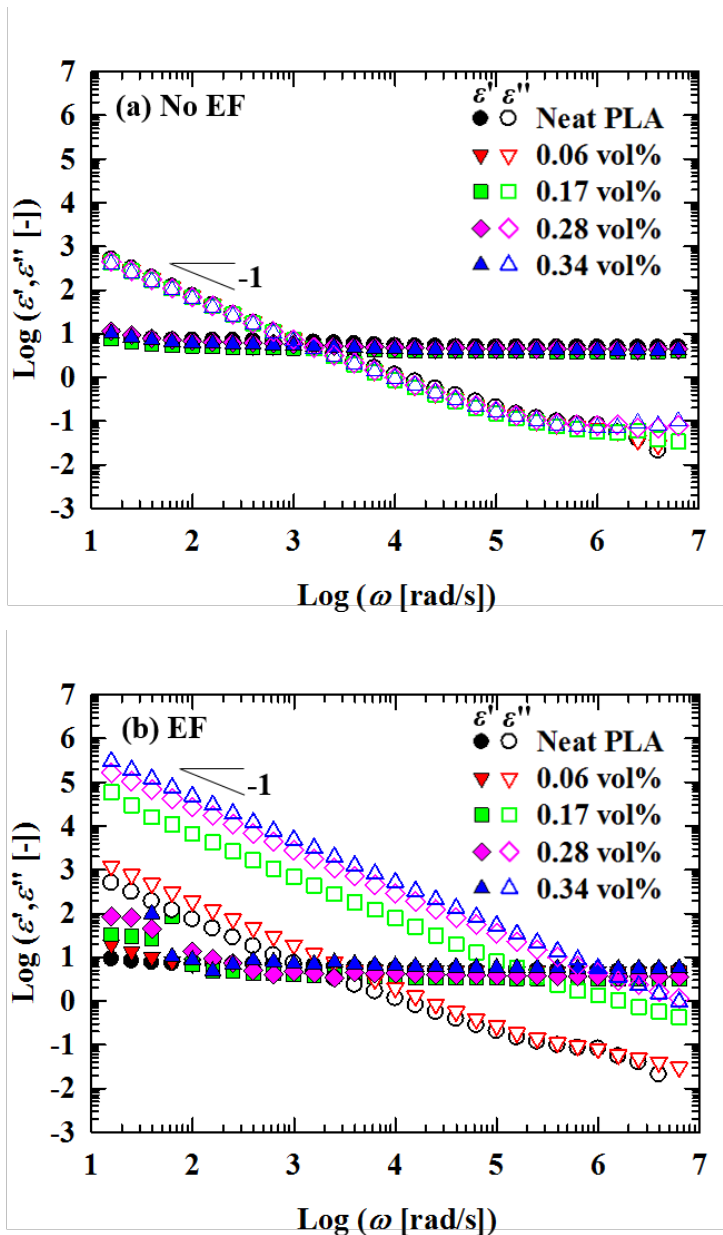


Fig. 4.1.7 Angular frequency (ω) dependence of dynamic dielectric constant ϵ' (filled symbols) and dielectric loss ϵ'' (unfilled symbols) of GNP composites at 190 °C (a) before and (b) after application of the electric field (1.75 kV/mm, $f = 60$ Hz).

Before application of the strong electric field (Fig. 4.1.7a), the $\varepsilon'(\omega)$ and $\varepsilon''(\omega)$ data of the composites are very close to those of the neat PLA matrix, suggesting that the GNP stacks were well dispersed to form no electrically percolated path and the dielectric response of the composite as a whole is hardly affected by such dilute stacks (having $\phi_{\text{GNP}} \leq 0.34$ vol%). For all systems, $\varepsilon''(\omega)$ at low ω is proportional to ω^{-1} to exhibit the dc conductance. Because of the coincidence of the $\varepsilon''(\omega)$ data of the composites and neat PLA, this conductance is attributed to the motion of ionic impurities included in PLA.

Application of the strong electric field hardly affected $\varepsilon'(\omega)$ and $\varepsilon''(\omega)$ of the composite having $\phi_{\text{GNP}} = 0.06$ vol%. This result suggests that the chained-stack structure of GNPs was formed by the strong electric field but this structure was not long/large enough to bridge the two electrodes. This “non-bridging” structure was concluded also from the liquid-like rheological response of the dilute composite being unaffected by application of the electric field (Figs. 4.1.4-4.1.6). That structure is dilute ($\phi_{\text{GNP}} = 0.06$ vol%) and thus cannot significantly affect the dielectric response of the composite as a whole.

In contrast, for $\phi_{\text{GNP}} \geq 0.17$ vol%, application of the strong AC electric field drastically increases $\varepsilon''(\omega)$ by two orders of magnitude, as noted in Fig. 4.1.7b. In those concentrated blends, the chained-stack structure of GNPs bridging the two electrodes should have been formed by the strong electric field, as discussed in relation to the solid-like

rheological response of the concentrated composites. Such a “bridging structure” provides the composite with the dc conduction (due to the electron flow between the electrodes), thereby enlarging $\varepsilon'(\omega)$ but hardly affecting the dynamic dielectric constant $\varepsilon'(\omega)$ that represents storage of the electrostatic energy, as observed in Fig. 4.1.7b.

This enhancement of the electrical dissipation observed for the concentrated GNP composites on application of the strong electric field can be also expressed as a decrease of a “phenomenological” relaxation time τ_{dc} defined for the dielectric modulus, $M^* = 1/\varepsilon^*$ (eq 3.5.1). Specifically, for a material having a ω -independent ε' (= static dielectric constant ε_s) and purely dissipative ε'' (= $\omega^{-1}\{\sigma_{dc}/\varepsilon_0\}$) with σ_{dc} and ε_0 being the static (dc) conductivity and the absolute permittivity of vacuum, respectively, M^* is expressed in the single Maxwellian form [57]:

$$M^*(\omega) = \frac{1}{\varepsilon_s} \frac{\omega^2 \tau_{dc}^2}{1 + \omega^2 \tau_{dc}^2} + j \frac{1}{\varepsilon_s} \frac{\omega \tau_{dc}}{1 + \omega^2 \tau_{dc}^2} \quad (j = \sqrt{-1}) \quad (4.1.1a)$$

with

$$\tau_{dc} = \frac{\varepsilon_0 \varepsilon_s}{\sigma_{dc}} \quad (4.1.1b)$$

ε^* data of the composites were converted into the dielectric modulus M^* and the ω dependence of M^* was examined. The results are summarized in Fig. 4.1.8 for the imaginary part, M'' . Almost single Maxwellian peak is observed for all composites and neat PLA at low ω , because all these

materials had ω -insensitive ε' and dissipative ε'' at low ω (cf. Fig. 4.1.7). Application of the strong electric field significantly shifts this peak to higher ω for the concentrated composites ($\phi_{\text{GNP}} \geq 0.17$ vol%) but not for the dilute composite ($\phi_{\text{GNP}} = 0.06$ vol%), as noted from comparison of Figs. 4.1.8a and 4.1.8b. Phenomenologically, this peak shift results from a very strong increase of σ_{dc} associated with no significant change of ε_s occurring on application of the strong electric field: The peak frequency, $1/\tau_{\text{dc}}$, strongly increases for that case; cf. eq 4.1.1b. (Consequently, no significant shift of the peak is observed for the dilute composite exhibiting just a mild increase of σ_{dc} on the electric field application.) From the structural point of view, the strong increase of σ_{dc} without significant change of ε_s is attributed to formation of the chained-stack of GNP conductively bridging the electrodes.

In Fig. 4.1.9, the peak shift seen in Fig. 4.1.8 is quantified as a decrease of the phenomenological τ_{dc} (reciprocal of peak frequency). It should be again emphasized that τ_{dc} is determined by the balance of dissipation and storage of the electrostatic energy, that is, a balance of σ_{dc} and ε_s (cf. eq 4.1.1b). For the composites examined, the strong decrease of τ_{dc} merely reflects the enhanced electrical conduction (dissipation) due to the GNPs bridging the electrodes, and is not related to any molecular relaxation (dipolar relaxation) process.

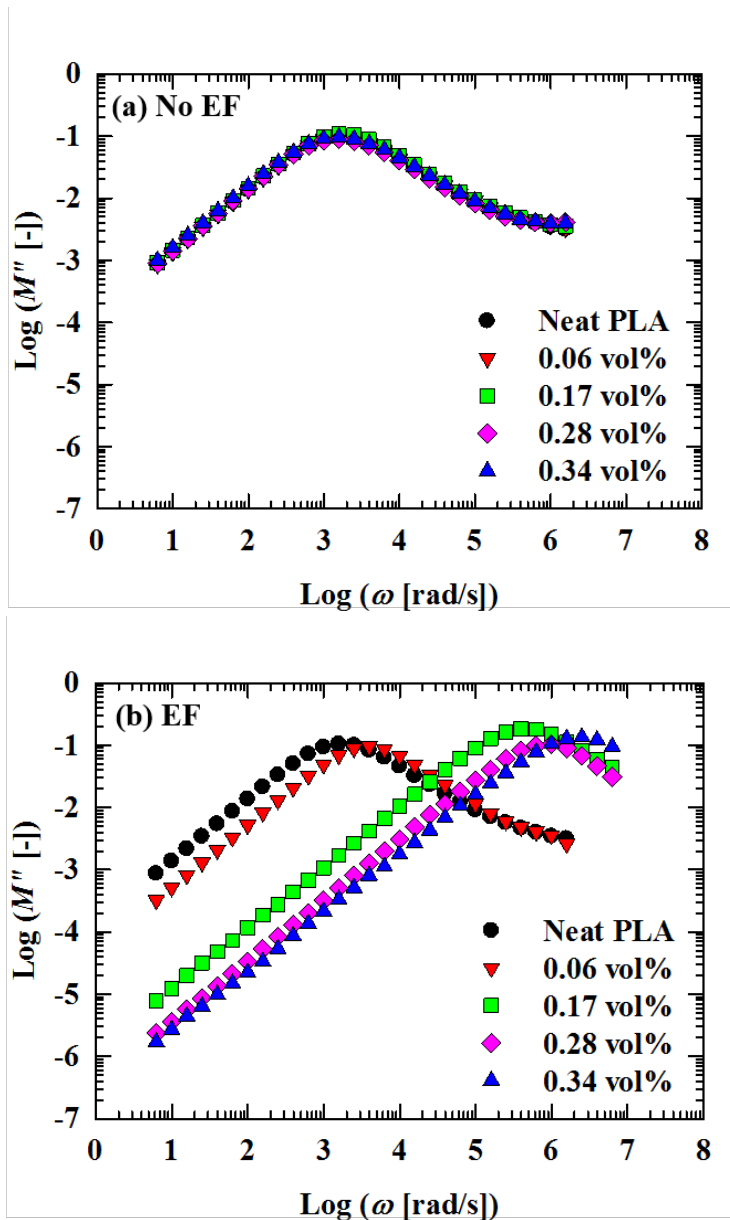


Fig. 4.1.8 Angular frequency (ω) dependence of the imaginary part of dielectric modulus M'' of GNP composites at 190 °C (a) before and (b) after application of the electric field (1.75 kV/mm, $f = 60$ Hz).

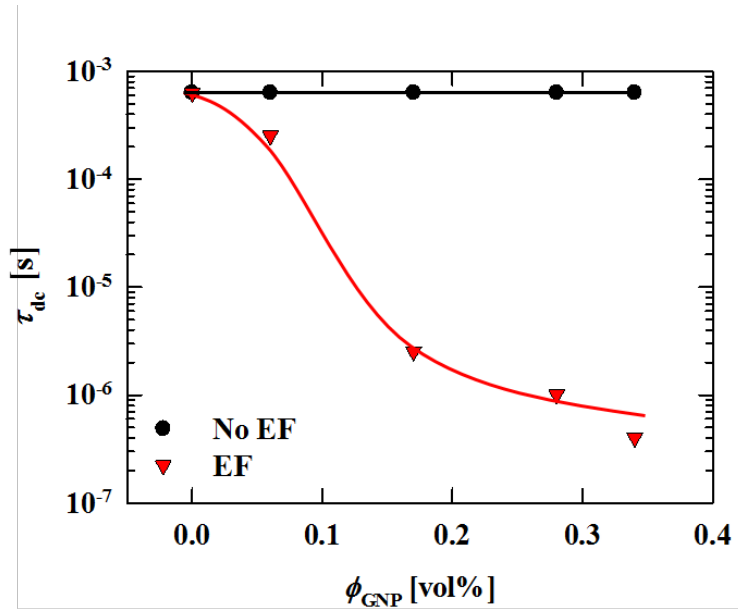


Fig. 4.1.9 ϕ_{GNP} dependence of phenomenological relaxation time, τ_{dc} before and after application of the electric field (1.75 kV/mm, $f = 60$ Hz). Lines were drawn to guide the eye.

In Fig. 4.1.10, the static (dc) conductivity σ_{dc} is compared for the GNP composites before and after application of the strong electric field. The strong increase of σ_{dc} on this application observed for the composites with $\phi_{GNP} \geq 0.17$ vol% is equivalent to the strong decrease of τ_{dc} seen in Fig. 4.1.9, so that Fig. 4.1.10 adds no new information in this sense. However, comparing Figs. 4.1.6 and 4.1.10, it is noted that the equilibrium modulus of the composites with $\phi_{GNP} \geq 0.17$ vol% after application of the electric field increases just weakly with ϕ_{GNP} whereas the increase of their dc conductivity is much more prominent. This difference between the equilibrium modulus and dc conductivity suggests that the GNPs exhibit a secondary structural change(s) on application of the strong electric field in addition to the primary structural change, formation of the chained-stack structure bridging the electrodes for the case of $\phi_{GNP} \geq 0.17$ vol%. This secondary change is later discussed in Chapter 4.1.4.1 in relation to the primary, chained-stack structure.

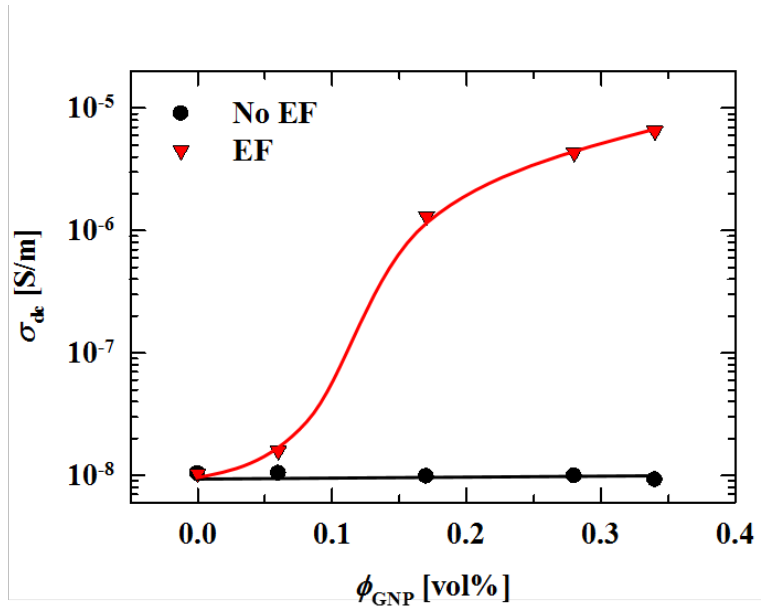


Fig. 4.1.10 ϕ_{GNP} dependence of σ_{dc} of GNP composites at 190 °C before and after application of the electric field (1.75 kV/mm, $f = 60$ Hz). Lines were drawn to guide the eye.

4.1.4. Correlation between structure and properties

4.1.4.1. primary structure

To obtain a better insight of the chained-stack structure, it is desired to correlate the structure with the properties of the GNP composite through quantitative analysis. In the simplest case, a single chained-stack extending from one electrode to the other may be regarded as a rigid single slab, as illustrated in Fig. 4.1.11a.

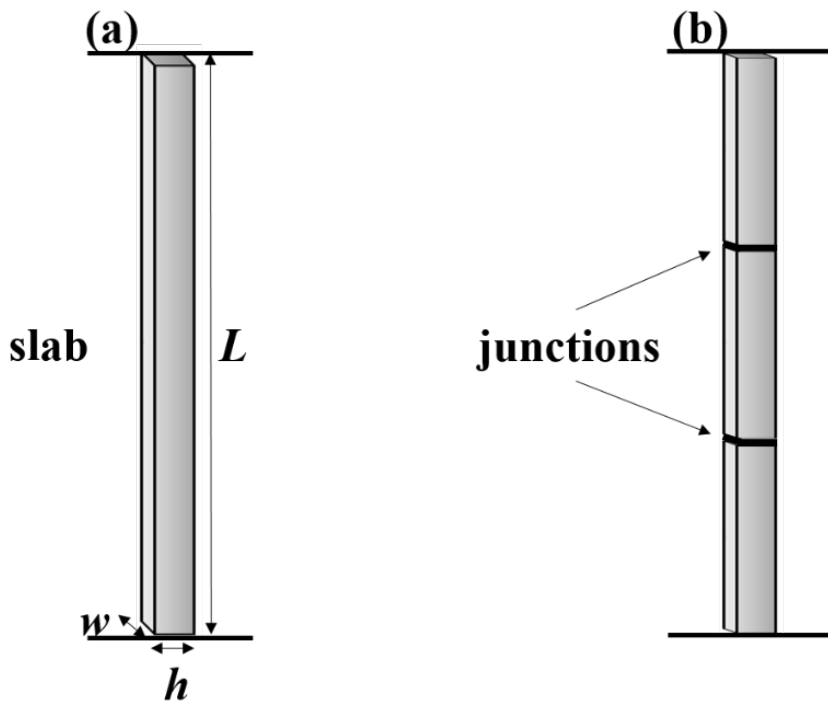


Fig. 4.1.11 Schematics of a chained-stack structure (a) as a rigid single slab and (b) with junctions.

If those rigid slabs tightly bridge the parallel plates in the rheometer, it should have been bent during the linear viscoelastic measurements, thereby exerting an elastic stress to the plates and sustaining the equilibrium modulus G_e . (For the composites with $\phi_{\text{GNP}} \geq 0.17$ vol%, G_e was estimated as the storage modulus at the lowest ω examined, $G'(\omega = 0.1)$, as already explained in Chapter 4.1.2.) This G_e can be roughly estimated from a force F per unit area (1×1) of the plate (*i.e.*, shear stress) required to bend all bridging slabs. Specifically, F can be expressed in a form of “beam bending” force [58]:

$$F \cong \nu_{\text{slab}} E \frac{4wh^3d}{L^3} \quad (4.1.2)$$

Here, ν_{slab} is the number of slabs bridging the unit area of the plates, E is the Young’s modulus of the slab, L is the slab length identical to the gap between the parallel plates, h and w indicate is the thickness and width of the slab, and d denotes the deflection of the slab that creates the stress F . This F should be identical to the elastic shear stress, γG_e , where the shear strain γ is equivalent to d/L . Substituting this expression of the force, $F = G_e d/L$, into eq 4.1.2 and considering that the factor $whL\nu_{\text{slab}}$ appearing in eq 4.1.2 is a volume of the slabs per unit area of the plate (per volume of $1 \times 1 \times L$ of the material) and can be replaced by the GNP volume in this volume, $\phi_{\text{GNP}}L$, an expression of G_e can be found as

$$G_e \cong E \frac{4h^2}{L^2} \phi_{\text{GNP}} \quad (4.1.3)$$

The Young's modulus of graphene sheet is known to be $E \cong 1$ TPa [45]. The other parameters appearing in eq 4.1.3 were determined and/or estimated from this experiment: $\phi_{\text{GNP}} = 0.34$ vol%, $L = 0.45$ mm (gap between the parallel plates), and $h = 100$ nm as estimated from the optical microscope image shown in Fig. 4.1.1 (after magnification of the image). Utilizing the E value and those parameter values in eq 4.1.3, G_e was calculated as 670 Pa. This G_e value is just a crude estimate, because of a considerable uncertainty in the estimate of h . Nevertheless, the equilibrium modulus measured for the concentrated composite after application of the electric field, $G_e = G'(\omega = 0.1) \cong 46$ Pa for $\phi_{\text{GNP}} = 0.34$ vol% (Fig. 4.1.6), is an order of magnitude smaller than the calculated G_e . Thus, the actual chained-stack structure of GNPs should be significantly different from the rigid single slab structure assumed in the calculation. The actual structure could have included many defects working as soft junctions as illustrated in Fig. 4.1.11b, thereby having G_e much smaller than the calculation.

This argument is in harmony with the observation that the composite with $\phi_{\text{GNP}} = 0.34$ vol% after application of the electric field has the dc conductance of $\sigma_{\text{dc}} \cong 10^{-5}$ S/m (Fig. 4.1.10). If GNPs of this volume fraction were to tightly bridge the plates as considered in Fig. 4.1.11a, the conductance of the composite should have been $\sigma_{\text{dc}} = \phi_{\text{GNP}} \sigma_{\text{GNP}} \cong 3$

$\times 10^5$ S/m as judged from the bulk conductance of GNP, $\sigma_{\text{GNP}} \cong 10^8$ S/m [47, 48]. The observed σ_{dc} is far below this expectation, suggesting that the actual chained-stack structure of GNPs includes many junctions (defects) that are much less conductive compared to the body of GNP (each graphene nanoplate). This argument is in harmony with the above argument for G_e .

4.1.4.2. secondary structure

If *all* GNPs in the composites were organized into the chained-stack structure containing soft and less conductive junctions as illustrated in Fig. 4.1.11b, the equilibrium modulus G_e and static electrical conductance σ_{dc} would be smaller than the calculation for the rigid slab (Fig. 4.1.11(a)) but should still increase in proportion to ϕ_{GNP} . However, neither the G_e data nor σ_{dc} data exhibit this proportionality after application of the strong AC electric field: On the factor of 2 increase of ϕ_{GNP} from 0.17 to 0.34 vol%, G_e ($= G'(\omega = 0.1)$) increased only by a factor of $\cong 30\%$ (Fig. 4.1.6) whereas σ_{dc} increases by a factor of $\cong 500\%$ (Fig. 4.1.10). This difference in the ϕ_{GNP} dependence of G_e and σ_{dc} after application of the electric field is not simply expected from formation of the chained-stack of GNP connecting the electrodes (primary structure), thereby suggesting that an additional (secondary) structure was also formed in the composites to have different contributions to G_e and σ_{dc} .

The weak ϕ_{GNP} dependence observed for G_e (weaker than the proportionality) suggests that a considerable fraction of GNP stacks was not organized into the chained-stack columnar structure and remained elastically inert. Such elastically inert stacks could have remained because of the short circuit during application of the strong electric field. Once the short circuit happened, the electrical current should mostly flow through the chained-stack columns already organized at that point, and

the electric torque orienting the “left-over” GNP stacks (out this structure) would almost vanish.

Nevertheless, the strong ϕ_{GNP} dependence of σ_{dc} (stronger than the proportionality) suggests that those left-over GNP stacks still enhance the electrical conduction of the chained-stack columnar structure. As one possibility, it may be speculated that the elastically inert left-over stacks were still oriented locally in the electric field direction (though not connected with each other in that direction) and *softly* touch the neighboring chained-stack columns bridging the electrodes to offer an extra conductive path to these columns, as illustrated in Fig. 4.1.12a. A magnetic field generated by the oscillatory current flowing through the columns *might* help this type of local orientation, as judged from the behavior of electromagnetic fluids containing nano-carbons: For anisotropic nano-carbons including carbon nanotube and graphene [28-33], a magnetic field induces alignment parallel to the field. In the composites examined in this study, the large oscillatory current flowing through the chained-stack columns (on the short circuit) could have created a magnetic field normal to the current direction, and this magnetic field could help the left-over stacks to be oriented in the magnetic field direction. Those stacks have a disk-like shape, and their orientation is specified by directions of two axes parallel to the disk surface. The orientation of one axis in the magnetic field direction is

equivalent to the orientation of the other axis in the current direction (cf. Fig. 4.1.12a), that is, the direction of the orientation of the chained-stack columns.

This local orientation of the left-over stacks is consistent with the significantly enhanced diffraction from the 002 planes of GNP sheets observed for concentrated composite after application of the electric field (Fig. 4.1.2). In addition, the mechanical rigidity of the chained-stack columns would not be significantly enhanced and G_e would remain rather insensitive to ϕ_{GNP} if the left-over stacks just softly touch the columns.

Attempting to observe the secondary structure speculated above, a survey was made for all TEM images obtained in this study. In some of those images after magnification, a GNP stack inserted between (and apparently touching) two GNP stacks was found, as shown in an example presented in Fig. 4.1.12b. This structure could be a part of the secondary structure speculated in Fig. 4.1.12a, although it is not easy to specify the direction of the field in the TEM image for the reason explained for Fig. 4.1.3. Furthermore, the TEM images only cover small areas in the sample and cannot well resolve the connection (if any) between GNP stacks over a large length scale in a given direction. Further experiments are necessary for quantitative analysis of the secondary structure.

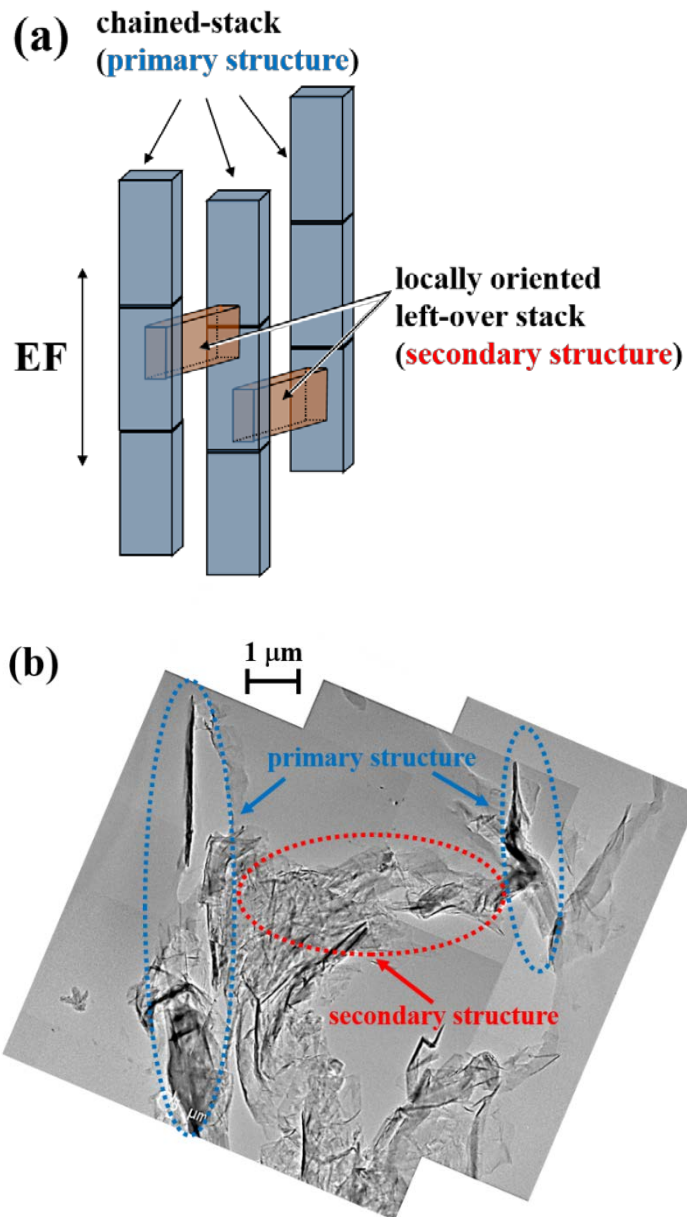


Fig. 4.1.12 (a) Schematic illustration of chained-stacks (primary structure) and left-over stacks (secondary structure) in the composite. (b) TEM image of GNP composite with $\phi_{\text{GNP}} = 0.28$ vol% after application of the electric field (1.75 kV/mm, $f = 60$ Hz).

4.2. Time/intensity-dependent changes by electric field

For the melt-mixed composite of PLA with GNPs having a fixed, low volume fraction $\phi_{\text{GNP}} = 0.34$ vol%, this chapter investigated growths of mechanical and electrical properties under an AC electric field of various intensities E for various times t_E , with a particular focus being placed on the field-induced GNP structures governing those properties. Details of the results are presented in this chapter.

4.2.1. Structure evolution under an electric field and evaluation of percolation time t_E^*

Fig. 4.2.1 presents optical micrographs (OM) obtained for a composite with $\phi_{\text{GNP}} = 0.028$ vol% being subjected to the strong electric field (2.5 kV/mm, $f = 60$ Hz) at 190 °C for times $t_E = 0$ s, 19 s, and 50 min. No further structural change was observed on application of the electric field for a longer t_E (> 50 min).

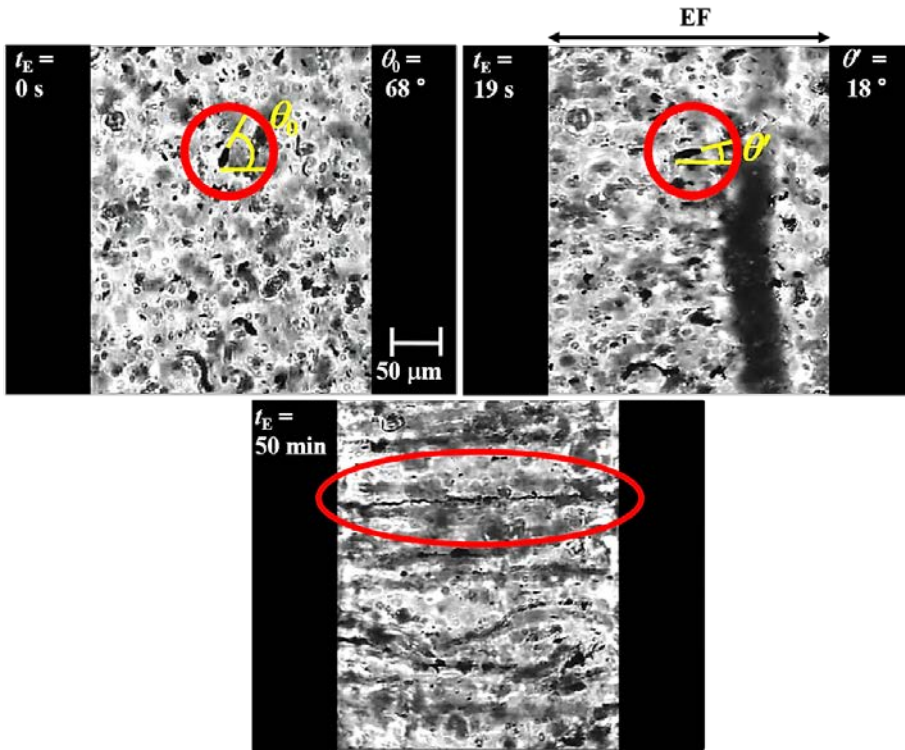


Fig. 4.2.1 Optical micrographs of GNP composite with $\phi_{\text{GNP}} = 0.028$ vol% subjected to the electric field ($E = 2.5$ kV/mm, $f = 60$ Hz) at 190 °C for times t_E as indicated. Circles and ellipse highlight characteristic structures of GNP stacks for respective t_E . The direction of the applied electric field (EF) is indicated in the image for $t_E = 19$ s. For the highlighted stack in the circles, the initial orientation angle (at $t_E = 0$) defined with respect to this field direction was $\theta_0 \cong 68^\circ$, and the angle at $t_E = 19$ s was $\theta' \cong 18^\circ$.

Before application of the electric field ($t_E = 0$ s), GNPs appeared to be organized into thin stacks but formed no large agglomerates. Those stacks were dispersed randomly in the PLA matrix through the mechanical melt mixing in the composite preparation process. In contrast, after application of the strong electric field, a fraction of the thin stacks of GNPs firstly rotated to align in the direction of the electric field ($t_E = 19$ s) and further organized into chains of stacks oriented in that direction (within $t_E = 50$ min), as highlighted by the circles and ellipse. (This column formation was optically confirmed also for concentrated composite with $\phi_{\text{GNP}} = 0.17$ vol% in Fig. 4.1.1.) Specifically, the stack highlighted with the circles has the initial orientation angle defined with respect to the electric field direction, $\theta_0 \cong 68^\circ$ at $t_E = 0$ s, and this angle decreases to $\theta' \cong 18^\circ$ at $t_E = 19$ s.

The structural evolution seen above should have occurred because of the electric field-induced dipole of each graphene sheet, as discussed in Chapter 4.1.1: The electron cloud of the sheet should instantaneously respond to the strong AC field to induce a dipole along the sheet that always has a positive component in the field direction, which results in efficient orientation of the GNP stacks in the field direction (unless the stack is initially oriented exactly normal to the field). These oriented stacks are further organized into a chain-like structure oriented in the field direction, quite possibly due to the interaction between the induced dipoles of neighboring stacks. The time scales of these structural changes,

including the time scale for the rotation mentioned above, are subjected to simple theoretical analyses later in Chapter 4.2.5.

For concentrated composites ($\phi_{\text{GNP}} \geq 0.17$ vol%), formation of the GNP columns *conductively bridging the electrodes* was noted as the electrical short circuit occurring on application of the strong electric field over certain times t_{E}^* . (The GNP columns were formed also in the extremely dilute composite with $\phi_{\text{GNP}} = 0.028$ vol% as noted in Fig. 4.2.1, but the columns were too short to bridge the electrodes and induced no short circuit.) For all concentrated composites examined, Table 4.2.1 summarizes the t_{E}^* values obtained from at least three independent runs of the strong electric field application. This t_{E}^* plays a key role in later analysis of the growth of the mechanical and electrical properties of the concentrated composite ($\phi_{\text{GNP}} = 0.34$ vol%) subjected to the strong electric field.

Here, it should be added that the short circuit of the concentrated GNP composite with $\phi_{\text{GNP}} = 0.34$ vol% was examined for several specimen of different thicknesses, 0.45, 0.9, and 1.35 mm (single-, double-, and triple-sheet samples). It turned out that t_{E}^* did not change with the sample thickness, given that the applied electric field had the same strength. This observation suggests that the rate-determining step for the GNP bridge formation (that resulted in the short circuit) is a rather *local* motion of the GNP stacks in the sample. This point is considered in the analysis explained later in Chapter 4.2.5.

Table. 4.2.1 The average time t_E^* required for formation of GNP columns conductively connecting two electrodes in concentrated GNP/PLA composites subjected to the strong AC electric field at 190 °C

ϕ_{GNP} (vol%)	t_E^* (min)	field intensity E (kV/mm)
0.17	31.5	1.10
	23.1	1.25
	19.8	1.50
	15.8	1.62
	12.6	1.75
	12.1	1.90
0.28	10.9	1.10
	8.6	1.25
	6.4	1.50
	6.2	1.62
	5.4	1.75
	5.2	1.90
0.34	7.2	1.10
	6.5	1.25
	5.4	1.50
	4.7	1.62
	4.5	1.75
	3.8	1.90

4.2.2. Rheological properties

For the GNP composite having $\phi_{\text{GNP}} = 0.34$ vol%, Fig. 4.2.2 shows the storage and loss moduli, $G'(\omega)$ and $G''(\omega)$, at 190 °C measured immediately after application of the strong electric field ($E = 1.75$ kV/mm) at 190 °C over the interval of time t_E as indicated. Before application of the field ($t_E = 0$ min), $G'(\omega)$ and $G''(\omega)$ of the composite were very close to those of the neat PLA matrix and *almost* proportional to ω^2 and ω , respectively, at intermediate-to-low angular frequencies ω . (At $\omega < 1$ s⁻¹, weak but slow relaxation is noted for the $G'(\omega)$ data of the neat PLA matrix having the polydispersity $M_w/M_n = 2.01$. This slow relaxation emerges also in the composite.) The coincidence of the moduli of the neat matrix and the as-prepared composite suggests that the GNP stacks with $\phi_{\text{GNP}} = 0.34$ vol% were still dilute and their random orientation therein activates no significant slow relaxation mechanism.

As noted in top panel of Fig. 4.2.2, $G'(\omega)$ of the composite is hardly affected by application of the strong electric field for $t_E = 1$ min but gradually increases in the low- ω regime ($\omega < 2$ rad/s) for $t_E = 2$ and 3 min, and finally becomes insensitive to t_E for $t_E \geq 4$ min. This growth of $G'(\omega)$ is attributable to formation of chained-stack structure (column) of GNP under the strong electric field. This structure is of elastic nature, as noted from the weak ω dependence (solid-like behavior) of $G'(\omega)$ in the low- ω regime in the saturated state ($t_E \geq 4$ min) and also from lack of significant increase observed for $G''(\omega)$ in the entire range of t_E .

It should be added that the $G'(\omega)$ and $G''(\omega)$ data shown in Fig. 4.2.2 remained the same at least for 30 min after switching off the strong electric field. This observation indicates that the Brownian motion of GNP stacks randomizing the column structure was much slower than the electric-field-driven GNP motion for formation of the columns (that completed within 4 min for the data shown in Fig. 4.2.2). This was the case for all electric field intensities examined ($E = 1.10 - 1.90$ kV/mm), allowing to consider that the Brownian force was much weaker than the force due to the electric field with those high intensities. This point becomes important in the analysis of the time scale of GNP column formation explained later. (In fact, this study focused only on the strong electric field with $E \geq 1.10$ kV/mm, thereby allowing to neglect the Brownian contribution to the GNP motion under that field.)

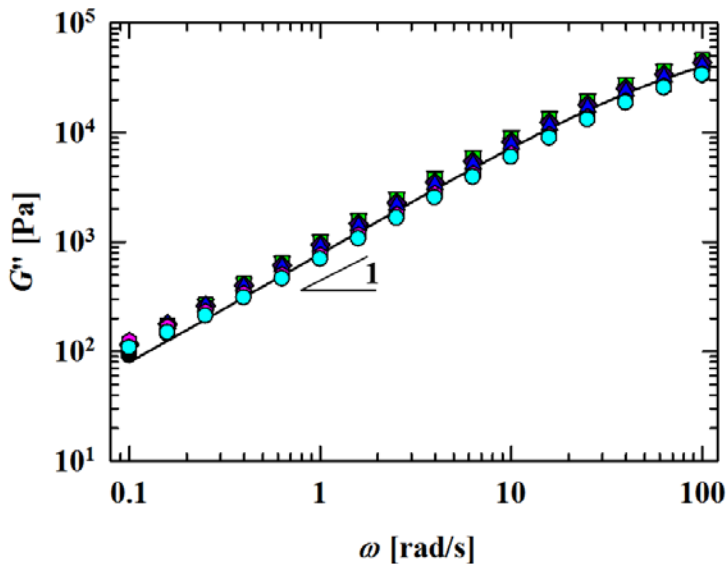
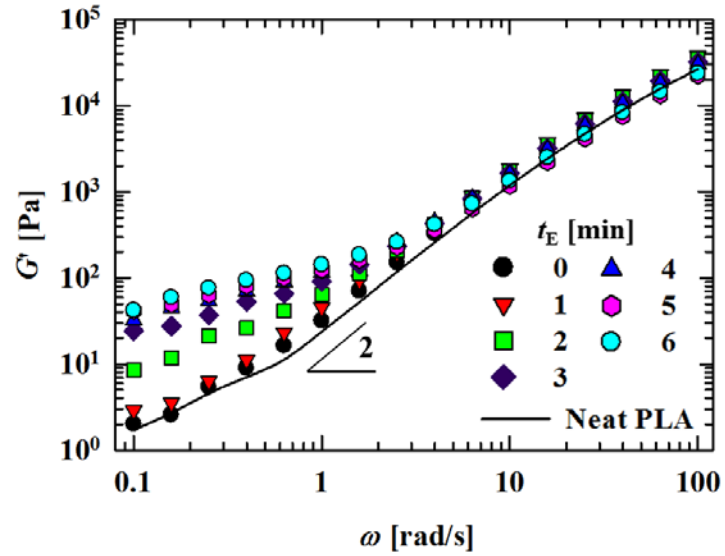


Fig. 4.2.2 Angular frequency (ω) dependence of storage and loss moduli, G' (top panel) and G'' (bottom panel), of GNP composite with $\phi_{\text{GNP}} = 0.34$ vol% at 190 °C measured after application of the strong electric field ($E = 1.75$ kV/mm, $f = 60$ Hz) for the time t_E as indicated. Neat PLA data are also shown as a reference.

It is of interest to examine the evolution of the elastic feature of the composite in relation to the time t_E^* (Table 4.2.1) for formation of long GNP columns *conductively* connecting the two electrodes (parallel plates used in the rheological measurements). For this purpose, the $G'(\omega = 0.1)$ data at the lowest ω in the experimental window ($\omega = 0.1$ rad/s) was utilized as a measure of the elasticity and its evolution were examined. The results are shown in Fig. 4.2.3 where the modulus increment due to the electric field, $\Delta G'(\omega = 0.1) \equiv G'(\omega = 0.1; t_E) - G'_{\text{ap}}(\omega = 0.1)$ with $G'_{\text{ap}}(\omega = 0.1)$ being the modulus of the as-prepared composite ($t_E = 0$ min), is plotted against t_E (top panel) and t_E/t_E^* (bottom panel).

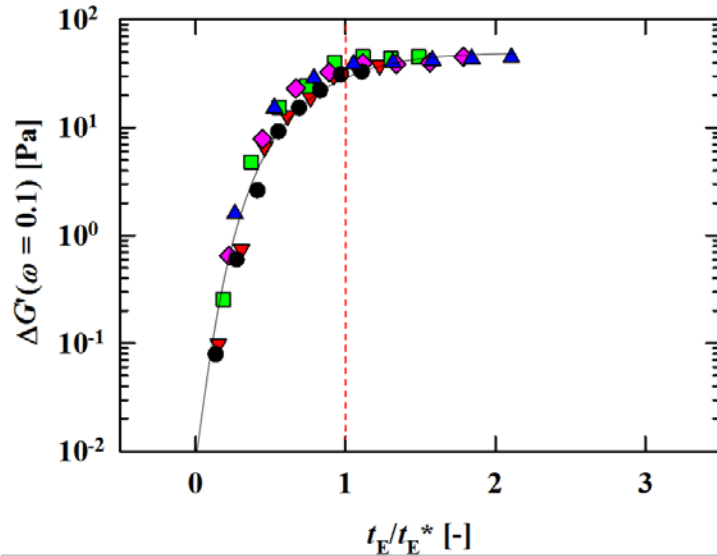
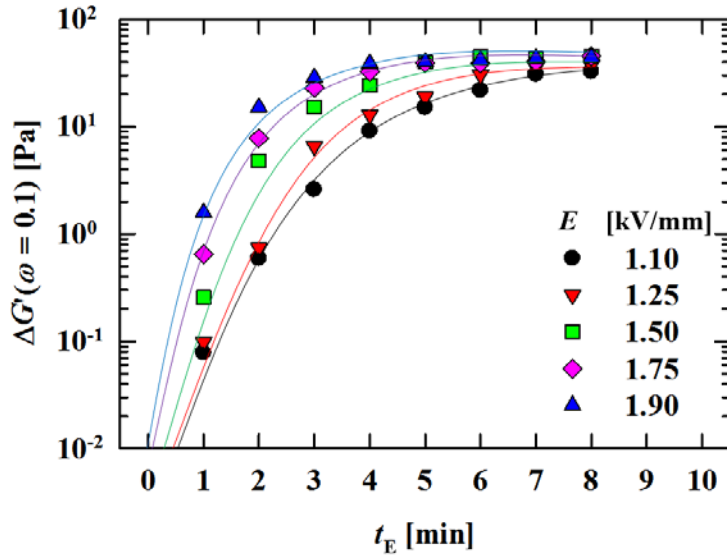


Fig. 4.2.3 Evolution of low- ω modulus increment $\Delta G'(\omega = 0.1)$ of composite with $\phi_{\text{GNP}} = 0.34$ vol% at 190 °C on application of the strong AC electric field of the intensity E as indicated. $\Delta G'(\omega = 0.1)$ is plotted against the electric field application time t_E (top panel) and a reduced time t_E/t_E^* (bottom panel). Lines were drawn to guide the eye.

Top panel of Fig. 4.2.3 demonstrates that the elasticity evolves faster on application of a stronger electric field, as naturally expected. This effect of the field intensity can be adsorbed in the time t_E^* for the GNP column formation (shorter for larger E ; cf. Table 4.2.1), thereby giving the master plots of $\Delta G'(\omega = 0.1)$ against the t_E/t_E^* ratio, the time t_E reduced with respect to the column formation time t_E^* , as noted in bottom panel. The $\Delta G'(\omega = 0.1)$ data points are excellently superposed to make this master plots, confirming that the elasticity grows in a way synchronous to formation of the GNP columns. However, it is also noted in bottom panel that the elasticity growth levels off by the reduced time $t_E/t_E^* = 1$, namely, on full formation of the GNP columns *conductively* connecting the electrodes. This result, suggesting some difference in the contributions of the columns to the mechanical elasticity and electrical conductivity, is discussed later in Chapter 4.2.4 in relation to the conductivity data.

4.2.3. Electrical properties

For the GNP composites having $\phi_{\text{GNP}} = 0.34$ vol%, Fig. 4.2.4 shows the dynamic dielectric constant and dielectric loss, $\epsilon'(\omega)$ and $\epsilon''(\omega)$, measured at 190 °C immediately after application of the strong electric field ($E = 1.75$ kV/mm) at the same temperature over the interval of time t_E as indicated. The measurement was made in the rheometer (utilizing the parallel plate electrodes) for freshly loaded composite samples that were subjected to the strong electric field in the same way as in the viscoelastic tests.

The $\epsilon'(\omega)$ and $\epsilon''(\omega)$ data are almost indistinguishable for the as-prepared composite ($t_E = 0$ min) and the neat PLA matrix, suggesting that the GNP stacks in the as-prepared composite (having small $\phi_{\text{GNP}} = 0.34$ vol%) were randomly oriented and well dispersed to form no electrically percolated path. The dielectric loss $\epsilon''(\omega)$ of the composite just moderately increases after application of the strong electric field for $t_E = 4$ min, whereas a drastic increase is observed on an increase of t_E from 4 min to 5 min. This drastic increase, accompanied by negligibly small changes in the dynamic dielectric constant $\epsilon'(\omega)$, reflects formation of GNP columns conductively connecting the electrodes (which was also detected as the short circuit under application of the strong field). It is also noted that $\epsilon''(\omega)$ increases gradually but $\epsilon'(\omega)$ hardly changes on a further increase of $t_E > 5$ min.

The $\epsilon'(\omega)$ and $\epsilon''(\omega)$ data shown in Fig. 4.2.4 remained the same at

least for 30 min after switching off the strong electric field, as similar to the behavior of the viscoelastic data explained for Fig. 4.2.2. Thus, the negligible contribution of the thermal Brownian force (compared to the force due to the strong electric field) to the GNP motion was confirmed also from the dielectric data.

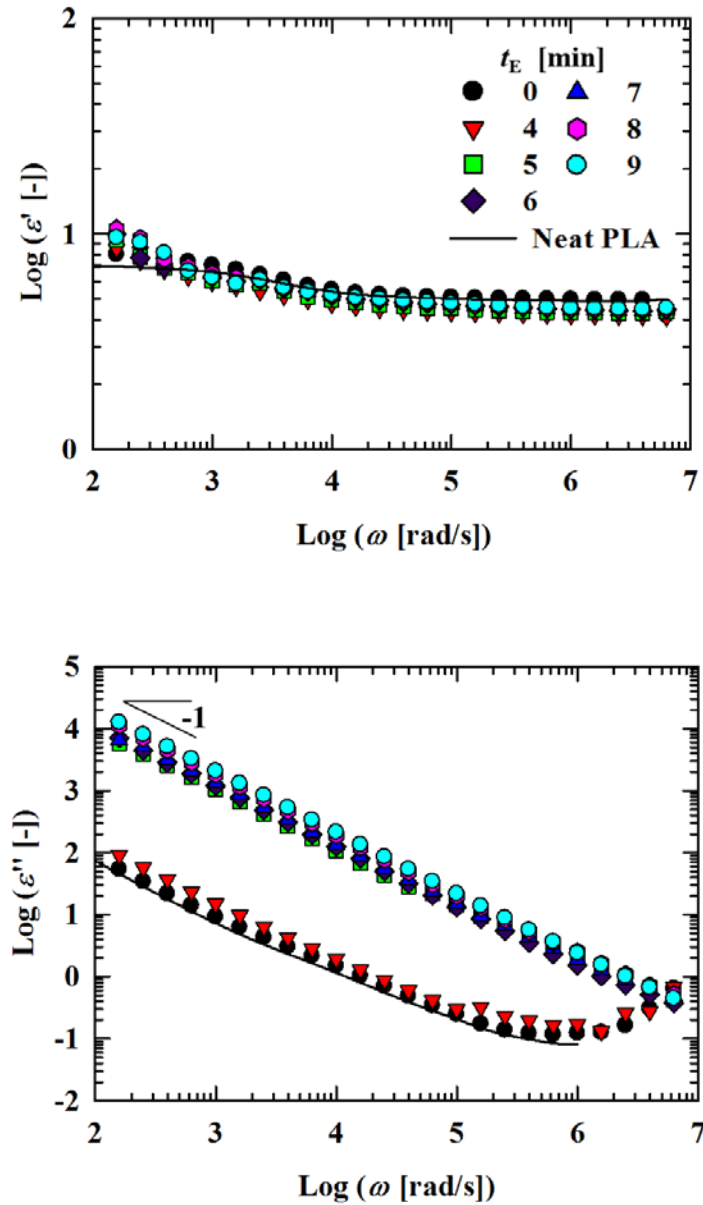


Fig. 4.2.4 Angular frequency (ω) dependence of dynamic dielectric constant and dielectric loss, ϵ' (top panel) and ϵ'' (bottom panel), of GNP composite with $\phi_{\text{GNP}} = 0.34 \text{ vol\%}$ at 190°C measured after application of the strong electric field ($E = 1.75 \text{ kV/mm}$, $f = 60 \text{ Hz}$) for the time t_E as indicated. Neat PLA data are also shown as a reference.

This change in the dielectric response can be characterized as a change of the dc conductivity σ_{dc} with t_E . For the composite after application of the strong electric field with various E for different t_E , the $\varepsilon''(\omega)$ data at low ω are proportional to ω^{-1} . Thus, the dc conductivity was evaluated as $\sigma_{dc} = \varepsilon_0[\omega\varepsilon''(\omega)]_{\omega \rightarrow 0}$ (with ε_0 being the absolute permittivity of vacuum). The conductivity observed for the neat PLA matrix (and as-prepared composite) is due to the ionic impurities included in the matrix. Therefore, the net increment of the conductivity due to application of the strong electric field was evaluated as $\Delta\sigma_{dc} \equiv \sigma_{dc}(t_E) - \sigma_{dc}(0)$ where $\sigma_{dc}(0)$ being the conductivity of the as-prepared composite ($t_E = 0$ min). In Fig. 4.2.5, this $\Delta\sigma_{dc}$ is plotted against t_E (top panel) and t_E/t_E^* (bottom panel).

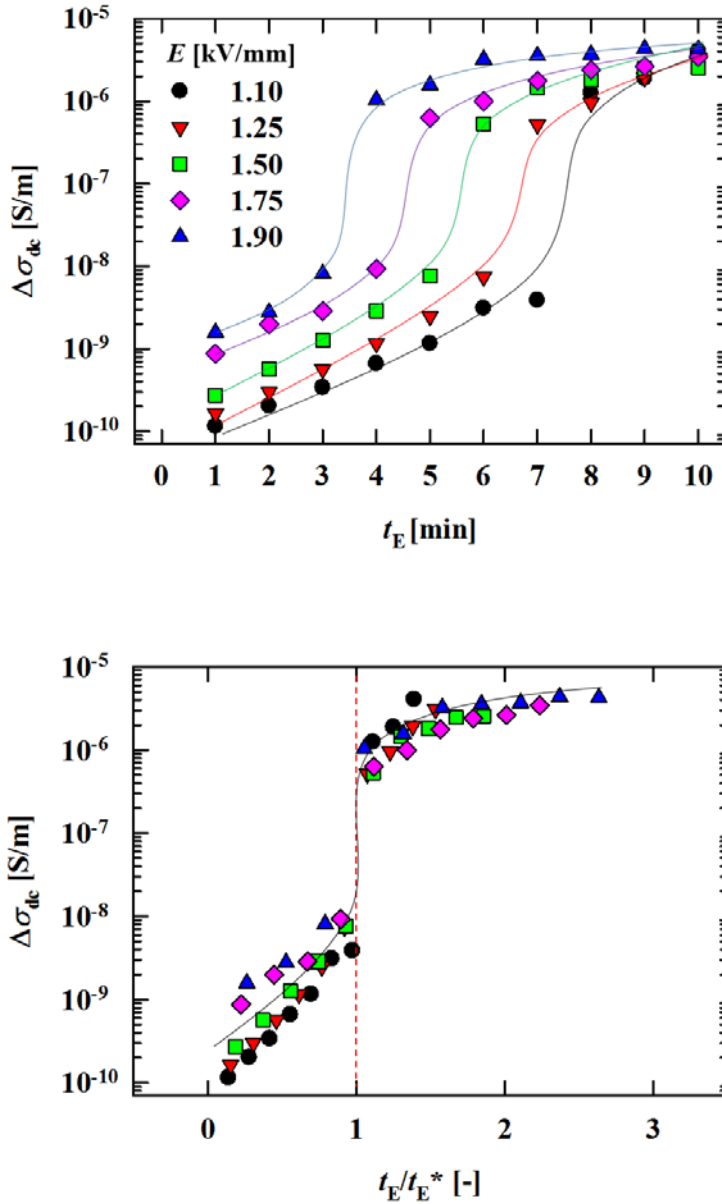


Fig. 4.2.5 Evolution of increment of dc conductivity $\Delta\sigma_{dc}$ of composite with $\phi_{GNP} = 0.34$ vol% at 190 °C on application of the strong AC electric field of the intensity E as indicated. $\Delta\sigma_{dc}$ is plotted against the electric field application time t_E (top panel) and a reduced time t_E/t_E^* (bottom panel). Lines were drawn to guide the eye.

Top panel of Fig. 4.2.5 demonstrates faster increase of the conductivity on application of a stronger electric field, as easily expected. (Phenomenologically, this increase can be also represented as a high- ω shift of the peak of the imaginary part of the dielectric modulus, $M'' \equiv \varepsilon''/\{\varepsilon'^2 + \varepsilon''^2\}$, as explained previously in Chapter 4.1.3.) The growth of the conductivity of the composite thus observed for various field intensity E can be summarized as master plots of $\Delta\sigma_{dc}$ against the reduced time t_E/t_E^* , as shown in bottom panel. Here, t_E^* is the time required for formation of GNP columns conductively connecting the two electrodes (Table 4.2.1). Good superposition of the data points in the master plots indicates that the conductivity increases in a way synchronous to formation of such columns, as was the case also for the growth of the mechanical elasticity (Fig. 4.2.3). In particular, a drastic (almost discontinuous) increase of $\Delta\sigma_{dc}$ occurs at $t_E/t_E^* = 1$, *i.e.*, when those columns were formed (to give electrical short circuit explained earlier). Nevertheless, $\Delta\sigma_{dc}$ keeps growing even at $t_E/t_E^* > 1$, suggesting that the GNP columns connecting the electrodes are not the only structure contributing to the conductivity. This point is further discussed in the next chapter in relation to the elasticity growth.

4.2.4. Similarity and difference of the elasticity and conductance growths

As noted from bottom panels of Figs. 4.2.3 and 4.2.5, the growths of the elasticity and conductivity of the composite with $\phi_{\text{GNP}} = 0.34$ vol% commonly behave as functions of the reduced time t_E/t_E^* . This result suggests that the elasticity and conductivity commonly grow in a way *primarily* synchronous to formation of the chained-stack columnar structure of GNPs that connect the parallel plate electrodes. Nevertheless, the elasticity increases most strongly at $t_E/t_E^* \cong 0.3$ and levels off by the reduced time $t_E/t_E^* = 1$, whereas the conductivity drastically increases at a longer time $t_E/t_E^* = 1$ (on the electrical short circuit) and keeps increasing gradually even at $t_E/t_E^* > 1$. This quantitative difference suggests some structural difference underlying the elasticity and conductivity growths.

Fig. 4.2.6 illustrates a hypothesis for the structural evolution that could lead to this difference of the elasticity and conductivity. Under the strong electric field, a fraction of the thin stacks of GNPs randomly dispersed in the as-prepared composites should firstly rotate and orient into the field direction because of the induced dipoles, as discussed earlier for the dilute composite (cf. Fig. 4.2.1). Essentially the same orientation would have occurred also in the concentrated composite ($\phi_{\text{GNP}} = 0.34$ vol%) examined in Figs. 4.2.2-4.2.5, although not directly observed for the reason explained earlier. This orientation would be

accompanied by conformational rearrangement of some matrix PLA chains, as illustrated in Fig. 4.2.6b. Good dispersion of GNPs in the as-prepared composite (Fig. 4.2.1) suggests that the GNP stacks were stabilized by PLA chains physically adsorbed thereon. These adsorbed chains can change their conformation to bridge neighboring stacks when these stacks rotate to come into a close neighborhood, thereby forming a soft, elastic network. This network, formed when the distance between the GNP stacks is smaller than the PLA chain size (radius of gyration, ~ 9 nm, as estimated from the data of [59] for PLA of $M_w = 200$ kg/mol being close to $M_w = 184$ kg/mol of the PLA used in this study), can sustain the low- ω elasticity if it connects the parallel plates (electrodes), thereby giving the early growth of elasticity at $t_E/t_E^* \cong 0.3$ (Fig. 4.2.3). At the same time, this inter-stack distance should have a distribution covering from the PLA chain size down to the hopping distance of electrons (due to the tunneling effect), ~ 1 nm [60], so that the electron hopping should/could have resulted in enhanced conduction even when the GNP stacks were separated by the “insulating” PLA before their direct contact. This electron hopping possibly led to mild growth in the electrical conductivity at $t_E/t_E^* < 1$ (Fig. 4.2.5) before the drastic increase in the conductivity occurred at $t_E/t_E^* = 1$ on formation of fully conductive GNP columns. In fact, a very similar explanation has been given by [61] for their observation of mechanical percolation occurring prior to electrical percolation in carbon nanotube composites.

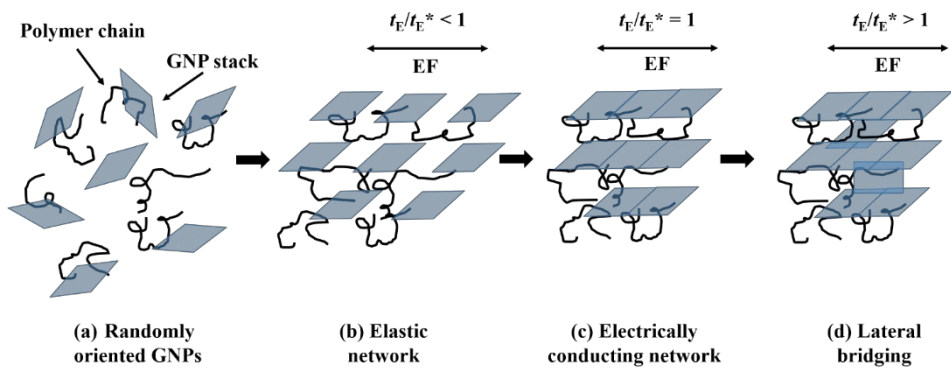


Fig. 4.2.6 Schematic illustration of GNP motion under a strong electric field. The direction of the applied AC electric field is indicated as EF (both-sided arrow).

After formation of the *soft* network explained above, the interaction between the induced dipoles of neighboring GNP stacks could induce translational motion of those stacks that organizes them into a conductive, chained-stack columnar structure, as illustrated in Fig. 4.2.6c. When such columns bridge the electrode, the short circuit occurs for the composite as a whole to give a drastic increase of the conductivity, as observed in Fig. 4.2.5 at $t_E/t_E^* = 1$. Those columns are rigid compared to the soft elastic network sustained by the PLA chains, and the elasticity of the composite levels off when those columns were formed. (Nevertheless, the columns should be much softer than the body of the GNP sheets because of the defects in the columns, as discussed previously on the basis of the rigidity analysis in Chapter 4.1.4.1.)

Once the short circuit occurs on the column formation explained above, the electrical current flows mostly along those columns and the residual GNP stacks out the columns experience essentially no electric force that organizes them into columns. Nevertheless, these left-over stacks could be still oriented locally and individually in the current direction to *softly* touch the neighboring columns (cf. Fig. 4.2.6d) and offer an extra conductive path to these columns, as speculated previously in Chapter 4.1.4.2. This “secondary structure” of the residual stacks could have resulted in the gradual increase of conductivity at $t_E/t_E^* > 1$ without significantly increasing the elasticity. (A hint of this “secondary structure” was observed in TEM images presented previously in Fig.

4.1.12. However, those images covered rather narrow areas in the composite, and further experiments characterizing the μm -sized (or larger) structure over the whole volume of the composite are required to fully analyze the secondary structure.)

A magnetic field generated by the AC current flowing through the columns might help this type of local orientation of the left-over stacks, as suggested from the behavior of nano-carbons in electromagnetic fluids [28-33, 62]: A magnetic field is known to align those nano-carbons parallel to the field. The orientation of the disk-like stack of GNP is specified by directions of two axes parallel to the disk surface. In the composites, the AC current flowing through the columns (on the short circuit) could have created a magnetic field normal to the current direction, and orientation of one axis of the residual stack in the magnetic field direction is equivalent to the orientation of the other axis in the current direction.

4.2.5. Further examination of time scale of structure formation

4.2.5.1. overview

In relation to the discussion of the rheological and electrical changes due to the columnar structure formation of GNP stacks (Chapters 4.2.2 and 4.2.3), it is of interest to examine dependence of the time t_E^* for this formation on the strength of the electric field E . In Fig. 4.2.7, the t_E^* data of the three concentrated composites ($\phi_{\text{GNP}} = 0.17, 0.28, \text{ and } 0.34 \text{ vol\%}$) at $190 \text{ }^\circ\text{C}$, summarized in Table 4.2.1, are double-logarithmically plotted against E . For respective ϕ_{GNP} , t_E^* decreases with increasing E (columns are formed more quickly under a stronger electric field), as easily expected. More quantitatively, this decrease becomes weaker for larger ϕ_{GNP} . These features can be discussed below in relation to the time required for motion of the GNP stacks.

In the simplest case, the internal electric field intensity E_{in} negligibly deviates from the applied field intensity E , and the induced dipole of the GNP stack, P , is proportional to $E_{\text{in}} = E$. For this case, the neighboring stacks being oriented in the electric field direction interact with each other through their induced dipoles, and the corresponding force acting on the stack is proportional to $P^2 \sim E^2$. Then, the time t_E^* required for formation of the chained-stack columns in a given composite is expected to be inversely proportional to this force, *i.e.*, to E^{-2} . Interestingly, in Fig. 4.2.7, the t_E^* data for the smallest $\phi_{\text{GNP}} (= 0.17 \text{ vol\%})$ *approximately*

exhibit this E^{-2} dependence. This result encourages a more quantitative comparison between the t_E^* data and a theoretical estimate, as explained below.

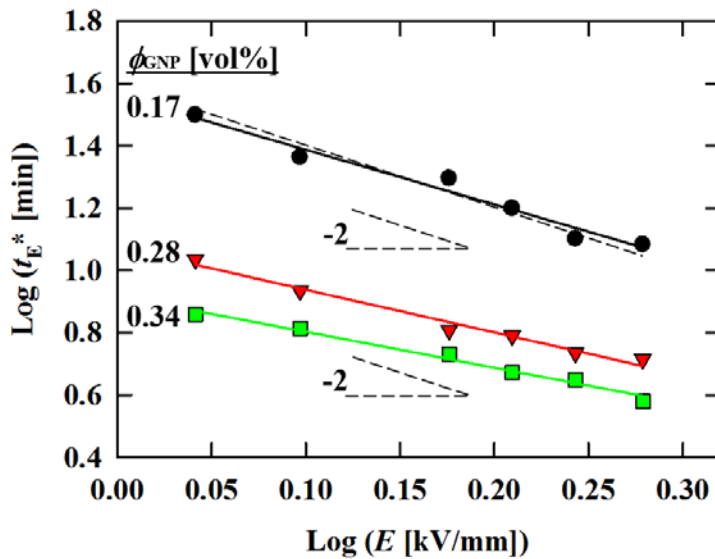


Fig. 4.2.7 Changes of the time t_E^* for formation of GNP columns under strong electric field with the field strength E observed for the composites with $\phi_{\text{GNP}} = 0.17, 0.28$ and 0.34 vol% at 190 °C. t_E^* is double-logarithmically plotted against E . Solid lines show results of power-law fitting. Dotted lines indicate a reference slope of -2 representing a relationship $t_E^* \propto E^{-2}$ expected for the simplest case.

4.2.5.2. estimate of translational and rotational times of GNP stack

For estimating the time t_E^* for the GNP column formation between the electrodes, it is first to focus on a time $t^{[2]*}$ for connection of the two nearest neighboring GNP stacks, the unit process of the column formation. (The number, 2, in the superscript represents that two GNP stacks are involved in the process.) For this unit process, the disk-like stacks as thin oblate spheroid inclusions having the minor and major axis lengths $2a$ and $2b$ that correspond to the thickness and length of the stack is modelled, as illustrated in Fig. 4.2.8b. (The side view of two inclusions is illustrated.) Lines of electric flux representing the interaction between the induced dipoles are shown schematically in Fig. 4.2.8c. After the inclusions *quickly* rotate to be aligned in the direction of the electric field as illustrated therein (and further discussed later), each of them has the field induced dipole $P = 2bq$ along the b -axis. The corresponding polarized charge is specified as [17]

$$q = \frac{V\alpha_p E}{2b} \quad (4.2.1)$$

where V is the volume of the inclusion, α_p is the polarizability along the major axis of the inclusion, and E is the electric field strength. (Here it is assumed that the internal field strength E_{in} coincides with the macroscopic E .) For the oblate-shaped inclusion, V and α_p are given by [63]

$$V = \frac{4\pi ab^2}{3} \quad (4.2.2)$$

$$\alpha_p = \frac{\varepsilon_m (\varepsilon_i - \varepsilon_m)^2}{[\varepsilon_m + (\varepsilon_i - \varepsilon_m)L_p]\varepsilon_i} \quad (4.2.3)$$

Here, ε_i and ε_m are the *absolute* permittivities of the inclusion and medium, respectively, and L_p is the depolarization factor along the major axis of the oblate-shaped inclusion defined as

$$L_p = \frac{a}{2b} \left(\frac{\pi}{2} - \frac{a}{b} \right) \quad (4.2.4)$$

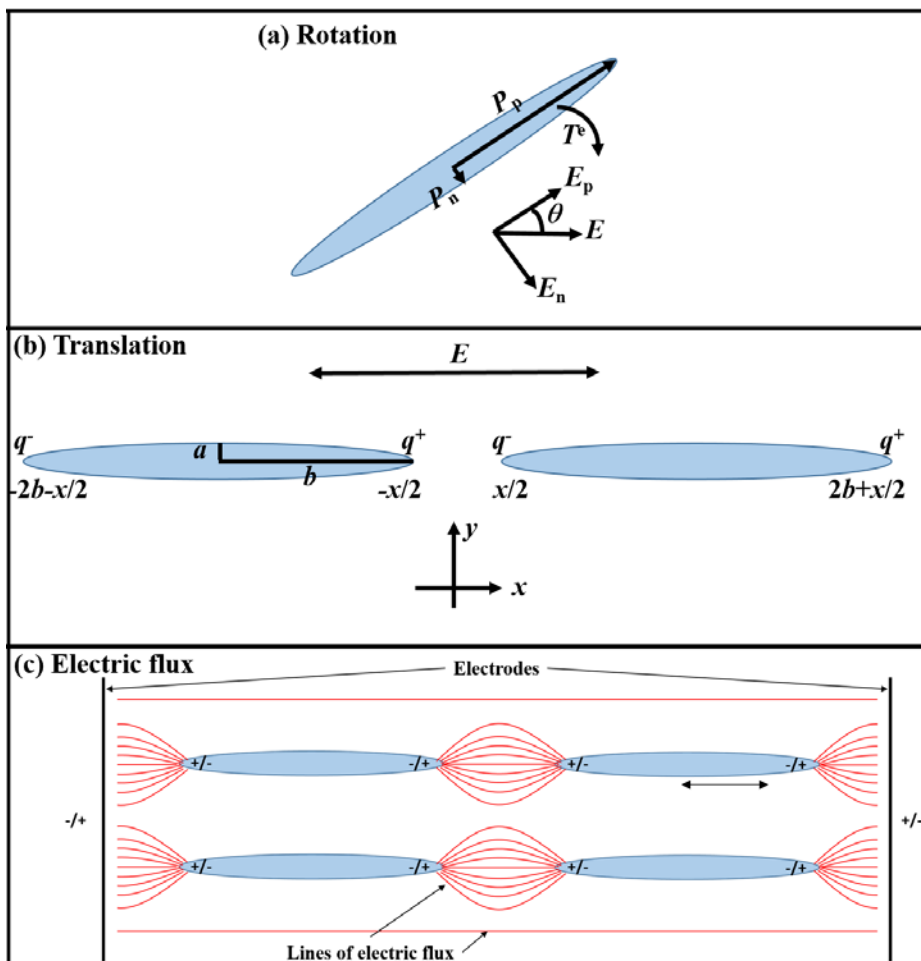


Fig. 4.2.8 Schematic illustration of alignment of GNP stacks for (a) rotational and (b) translational motion under electric field. The lines of electric flux representing the interaction between the induced dipoles of neighboring GNP stacks are schematically shown in (c).

A spatial coordinate (x,y) is introduced as indicated in Fig. 4.2.8b. It is considered that the two inclusions are aligned along the x axis and have the edges at $(-2b-x/2, 0)$ and $(-x/2, 0)$ (for the left inclusion) and at $(x/2, 0)$ and $(2b+x/2, 0)$ (for the right inclusion), thereby having the closest inter-edge distance of x . These inclusions are aligned in the electric field direction and no electrical torque acts on them. (This alignment can be quickly achieved, as discussed later in more detail.) Then, the net electric force F^e acting on the right inclusion in the x direction is specified as,

$$F^e = \frac{q^2}{4\pi\epsilon_m} g(x) \quad (4.2.5a)$$

with

$$g(x) = -\frac{1}{x^2} + \frac{2}{(x+2b)^2} - \frac{1}{(x+4b)^2} \quad (4.2.5b)$$

This F^e is negative (because $x > 0$) and the right inclusion moves to the left direction. On the other hand, a counter force $-F^e (> 0)$ acts on the left inclusion so that this inclusion moves to the right direction. The total force acting on the system of the two inclusions is zero, and thus the center of mass of the system, located at $x = 0$, does not move. Namely, the two inclusions are connected into a column when their neighboring ends move to $x = 0$. This motion occurs against a viscous frictional force exerted from the medium. For the right inclusion illustrated in Fig. 4.2.8b, this viscous force is specified in terms of the velocity of this inclusion, v

= $d(x/2)/dt$, as

$$F^v = -\eta k_t v = -\left(\frac{\eta k_t}{2}\right) \frac{dx}{dt} \quad (> 0 \text{ for the right inclusion}) \quad (4.2.6)$$

Here, η is the medium viscosity, and k_t is the translational friction coefficient for the oblate-shaped inclusion given by [64],

$$k_t = 6\pi(ab^2)^{1/3} \frac{\sqrt{(a/b)^{-2} - 1}}{(a/b)^{-2/3} \tan^{-1} \sqrt{(a/b)^{-2} - 1}} \quad (4.2.7)$$

In eq 4.2.6, the squeezing lubricant force acting between the two inclusions has been neglected, assuming that the inclusions are thin ($a \ll b$).

For such a thin inclusion, the inertia force can be safely neglected, too. Furthermore, the thermal Brownian force F^B can also be neglected compared to the force F^e due to the strong electric field examined ($E \geq 1.10$ kV/mm), as explained earlier for Figs. 4.2.2 and 4.2.4. Then, the motion of the right inclusion illustrated in Fig. 4.2.8b is described by a force balance equation, $F^e + F^v = 0$, which is straightforwardly cast in a time evolution equation of x (cf. eqs 4.2.5 and 4.2.6),

$$\frac{dx}{dt} = Ag(x) \quad \text{with } A = \frac{2q^2}{4\pi\epsilon_m \eta k_t} \quad (4.2.8)$$

For the initial condition, $x = x_s$ (starting separation) at $t = 0$, and the final condition, $x = 0$ (connection of two inclusions) at $t = t^{[2]*}$, eq 4.2.8 can

be analytically integrated to find

$$t^{[2]*} = \frac{1}{A} \int_{x_s}^0 \frac{1}{g(x)} dx$$

$$= \frac{8b^3}{A} \left\{ \frac{1}{30} \xi_s^5 + \frac{1}{6} \xi_s^4 + \frac{13}{54} \xi_s^3 + \frac{1}{18} \xi_s^2 - \frac{1}{27} \xi_s - \frac{1}{27} \frac{1}{\sqrt{3}} \ln \left[\frac{\lambda_+ (\xi_s - \lambda_-)}{\lambda_- (\xi_s - \lambda_+)} \right] \right\}$$

(4.2.9a)

with

$$\xi_s = \frac{x_s}{2b}, \quad \lambda_+ = -1 + \sqrt{1/3}, \quad \lambda_- = -1 - \sqrt{1/3} \quad (4.2.9b)$$

(In the integral, the following analytical identity has been utilized,

$$\left\{ -\frac{1}{\xi^2} + \frac{2}{(\xi+1)^2} - \frac{1}{(\xi+2)^2} \right\}^{-1}$$

$$= -\frac{1}{6} \xi^4 - \frac{2}{3} \xi^3 - \frac{13}{18} \xi^2 - \frac{1}{9} \xi + \frac{1}{27} - \frac{1}{27\sqrt{3}} \left(\frac{1}{\xi - \lambda_+} - \frac{1}{\xi - \lambda_-} \right)$$

.)

The factor A appearing in eq 4.2.9 is proportional to q^2 (cf. eq 4.2.8) and thus to E^2 (cf. eq 4.2.1), so that $t^{[2]*}$ estimated from the above simple analysis is proportional to E^{-2} .

For the composite with a rather low GNP content, $\phi_{\text{GNP}} = 0.17$ vol% (that gives $t_E \sim E^{-2}$, cf. Fig. 4.2.7), the parameters were estimated as $\varepsilon_m = 10\varepsilon_0$, $\varepsilon_i = 10^5\varepsilon_0$ (similar to carbon nanotube [65]), $\eta = 1000$ Pa·s (matrix PLA viscosity), $a = 50$ nm and $b = 5$ μm (according to the manufacturer's

specifications), $V = 5.24 \times 10^{-18} \text{ m}^3$, $\alpha_p = 1.12 \times 10^{-8} \text{ F/m}$, $k_t = 6.05 \times 10^{-5} \text{ m}$, and $x_s \cong \{\pi a^2/4\phi_{\text{GNP}}\}^{1/2} \cong 10 \text{ }\mu\text{m}$ (calculation of x_s follows [13]). With these estimates and the value of the absolute permittivity of vacuum, $\epsilon_0 = 8.854 \times 10^{-12} \text{ F/m}$, eq 4.2.9 gives $t^{[2]*} \cong 2.5 \text{ min}$ (150 s) for $E = 1.75 \text{ kV/mm}$. This estimate of $t^{[2]*}$ is not identical to (though not tremendously different from) the t_E^* data of the corresponding composite, $t_E^* = 12.6 \text{ min}$ for $E = 1.75 \text{ kV/mm}$ (cf. Fig. 4.2.7). However, the connection of just two oblate spheroids (Fig. 4.2.8(b)) serves merely as the unit (most localized) process for *full* formation of the GNP column between the electrodes, so that $t^{[2]*}$ for this unit process does not necessarily agree with the column formation time t_E^* , as discussed below in more detail.

The t_E^* data are insensitive to the GNP sample thickness L (when E remains the same), as explained earlier. Thus, the time for the full column formation is governed by local motion of the GNP stacks occurring in a length scale $< L$, as explained in Chapter 4.2.1. However, the connection of just two GNP stacks (requiring the time $t^{[2]*}$) may occur too locally thereby not serving as the rate-determining step for the full column formation. Consequently, connection of a few more GNP stacks, occurring in a larger but still local length scale, may serve as the rate-determining step.

As a trial, a time required for connecting 4 GNP stacks, $t^{[4]*}$ can be estimated. This $t^{[4]*}$ can be roughly estimated as a time for connecting a

pair of structures formed after the unit process explained above (eqs 4.2.1-4.2.9) with each structure containing two oblate spheroids (two GNP stacks) as schematically represented in Fig. 4.2.9a. This situation is similar to that illustrated in Fig. 4.2.8b, except that the inclusion is no longer the thin oblate spheroid but is regarded as a thin, longer ellipsoid having the axis lengths of $4b$, $2a$, and $2b$ in the x , y , and z directions (following the spatial coordinate given in Fig. 4.2.8b), and that the initial separation between the neighboring edges of the two ellipsoids is given by $2x_s$ (with x_s being the initial separation considered for the unit process). The charge q polarized at the ellipsoid edges is still given by eq 4.2.1, because the volume to axial length ratio (V/b) and the polarizability (α_P) appearing in eq 4.2.1 do not change on the connection of the two oblate spheroids. In contrast, the friction coefficient k_t becomes double when those two oblate spheroids are connected to become the motional unit (because of the double-folded increase of the surface area.) Then, the equation of motion, eq 4.2.8, remains formally identical for the thin, long ellipsoid so that the time $t^{[4]*}$ required for connection of two longer ellipsoids (i.e., 4 GNP stacks) is still given by eq 4.2.9 except that the factor b (semi-axis length in the x direction) appearing therein is replaced by $2b$ and the other factor $A(\propto k_t^{-1})$, by $A/2$. (The normalized initial separation ξ_s defined by eq 4.2.9b remains the same as in the case of the unit process, because the factors x_s and b included in ξ_s are commonly doubled when the connected two GNP stacks is considered as the

motional unit.) Thus, a simple relationship between $t^{[2]*}$ (for the unit process) and $t^{[4]*}$ (for connection of two longer ellipsoids), $t^{[4]*} \cong 16t^{[2]*}$ with $t^{[2]*} \cong 2.5$ min is noted as estimated above. Then, the time for forming the connected sequence of 4 GNP stacks from the initial state (where the GNP stacks were not connected) is roughly estimated as

$$t_E^* \cong t^{[2]*} + t^{[4]*} \cong 42.5 \text{ min (for } E = 1.75 \text{ kV/mm)} \quad (4.2.10)$$

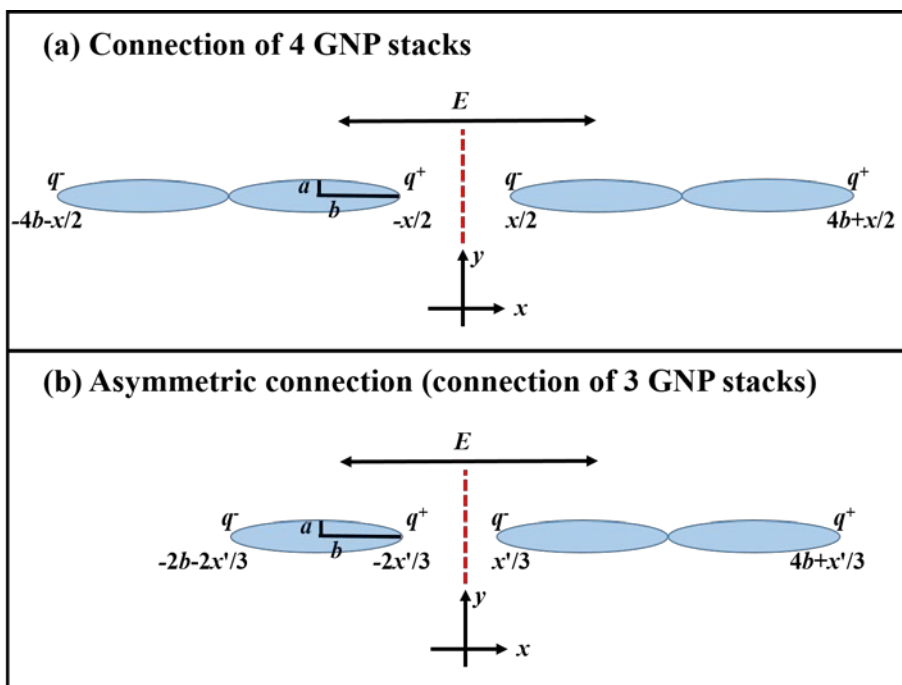


Fig. 4.2.9 Schematic illustration of possible sequential motions of GNPs serving for the rate-determining step: Connection of (a) 4 GNP stacks and (b) 3 GNP stacks.

In another trial, as the rate-determining step mentioned above, formation of a sequence of three GNP stacks resulting from asymmetric connection of a single GNP stack with a sequence of two stacks (formed through the unit process) may be considered, as schematically illustrated in Fig. 4.2.9b. The time $t^{[3]*}$ required for this asymmetric connection can be estimated in a way essentially identical to that explained for eqs 4.2.1-4.2.9. For the asymmetric connection, the single GNP stack can be treated as a thin oblate spheroid and the two connected GNP stacks (formed through the unit process) as a longer ellipsoid. In the coordinate (x,y) illustrated in Fig. 4.2.8b, two inclusions are aligned along the x axis and have the edges at $(-2x'/3-2b,0)$ and $(-2x'/3,0)$ (for the single GNP stack located in the left side) and at $(x'/3,0)$ and $(x'/3+4b,0)$ (for the connected two GNP stacks in the right side). Then, the net electric force $F^{e'}$ for the left inclusion, acting in the x direction, is described as a function of the closest inter-edge distance x' as

$$F^{e'} = \frac{q^2}{4\pi\epsilon_m} g'(x') \quad (4.2.11a)$$

with

$$g'(x') = \frac{1}{x'^2} + \frac{1}{(x'+6b)^2} - \frac{1}{(x'+2b)^2} - \frac{1}{(x'+4b)^2} \quad (4.2.11b)$$

A counter force $-F^{e'}$ acts on the right inclusion, and the center of mass of the two inclusions, located at $(0,0)$ is subjected to no electrical force.

Thus, the two inclusions are connected when the neighboring edges at the coordinates $(-2x'/3,0)$ and $(x'/3,0)$ move to the center of mass, namely, when x' becomes zero. The time $t^{[3]*}$ required for this connection can be estimated by focusing on the left inclusion. The velocity of this inclusion, $v = d\{-2x'/3\}/dt$, is determined by a balance of the electric force $F^{e'}$ (eq 4.2.11) and the viscous force, the latter being given by

$$F^{v'} = -\eta k_t v = \left(\frac{2\eta k_t}{3} \right) \frac{dx'}{dt} \quad (< 0 \text{ for the left inclusion}) \quad (4.2.12)$$

where η is the medium viscosity and k_t is the translational friction coefficient of the left inclusion (single GNP stack) specified by eq 4.2.7. Neglecting the inertia and the Brownian force (as in the case of the unit process), the time $t^{[3]*}$ can be estimated from the force balance equation, $F^{e'} + F^{v'} = 0$, as

$$t^{[3]*} = \frac{4}{3A} \int_{x'_s}^0 \frac{1}{g'(x')} dx' \cong 12.1 \text{ min} \quad (4.2.13)$$

with the factor A for the single GNP stack being specified in eq 4.2.8. The integral in eq 4.2.13 was conducted numerically for the known A and b values (described for the unit process) and the initial separation of $x'_s = 1.5x_s = 15 \mu\text{m}$ being estimated as the average separation between the neighboring edges of the two inclusions at $t = 0$ (as done in the estimation of $t^{[4]*}$). This $t^{[3]*}$ allows to estimate the time necessary for asymmetric connection of 3 GNP stacks from the initial state (where the

GNP stacks are disconnected) as

$$t_E^* \cong t^{[2]*} + t^{[3]*} \cong 14.6 \text{ min (for } E = 1.75 \text{ kV/mm)} \quad (4.2.14)$$

This estimate of t_E^* (eq 4.2.14 for connection of 3 GNP stacks) is close to the t_E^* data (12.6 min), and the other estimate (eq 4.2.10 for connection of 4 GNP stacks) deviates from the data but this deviation is not fatally large. These results lend support to the structural hypothesis that local motion involving a few GNP stacks serves as the rate-determining step for the full formation of GNP columns connecting the electrodes. At the same time, it should be emphasized that the above argument for estimating t_E^* includes several uncertain points and is a very crude argument. Namely, the argument neither considers all possible modes of local motion (such as the asymmetric connection of a single GNP stack to a larger sequence of more than two stacks) nor fully specifies the number of the GNP stacks involved in the local, rate-determining step.

In addition to those uncertainties, it has to be hastened to add that the above argument gives $t_E^* \propto E^{-2}$ irrespective of the modes of local motion and the number of GNP stacks considered therein. Nevertheless, some deviation from this E^{-2} dependence has been already noted experimentally even for the smallest ϕ_{GNP} (cf. circles in Fig. 4.2.7), and this deviation becomes more prominent for larger ϕ_{GNP} (cf. triangles and squares in Fig. 4.2.7). This weakening of the E dependence of the t_E^*

data could reflect the screening of the internal electric field (giving $E_{in} < E$) that is enhanced for large ϕ_{GNP} . In addition, the weakening might be also related to saturation of the induced dipole (giving E_{in} -insensitive P) for large E . Furthermore, it is also noted that η appearing in eq 4.2.9 may need to be modified for the matrix PLA chains bridging the neighboring GNP stacks (cf. Fig. 4.2.6b): η could change with ϕ_{GNP} for such a case. Despite all these uncertainties, the above comparison of the estimate and data of t_E^* suggests the basic validity of the argument relating t_E^* to the local stack motion driven by the interaction between electric field-induced dipoles.

Here, it should also be noted that the above argument (implicitly) assumed that the rotational motion of the isolated stacks, necessary to make the configuration illustrated in Fig. 4.2.8b, was much faster than the translational motion of the stacks. This point is examined below with the aid of a rough estimate of the rotational time, t_r .

For the composites examined in Fig. 4.2.7, this fast rotational process, occurring prior to the translational motion discussed above, was not resolved *via* optical microscopy (OM) observation because of the difficulty (full coverage of view field with GNP stacks) explained earlier. Thus, the OM observation was restricted to the very dilute composite with $\phi_{GNP} = 0.028$ vol% (Fig. 4.2.1) and it was attempted to extract a characteristic feature of the rotational process.

As illustrated in Fig. 8a, the electric torque T^e acting on the isolated

GNP stack (modeled as a very thin oblate spheroid) can be expressed as

$$T^e = P_p E_n - P_n E_p \quad (4.2.15)$$

Here, P_p and E_p denote the components of the induced dipole and field intensity in the direction of the major axis of the oblate spheroid, and P_n and E_n , those in the direction normal to this axis (cf. Fig. 4.2.8a). P_x ($x = p, n$) is related to E_x and the component α_x of the polarizability in respective directions as $P_x = V\alpha_x E_x$ (cf. eq 4.2.1). Thus, eq 4.2.15 can be rewritten as

$$T^e = V(\alpha_p - \alpha_n)E^2 \sin \theta \cos \theta \quad (4.2.16)$$

where θ is the angle between the major axis of the oblate spheroid and the electric field (cf. Fig. 4.2.8a). Since $\alpha_p \gg \alpha_n$, α_n in eq 4.2.16 can be neglected to find

$$T^e = \frac{V\alpha_p E^2 \sin 2\theta}{2} \quad (4.2.17)$$

Neglecting the inertia for the GNP stack and the Brownian force for the GNP stack (as explained just after eq 4.2.7), it may be considered that the rotational motion of the GNP stack is determined by a balance of this electrical torque T^e and a viscous torque T^v , the latter being expressed in terms of the angular velocity of the stack Ω and the medium viscosity η as [17]

$$T^v = -\eta\Omega k_r \quad (4.2.18)$$

Here, k_r is the rotational friction coefficient for the oblate-shaped inclusion. For the GNP stack modeled as the thin oblate spheroid, this k_r is related to the translational friction coefficient k_t (eq 7) as [64]

$$k_r = 8\pi ab^2 \frac{4\{1-(a/b)^{-4}\}}{3(a/b)^{-2} \left[\frac{2(a/b)^{2/3} \{2-(a/b)^{-2}\}}{\left\{ \frac{k_t}{6\pi(ab^2)^{1/3}} \right\}} - 2 \right]} \quad (4.2.19)$$

Balancing T^e and T^v ($T^e + T^v = 0$) and replacing Ω by $-d\theta/dt$ give

$$-\eta k_r \frac{d\theta}{dt} = \frac{V\alpha_p E^2}{2} \sin 2\theta \quad (4.2.20)$$

Equation 4.2.20 can be rewritten for the GNP stack (thin oblate spheroid) rotating from the initial angle θ_0 at $t = 0$ to a final angle θ' at the time t_r :

$$t_r = \int_0^{t_r} dt = -\frac{2\eta k_r}{V\alpha_p E^2} \int_{\theta_0}^{\theta'} \frac{1}{\sin 2\theta} d\theta \quad (4.2.21)$$

Integration of eq 4.2.21 can be conducted analytically to give

$$t_r = \frac{\eta k_r}{V\alpha_p E^2} \ln \left(\frac{\tan \theta_0}{\tan \theta'} \right) \quad (4.2.22)$$

Equation 4.2.17 underlying eq 4.2.22 considers the *simplest case* of no correction for the internal field intensity and no saturation of the induced dipole, so that it gives the torque on the GNP stack due to the induced dipole being proportional to the applied electric field, $P \sim \alpha_p E$. Correspondingly, eq 4.2.22 includes the factor representing this interaction, $PE \sim \alpha_p E^2$ (not the other factor $P^2 \sim q^2 \sim \alpha_p^2 E^2$ explained for eq 4.2.9).

In Fig. 4.2.1, $\theta_0 = 68^\circ$ at $t_E = 0$ s and $\theta' = 18^\circ$ at $t_E = 19$ s have been roughly estimated for a representative GNP stack highlighted with the circles. The corresponding t_r value for $E = 2.5$ kV/mm was estimated from eq 4.2.22, with $k_r = 1.33 \times 10^{-15}$ m³ and the rest of the parameters having the same values as in eq 4.2.9. The resulting estimate, $t_r \cong 7.4$ s, is in the same order of magnitude with the observed rotational time, 19 s. This semi-quantitative agreement lends support to the idea of fast electric field-driven rotation ($t_r \ll t_E^*$), although some consideration needs to be made for the corrections for the internal field intensity (in particular for large ϕ_{GNP}) and saturation of the induced dipole (prominent for large E), as similar to the situation explained for the time t_t for the translational motion.

Much more importantly, eq 4.2.22 suggests that the rotation is very slow for the GNP stacks oriented initially normal to the electric field: Note that eq 4.2.22 gives $t_r = \infty$ for $\theta_0 = 90^\circ$ (because a net electrical torque vanishes for such a stack having the normal orientation). Thus,

the rotation occurs quickly only for the stacks having θ_0 well below 90° in the as-prepared composites (in the initial state), and only those quickly rotating stacks participate in the second-step structural evolution, formation of the chained-stack columns. In other words, the left-over stacks being not included in the columns (discussed for Fig. 4.2.6d) is a natural consequence of the isotropic orientation (broad distribution of θ_0) of the stacks in the as-prepared composites.

5. Summary

This thesis aimed to study the effect(s) of the AC electric field-induced graphene nanoplatelet (GNP) networks on the rheological and electrical properties of poly(lactic acid) (PLA)/GNP composites and to find the correlation between the GNP structure and the composite properties by varying the GNP concentration or application intensity/time of the electric field.

For the melt-compounded PLA composites containing GNPs at various but low volume fractions ($\phi_{\text{GNP}} \leq 0.34$ vol%), this thesis investigated the correlation(s) between the structure of GNP stacks and the composite properties. Using the modified parallel plates of a rheometer that served as both the rheological measurement fixture and the electrodes, a strong but fixed AC electric field (60 Hz, 1.75 kV/mm) was applied to the composites loaded between the plates up to the occurrence of electrical short circuit. Optical microscopy, transmission electron microscopy, and 2D wide-angle X-ray diffraction revealed that the almost randomly oriented thin stacks of GNPs in the as-fabricated composites were oriented in the field direction and subsequently developed into the chained-stack structure in that direction. The as-fabricated composites before application of the electric field behaved as viscous fluids almost indistinguishable from the neat PLA matrix, whereas after application of the field, the composites exhibit a solid-like response characterized by ω -insensitive storage modulus G' at low ω . The loss modulus, G'' , was hardly affected by the electric field, implying that the chained-stack structure is an elastic structure bridging the two plates. Through this bridging, electrons can flow from one plate to the

other, thus making the composites electrically conductive when $\phi_{\text{GNP}} \geq 0.17$ vol%. The correlation between the chained-stack structure and the composite properties was examined through quantitative analysis. It turned out that the chained-stack structure cannot be a single rigid slab but possibly includes inter-stack junctions (defects) being softer and less conductive than the single graphene nanoplate. Furthermore, examination of the ϕ_{GNP} dependence of the equilibrium modulus and static electrical conductance suggested that the left-over GNP stacks, being not involved in the chained-stack structure (primary structure formed by the strong electric field), were elastically inert but still offered an extra conductive path to the primary structure.

Meanwhile, for the melt-compounded PLA composite containing GNPs at a low but fixed volume fraction ($\phi_{\text{GNP}} = 0.34$ vol%), this thesis also focused on the growths of mechanical elasticity and electrical conductivity on application of a strong AC electric field, and investigated difference in the behavior of those properties on formation of higher-order structures induced by the electric field. The GNP composite was subjected to the AC electric field (60 Hz) of various intensities E for various times t_E at 190 °C. The optical microscopy observation made for a dilute composite with $\phi_{\text{GNP}} = 0.028$ vol% revealed that a fraction of randomly oriented thin stacks of GNPs in the as-prepared composite was firstly aligned in the electric field direction and subsequently chained into columnar structure oriented in that direction. For a concentrated composite with $\phi_{\text{GNP}} = 0.34$ vol% subjected to the strong electric field for a sufficiently long time, electrical short circuit occurred and thus the

conductive GNP columns were fully formed to bridge the electrodes. Both of the low-frequency storage modulus $G'(\omega = 0.1)$ and the static (dc) electrical conductivity σ_{dc} grew on this column formation, and their growths were characterized by the time t_E^* for the occurrence of electrical short circuit (for the GNP bridge formation). An approximate but simple theoretical analysis successfully gave an order of magnitude estimate for t_E^* . For various E , $G'(\omega = 0.1)$ and σ_{dc} behaved as functions of a single, reduced time t_E/t_E^* and were collapsed into respective master curves when plotted against t_E/t_E^* . This result suggests that the growths of both $G'(\omega = 0.1)$ and σ_{dc} were synchronized with the GNP column formation. However, the quantitative analysis revealed that the growth of $G'(\omega = 0.1)$ was fast and saturated by the time $t_E \cong t_E^*$, whereas the growth of σ_{dc} was slower and continued even at $t_E > t_E^*$. This quantitative difference was discussed in relation to the matrix PLA chains that would have mechanically bridged neighboring GNP stacks thereby enhancing $G'(\omega = 0.1)$ but not σ_{dc} , and also to the left-over GNP stacks (not included in the GNP column) that would have *softly* touched neighboring columns at long times ($t_E > t_E^*$) to offer an extra conductive path and allow σ_{dc} to keep increasing without significantly affecting $G'(\omega = 0.1)$. An approximate but simple theoretical analysis, successfully giving an order of magnitude estimate for the time required for the rotation of single GNP stack, suggested that the random orientation of the GNP stacks in the as-prepared composite naturally gave those left-over GNP stacks.

국문 초록

본 논문에서는 전기장 인가에 따른 그래핀 나노플레이트 (GNP) 네트워크 구조 형성이 폴리락틱산/GNP 복합체의 유변물성 및 전기적 특성에 미치는 영향에 대해서 알아보고, GNP 구조와 복합체 물성과의 상관관계를 규명하였다.

낮은 GNP 함량 ($\phi_{\text{GNP}} \leq 0.34 \text{ vol\%}$)의 복합체에 대해, 본 논문에서는 복합체의 물성과 고정된 교류 전기장 (주파수와 강도가 각각 60 Hz, 1.75 kV/mm) 인가에 의해 형성된 GNP 구조간의 상관관계에 대해 연구하였다. 레오미터 평행 판 사이에 위치한 복합체에 전기장을 인가함으로써 평행 판 자체가 전극과 유변물성을 측정하는 픽스처 역할을 동시에 수행하였다. 광학 현미경, TEM, 그리고 이차원의 고각도 x-레이 산란 기법을 통하여 전기장 인가 전에는 거의 랜덤하게 배향된 GNP 들이 전기장 인가 후에는 인가 방향으로 배향되고, 긴 체인 (칼럼) 구조를 형성하는 것을 확인하였다. 이러한 GNP 체인 구조가 두 전극 사이를 연결하기 위해서는 ϕ_{GNP} 가 임계함량 ϕ_{GNP}^* ($\geq 0.17 \text{ vol\%}$)보다 높아야 한다는 것을 전기 단락의 발생을 통해 알아냈다. 이러한 구조 변화와 맞물려, 전기장 인가 전에는 탄성 계수 G' 이 중간-낮은 영역의 주파수 ω 에서 거의 ω^2 에 비례하였지만 전기장 인가 후에는 저주파수 영역의 G' 이 ω 에 관계없이 거의 일정하였다. 하지만 손실 계수 G'' 의 경우 전기장 인가와

상관 없이 낮은 ω 영역에서 ω^2 에 비례하였다. 이를 통하여 ϕ_{GNP}^* 이후에 형성된 전극 사이를 연결하는 GNP 체인 구조는 탄성적인 가교 역할을 한다는 것을 알 수 있었다. 이러한 탄성 가교 역할을 하는 GNP 칼럼 구조는 동시에 전도성 통로의 역할을 함으로써 ϕ_{GNP}^* 이후 부도체에서 전도체의 전이가 일어나는 양상을 확인하였다. 전기장 인가 후 ϕ_{GNP}^* 이후의 평형 탄성 계수와 dc 전도도의 정량적인 분석을 통해 GNP 체인 구조는 단단한 하나의 평판 구조가 아니라 사이 사이에 GNP에 비해 훨씬 유연하고 전도성이 낮은 접합부를 포함하는 것을 확인하였다. 또한 ϕ_{GNP}^* 이후의 입자 함량에 따른 평형 탄성 계수와 dc 전도도의 상관관계를 통해 일차적으로 전기장 방향으로 형성된 GNP 칼럼 구조 형성 후 남은 GNP가 국소적인 움직임을 통해 탄성적으로 비활성화된 이차 구조를 형성하는 것으로 추론되었다. 이러한 이차 구조는 일차적으로 형성된 칼럼 구조에 부드럽게 붙어 있기에 탄성적인 측면에서는 효과가 미비하지만 전기적 통로의 역할을 할 수 있기에 전도성 증가에는 효과가 있는 것으로 추론하였다.

한편, 고정된 $\phi_{\text{GNP}} = 0.34 \text{ vol\%}$ 의 복합체에 대해, 본 논문에서는 다양한 전기장 인가 세기 E 및 시간 t_E 을 따른 유변 물성과 전기적 물성의 성장에 대해 알아보았고 이를 GNP 구조와 연관 지어 상관관계를 규명하였다. 묶은 $\phi_{\text{GNP}} = 0.028 \text{ vol\%}$ 복합체의 전기장 인가에 따른 구조 변화를 광학 현미경을 통해 실시간으로 관찰한 결과 무질서하게 배향된

GNP 입자의 일부분이 먼저 전기장 인가 방향으로 배향되고, 긴 체인 구조를 형성하였다. 이러한 GNP 체인 구조 과정은 저주파수 영역의 탄성계수 $G'(\omega = 0.1)$ 와 dc 전도도 σ_{dc} 의 증가와 정성적으로는 비슷하게 나타났다. 이러한 각각의 물성 증가 거동을 잘 나타내는 정량적인 지표가 t_E^* 이다. t_E^* 의 경우 특정 전기장 인가 세기 하에 전기적 단락이 일어날 때까지 걸리는 시간을 나타낸다. $G'(\omega = 0.1)$ 와 σ_{dc} 모두 t_E/t_E^* 에 의해 중첩이 되어 마스터 플롯을 그리는 것으로 보아 GNP 칼럼 구조의 형성 과정은 물성의 증가 과정과 일치한다는 것을 알 수 있었다. 하지만 정량적으로는 $G'(\omega = 0.1)$ 의 경우 $t_E/t_E^* < 1$ 일 때, 즉 전기적 단락이 일어나기 이전에 가파른 상승세를 보이고 $t_E/t_E^* = 1$ 이 될 때에 포화가 되는 반면 σ_{dc} 의 경우 $t_E/t_E^* = 1$ 이 되어서야 급진적으로 증가하고 $t_E/t_E^* \gg 1$ 에도 계속해서 점진적으로 증가하였다. 두 물성 간의 정량적인 차이는 PLA 체인에 탄성적으로 연결된 GNP 입자와 칼럼구조를 형성하고 남은, 탄성적으로는 비활성화된 잔여 GNP 입자에 의해 설명될 수 있다.

복합체의 물성과 전기장 인가에 의해 형성된 GNP 네트워크 구조의 상관관계를 조사한 본 논문은 GNP 입자의 우수한 특성을 복합체 내에서 최대한 발현하기 위해서는 입자의 미세구조, 특히 배향 제어가 필수적임을 강조하고 있다.

주요어: 전기장, 그래핀 나노플레이트, 폴리락틱산,
생분해성 복합체, 고분자 유변학, 유전특성

학 번: 2014-30248

References

1. Filippone, G., M. Salzano de Luna, D. Acierno, and P. Russo, *Elasticity and structure of weak graphite nanoplatelet (GNP) networks in polymer matrices through viscoelastic analyses*. Polymer, 2012. **53**(13): p. 2699-2704.
2. Li, Y., J. Zhu, S. Wei, J. Ryu, L. Sun, and Z. Guo, *Poly(propylene)/Graphene Nanoplatelet Nanocomposites: Melt Rheological Behavior and Thermal, Electrical, and Electronic Properties*. Macromolecular Chemistry and Physics, 2011. **212**(18): p. 1951-1959.
3. Ramirez, C., F.M. Figueiredo, P. Miranzo, P. Poza, and M.I. Osendi, *Graphene nanoplatelet/silicon nitride composites with high electrical conductivity*. Carbon, 2012. **50**(10): p. 3607-3615.
4. Sabzi, M., L. Jiang, F. Liu, I. Ghasemi, and M. Atai, *Graphene nanoplatelets as poly (lactic acid) modifier: linear rheological behavior and electrical conductivity*. Journal of Materials Chemistry A, 2013. **1**(28): p. 8253-8261.
5. Wang, F., L.T. Drzal, Y. Qin, and Z. Huang, *Mechanical properties and thermal conductivity of graphene nanoplatelet/epoxy composites*. Journal of Materials Science, 2015. **50**(3): p. 1082-1093.
6. Wang, Y., J. Yu, W. Dai, Y. Song, D. Wang, L. Zeng, and N. Jiang,

- Enhanced thermal and electrical properties of epoxy composites reinforced with graphene nanoplatelets*. *Polymer Composites*, 2015. **36**(3): p. 556-565.
7. Shevchenko, V.G., S.V. Polschikov, P.M. Nedorezova, A.N. Klyamkina, A.N. Shchegolikhin, A.M. Aladyshev, and V.E. Muradyan, *In situ polymerized poly(propylene)/graphene nanoplatelets nanocomposites: Dielectric and microwave properties*. *Polymer*, 2012. **53**(23): p. 5330-5335.
 8. Yadav, S.K. and J.W. Cho, *Functionalized graphene nanoplatelets for enhanced mechanical and thermal properties of polyurethane nanocomposites*. *Applied Surface Science*, 2013. **266**: p. 360-367.
 9. Ke, K., Y. Wang, X.-Q. Liu, J. Cao, Y. Luo, W. Yang, B.-H. Xie, and M.-B. Yang, *A comparison of melt and solution mixing on the dispersion of carbon nanotubes in a poly(vinylidene fluoride) matrix*. *Composites Part B: Engineering*, 2012. **43**(3): p. 1425-1432.
 10. Prashantha, K., J. Soulestin, M.F. Lacrampe, P. Krawczak, G. Dupin, and M. Claes, *Masterbatch-based multi-walled carbon nanotube filled polypropylene nanocomposites: Assessment of rheological and mechanical properties*. *Composites Science and Technology*, 2009. **69**(11–12): p. 1756-1763.
 11. Lim, C.S., A.J. Rodriguez, M.E. Guzman, J.D. Schaefer, and B.

- Minaie, *Processing and properties of polymer composites containing aligned functionalized carbon nanofibers*. Carbon, 2011. **49**(6): p. 1873-1883.
12. Takahashi, T., T. Murayama, A. Higuchi, H. Awano, and K. Yonetake, *Aligning vapor-grown carbon fibers in polydimethylsiloxane using dc electric or magnetic field*. Carbon, 2006. **44**(7): p. 1180-1188.
 13. Osazuwa, O., M. Kontopoulou, P. Xiang, Z. Ye, and A. Docoslis, *Electrically conducting polyolefin composites containing electric field-aligned multiwall carbon nanotube structures: The effects of process parameters and filler loading*. Carbon, 2014. **72**: p. 89-99.
 14. Park, C., J. Wilkinson, S. Banda, Z. Ounaies, K.E. Wise, G. Sauti, P.T. Lillehei, and J.S. Harrison, *Aligned single-wall carbon nanotube polymer composites using an electric field*. Journal of Polymer Science Part B: Polymer Physics, 2006. **44**(12): p. 1751-1762.
 15. Oliva-Avilés, A.I., F. Avilés, V. Sosa, A.I. Oliva, and F. Gamboa, *Dynamics of carbon nanotube alignment by electric fields*. Nanotechnology, 2012. **23**(46): p. 465710.
 16. Martin, C., J. Sandler, A. Windle, M.-K. Schwarz, W. Bauhofer, K. Schulte, and M. Shaffer, *Electric field-induced aligned multi-wall carbon nanotube networks in epoxy composites*. Polymer,

2005. **46**(3): p. 877-886.
17. Monti, M., M. Natali, L. Torre, and J.M. Kenny, *The alignment of single walled carbon nanotubes in an epoxy resin by applying a DC electric field*. Carbon, 2012. **50**(7): p. 2453-2464.
 18. Prasse, T., L. Flandin, K. Schulte, and W. Bauhofer, *In situ observation of electric field induced agglomeration of carbon black in epoxy resin*. Applied Physics Letters, 1998. **72**(22): p. 2903-2905.
 19. Schwarz, M.-K., W. Bauhofer, and K. Schulte, *Alternating electric field induced agglomeration of carbon black filled resins*. Polymer, 2002. **43**(10): p. 3079-3082.
 20. Wu, S., R.B. Ladani, J. Zhang, E. Bafekrpour, K. Ghorbani, A.P. Mouritz, A.J. Kinloch, and C.H. Wang, *Aligning multilayer graphene flakes with an external electric field to improve multifunctional properties of epoxy nanocomposites*. Carbon, 2015. **94**: p. 607-618.
 21. Kim, G., *Thermo-physical responses of polymeric composites tailored by electric field*. Composites Science and Technology, 2005. **65**(11): p. 1728-1735.
 22. Kim, G. and Y.M. Shkel, *Polymeric Composites Tailored by Electric Field*. Journal of Materials Research, 2004. **19**(04): p. 1164-1174.
 23. Chen, G., H. Wang, and W. Zhao, *Fabrication of highly ordered*

- polymer/graphite flake composite with eminent anisotropic electrical property*. *Polymers for Advanced Technologies*, 2008. **19**(8): p. 1113-1117.
24. Wang, H., H. Zhang, and G. Chen, *Preparation of unsaturated polyester/graphite nanosheet conducting composite under electric field*. *Composites Part A: Applied Science and Manufacturing*, 2007. **38**(10): p. 2116-2120.
25. Wang, H., H. Zhang, W. Zhao, W. Zhang, and G. Chen, *Preparation of polymer/oriented graphite nanosheet composite by electric field-inducement*. *Composites Science and Technology*, 2008. **68**(1): p. 238-243.
26. Kwon, O.M., H. Watanabe, K.H. Ahn, and S.J. Lee, *Interplay between structure and property of graphene nanoplatelet networks formed by an electric field in a poly (lactic acid) matrix*. *Journal of Rheology*, 2017. **61**(2): p. 291-301.
27. Kwon, O.M., H. Watanabe, K.H. Ahn, and S.J. Lee, *Growths of mechanical elasticity and electrical conductance of graphene nanoplatelet/poly(lactic acid) composites under strong electric field: correlation with time evolution of higher order structure of graphene nanoplatelets*. *Rheologica Acta*, 2017. **56**(11): p. 871-885.
28. Yan, H., Y. Tang, W. Long, and Y. Li, *Enhanced thermal conductivity in polymer composites with aligned graphene*

- nanosheets*. Journal of Materials Science, 2014. **49**(15): p. 5256-5264.
29. Choi, E.S., J.S. Brooks, D.L. Eaton, M.S. Al-Haik, M.Y. Hussaini, H. Garmestani, D. Li, and K. Dahmen, *Enhancement of thermal and electrical properties of carbon nanotube polymer composites by magnetic field processing*. Journal of Applied Physics, 2003. **94**(9): p. 6034-6039.
30. Jiao, W., M. Shioya, R. Wang, F. Yang, L. Hao, Y. Niu, W. Liu, L. Zheng, F. Yuan, L. Wan, and X. He, *Improving the gas barrier properties of Fe₃O₄/graphite nanoplatelet reinforced nanocomposites by a low magnetic field induced alignment*. Composites Science and Technology, 2014. **99**: p. 124-130.
31. Wu, S., R.B. Ladani, J. Zhang, A.J. Kinloch, Z. Zhao, J. Ma, X. Zhang, A.P. Mouritz, K. Ghorbani, and C.H. Wang, *Epoxy nanocomposites containing magnetite-carbon nanofibers aligned using a weak magnetic field*. Polymer, 2015. **68**: p. 25-34.
32. Kimura, T., H. Ago, M. Tobita, S. Ohshima, M. Kyotani, and M. Yumura, *Polymer composites of carbon nanotubes aligned by a magnetic field*. Advanced Materials, 2002. **14**(19): p. 1380-1383.
33. Li, D., Y. Liu, H. Ma, Y. Wang, L. Wang, and Z. Xie, *Preparation and properties of aligned graphene composites*. RSC Advances, 2015. **5**(40): p. 31670-31676.

34. Sulong, A.B. and J. Park, *Alignment of multi-walled carbon nanotubes in a polyethylene matrix by extrusion shear flow: mechanical properties enhancement*. Journal of Composite Materials, 2011. **45**(8): p. 931-941.
35. Thostenson, E.T. and T.-W. Chou, *Aligned multi-walled carbon nanotube-reinforced composites: processing and mechanical characterization*. Journal of Physics D: Applied Physics, 2002. **35**(16): p. L77.
36. Kim, H. and C.W. Macosko, *Processing-property relationships of polycarbonate/graphene composites*. Polymer, 2009. **50**(15): p. 3797-3809.
37. Li, X., G.B. McKenna, G. Miquelard-Garnier, A. Guinault, C. Sollogoub, G. Regnier, and A. Rozanski, *Forced assembly by multilayer coextrusion to create oriented graphene reinforced polymer nanocomposites*. Polymer, 2014. **55**(1): p. 248-257.
38. Kim, D.H., K.S. Cho, T. Mitsumata, K.H. Ahn, and S.J. Lee, *Microstructural evolution of electrically activated polypropylene/layered silicate nanocomposites investigated by in situ synchrotron wide-angle X-ray scattering and dielectric relaxation analysis*. Polymer, 2006. **47**(16): p. 5938-5945.
39. Kim, D.H., J.U. Park, K.H. Ahn, and S.J. Lee, *Electrically Activated Poly(propylene)/Clay Nanocomposites*. Macromolecular Rapid Communications, 2003. **24**(5-6): p. 388-

391.

40. Kim, D.H., J.U. Park, K.S. Cho, K.H. Ahn, and S.J. Lee, *A Novel Fabrication Method for Poly(propylene)/Clay Nanocomposites by Continuous Processing*. *Macromolecular Materials and Engineering*, 2006. **291**(9): p. 1127-1135.
41. Park, J.U., Y.S. Choi, K.S. Cho, D.H. Kim, K.H. Ahn, and S.J. Lee, *Time–electric field superposition in electrically activated polypropylene/layered silicate nanocomposites*. *Polymer*, 2006. **47**(14): p. 5145-5153.
42. Ock, H.G., K.H. Ahn, and S.J. Lee, *Effect of electric field on polymer/clay nanocomposites depending on the affinities between the polymer and clay*. *Journal of Applied Polymer Science*, 2016. **133**(25).
43. Kelly, B., *The Physics of Graphite (London: Applied Science); 1981b*. *High Temp. High Pressures*, 1981. **13**: p. 245.
44. Fukushima, H. and L. Drzal. *A carbon nanotube alternative: graphite nanoplatelets as reinforcements for polymers*. in *ANTEC 2003 Conference Proceedings*. 2003.
45. Lee, C., X. Wei, J.W. Kysar, and J. Hone, *Measurement of the Elastic Properties and Intrinsic Strength of Monolayer Graphene*. *Science*, 2008. **321**(5887): p. 385-388.
46. Smith, A.W. and N.S. Rasor, *Observed Dependence of the Low-Temperature Thermal and Electrical Conductivity of Graphite on*

- Temperature, Type, Neutron Irradiation, and Bromination*.
Physical Review, 1956. **104**(4): p. 885-891.
47. Novoselov, K.S., A.K. Geim, S.V. Morozov, D. Jiang, Y. Zhang, S.V. Dubonos, I.V. Grigorieva, and A.A. Firsov, *Electric Field Effect in Atomically Thin Carbon Films*. Science, 2004. **306**(5696): p. 666-669.
48. Zhang, Y., Y.-W. Tan, H.L. Stormer, and P. Kim, *Experimental observation of the quantum Hall effect and Berry's phase in graphene*. Nature, 2005. **438**(7065): p. 201-204.
49. Kim, H., A.A. Abdala, and C.W. Macosko, *Graphene/Polymer Nanocomposites*. Macromolecules, 2010. **43**(16): p. 6515-6530.
50. Kim, H. and C.W. Macosko, *Morphology and Properties of Polyester/Exfoliated Graphite Nanocomposites*. Macromolecules, 2008. **41**(9): p. 3317-3327.
51. Kim, H., Y. Miura, and C.W. Macosko, *Graphene/polyurethane nanocomposites for improved gas barrier and electrical conductivity*. Chemistry of Materials, 2010. **22**(11): p. 3441-3450.
52. Ramanathan, T., A. Abdala, S. Stankovich, D. Dikin, M. Herrera-Alonso, R. Piner, D. Adamson, H. Schniepp, X. Chen, and R. Ruoff, *Functionalized graphene sheets for polymer nanocomposites*. Nature Nanotechnology, 2008. **3**(6): p. 327-331.
53. Stankovich, S., D.A. Dikin, G.H. Dommett, K.M. Kohlhaas, E.J. Zimney, E.A. Stach, R.D. Piner, S.T. Nguyen, and R.S. Ruoff,

- Graphene-based composite materials*. Nature, 2006. **442**(7100): p. 282-286.
54. Castro Neto, A.H., F. Guinea, N.M.R. Peres, K.S. Novoselov, and A.K. Geim, *The electronic properties of graphene*. Reviews of Modern Physics, 2009. **81**(1): p. 109-162.
55. *Schematic representation of GNP*. [Retrieved November 11, 2017]; Available from: <https://www.cheaptubes.com/product-category/graphene-nanoplatelets/>.
56. *SEM of graphene nanoplatelet*. [Retrieved November 11, 2017]; Available from: http://s.b5z.net/i/u/10091461/i/US1059-SEM-Graphene_Nanoplatelets.jpg.
57. Lee, A., Y. Matsumiya, H. Watanabe, K.H. Ahn, and S.J. Lee, *Multiple representation of linear dielectric response*. Nihon Reoroji Gakkaishi (J. Soc. Rheol. Japan), 2010. **38**(3): p. 149-155.
58. Crawford, R.J. and Y. Yigsaw, *A study of the effect of test variables on the flexural modulus of plastics*. Journal of Materials Science Letters, 1984. **3**(2): p. 171-176.
59. Wang, Y., L. Yang, Y. Niu, Z. Wang, J. Zhang, F. Yu, and H. Zhang, *Rheological and topological characterizations of electron beam irradiation prepared long-chain branched polylactic acid*. Journal of Applied Polymer Science, 2011. **122**(3): p. 1857-1865.
60. Barrau, S., P. Demont, A. Peigney, C. Laurent, and C. Lacabanne,

- DC and AC Conductivity of Carbon Nanotubes–Polyepoxy Composites*. *Macromolecules*, 2003. **36**(14): p. 5187-5194.
61. Du, F., R.C. Scogna, W. Zhou, S. Brand, J.E. Fischer, and K.I. Winey, *Nanotube Networks in Polymer Nanocomposites: Rheology and Electrical Conductivity*. *Macromolecules*, 2004. **37**(24): p. 9048-9055.
62. Zhang, W.L., Y.D. Liu, and H.J. Choi, *Field-responsive smart composite particle suspension: materials and rheology*. *Korea-Australia Rheology Journal*, 2012. **24**(3): p. 147-153.
63. Jones, T.B. and T.B. Jones, *Electromechanics of particles*. 2005: Cambridge University Press.
64. Bloomfield, V.A., *Survey of biomolecular hydrodynamics*. On-Line Biophysics Textbook: Separations and Hydrodynamics, 2000.
65. Li, J., Q. Zhang, N. Peng, and Q. Zhu, *Manipulation of carbon nanotubes using AC dielectrophoresis*. *Applied Physics Letters*, 2005. **86**(15): p. 153116.